

**Metabolic alteration of circulating monocytes during
neuroinflammation: method development and *in vitro*
studies in Alzheimer's disease and multiple sclerosis**

Inaugural-Dissertation
to obtain the academic degree
Doctor rerum naturalium (Dr. rer. nat.)

submitted to the Department of Biology, Chemistry, Pharmacy
of Freie Universität Berlin

by
Ginevra Giacomello
2023

Research of the present study was conducted from 2019 till 2023 under the supervision of Prof. Dr. Maria Kristina Parr at the Institute of Pharmacy of the Freie Universität Berlin in collaboration with PD Dr. Chotima Böttcher at the Charité Universitätsmedizin Berlin.

1st Reviewer: Prof. Dr. Maria Kristina Parr

2nd Reviewer: Prof. Dr. Francesco Botrè

Date of Defense: 24th of August 2023

Nci dissì u surici a nuci dammi tempu ca ti perciu.

My grandmother

Acknowledgements

I want to thank Prof. Dr. Maria Kristina Parr for being the best supervisor I could ask for. She granted me the freedom to grow, encouragement to never give up, and, above all, extraordinary scientific support and guidance. I could not be luckier as a student and scientist to work and learn from her.

I want to thank PD Dr. Chotima Böttcher for her amazing introduction to the world of monocytes and neuroinflammation. Neuroscience was far from my background, but thanks to her precious and comprehensive insight we found the way in this fantastic project.

I thank Prof. Dr. Francesco Botrè, without him, I would not be here now. His passion for science in all its aspects and his incredible way of teaching expanded my horizons and sparked my scientific curiosity. He has been a wise and precious mentor along this journey of science and life experiences.

I thank Bernhard Wüst for his fantastic scientific and technical help. He answered all my questions, revealing the inherent beauty of the instruments.

I sincerely thank my current and former colleagues from the group of Prof. Dr. Parr. Their friendship and always instructive scientific exchanges made me look forward to going to the institute. These years with them have flown.

I also want to thank my friends, near and far, for being such an incredible part of my life.

Fully expressing my gratitude and enormous thankfulness to my parents, Pierluigi e Gabriella, is hard. Their unconditional love and support never left my side, even a thousand kilometres away. They told me how to be independent and, at the same time, showed me how strong “together” can be. I also thank my brother Alberto and his beautiful family, Lavinia, Leone, and Lucrezia. They are an endless source of joy and love. Finally, I thank Nicola, the love of my life. Thank you for being so marvellously you.

Table of Contents

I	Abbreviations	III
1	Introduction and Aim of the Project	1
1.1	Alzheimer's disease and multiple sclerosis	2
1.2	Cell metabolism	4
2	Methods	8
2.1	<i>In vitro</i> metabolic studies	8
2.2	Isotopic tracing metabolic studies	9
2.3	Analysis of the metabolites and their analytical challenges.....	11
3	Manuscripts.....	17
3.1	Manuscript I: "Isotopic tracing of glucose metabolites in human monocytes to assess changes in inflammatory conditions"	17
3.2	Manuscript II: "Differential compartmentalisation of myeloid cell phenotypes and responses towards the CNS in Alzheimer's disease"	43
3.3	Manuscript III: "1,2- ¹³ C ₂ -Glucose Tracing Approach to Assess Metabolic Alterations of Human Monocytes under Neuroinflammatory Conditions"	62
4	Declaration of Own Contribution	82
5	Discussion and Outlook	83
6	Summary.....	88
7	Zusammenfassung.....	90
8	References	92
9	List of Publications.....	102
9.1	Publications in scientific peer-reviewed journals	102

9.2	Oral presentations.....	103
9.3	Poster presentations.....	103
10	Independence Declaration.....	104
11	Appendix.....	105
11.1	List of Figures	105
11.2	List of Tables	106

I Abbreviations

AcCoA	acetyl coenzyme A
AD	Alzheimer's disease
AD-CSF	cerebral spinal fluid of patients with Alzheimer's disease
ATP	adenosine triphosphate
AX	anion exchange
A β	beta-amyloid
BCSFB	blood-cerebral spinal fluid barrier
CCM	central carbon metabolism
CNS	central nervous system
CON-CSF	cerebral spinal fluid of healthy donors
CSF	cerebral spinal fluid
dMRM	dynamic multiple reaction monitoring
EBV	Epstein-Barr virus
EIC-	extracted ion chromatogram in negative mode
EDTA	ethylenediaminetetraacetic acid
F6P	fructose-6-phosphate
FA-CoA	fatty acyl-coenzyme A
FADH ₂	dihydro-flavine-adenine dinucleotide
GC	gas chromatography
HILIC	hydrophilic interaction liquid chromatography
HPLC	high-performance liquid chromatography
HPLC-ESI-QQQ-MS	high-performance liquid chromatography coupled by electrospray ionisation to triple quadrupole
HPLC-MS/MS	high-performance liquid chromatography coupled with tandem mass spectrometry

IEX	ion exchange
IFN- γ	interferon- γ
IP	ion pairing agents
LC	liquid chromatography
LPS	lipopolysaccharide
MACS	magnetic-activated cell separation
MM	mixed-mode chromatography
MS	mass spectrometry
MS/MS	tandem mass spectrometry
MScI	multiple sclerosis
MScI-CSF	cerebral spinal fluid of patients with multiple sclerosis
NADPH	nicotinamide-adenine dinucleotide phosphate
NFT	neurofibrillary tangles
PBMC	peripheral blood mononuclear cell
PEEK	polyether ether ketone
PPP	pentose phosphate pathway
QQQ	triple quadrupole
RP	reversed-phase chromatography
TCA	tricarboxylic acid
UVB	ultraviolet B light
z-HILIC	zwitterionic hydrophilic interaction liquid chromatography

1 Introduction and Aim of the Project

Alzheimer's disease (AD) and multiple sclerosis (MScl) are two of the most studied pathologies of the central nervous system to their devastating consequences in terms of life quality, worldwide spread, and cost for the healthcare systems.

In 2019, 55 million people worldwide were diagnosed with dementia, whereby 60-80% are attributable to AD. This number is destined to increase to 78 million in 2030. The cost of care and treatment for dementia is estimated to be above 1.3 trillion dollars annually and is expected to rise to 2.8 trillion dollars by 2030 [1]. The human cost in suffering, for both patients and caregivers, is way more devastating and cannot be reduced to a number. Similarly, 2.8 million people were diagnosed worldwide in 2020 with MScl [2]. Although these two diseases differ in course, onset, and pathophysiology, they have aspects in common. Both, for instance, present neuroinflammation and activation of immune cells, including microglia/macrophages, in the central nervous system (CNS), possibly initiating neurodegeneration. Despite numerous studies, both diseases remain uncured. Furthermore, their aetiology remains largely unknown. Therefore, every piece of information is a step forward in unfolding their complexity.

As mentioned above, a common trait of AD and MScl is neuroinflammation and, with it, the impairment of the barrier between blood and cerebral spinal fluid (BCSFB) together with infiltration of immune cells from the bloodstream.

This project aims to study the alterations in the metabolism of monocytes recruited from the bloodstream into the cerebral spinal fluid (CSF) during neuroinflammation and evaluate possible differences between AD and MScl. With this purpose, a method has been developed, optimised, and validated for

the analysis of glucose metabolites using high-performance liquid chromatography (HPLC) hyphenated with mass spectrometry (MS).

1.1 Alzheimer's disease and multiple sclerosis

AD is a chronic neurodegenerative disorder that causes the decline of the cognitive functions of the patient. Ageing is not the only high-risk factor in developing the disease. Also, but not limited to, genetic predisposition, severe head injury, or cerebrovascular disease may have a role in it [3]. The typical clinical features of AD include a progressive loss of memory, topographical and spatial difficulties, and behavioural alterations. Cognitive impairment increases with the progress of the disease and neurodegeneration. This causes a complete loss of autonomy, the mobility of the patient becomes compromised, and seizures may occur at a late stage. Death usually comes 8.5-10 years after symptom manifestation [4, 5].

The aetiology is still under debate, and the pathophysiology picture is far from complete. Still, it is widely accepted that abnormalities relative to the proteins beta-amyloid ($A\beta$) and Tau are two fundamental hallmarks of AD [6-8]. The overproduction and failure in the clearance of the $A\beta$ lead to an accumulation of the protein into fibrils which lead to plaques, causing impairment of synaptic functions. Similarly, the hyperphosphorylated Tau protein aggregates in neurons, forming neurofibrillary tangles (NFT) and reducing neuronal activity [3, 7]. The third and equally important hallmark of AD is microglial activation and neuroinflammation. This chronic inflammation is not only a reaction to the formation of plaques and NFT but becomes part of the pathogenesis itself [9]. Microglia are the resident macrophages of the brain responsible for the immune response in case of brain injury or infection. When in a resting state, they have a characteristic ramified structure optimal for scanning the CNS. Once an inflammatory disease or environmental factors disrupt the homeostasis of the brain, the microglia get activated in a process

called “microglial priming”. They change morphology into an amoeboid form able to quickly move towards the injury or infection site and release pro- and anti-inflammatory cytokines and other inflammatory mediators [10].

MScl is a chronic disease of the CNS characterised by neuroinflammation and progressive demyelination. The disease course leads to an increasing impairment of neurological functions and neurodegeneration. It occurs in young adults (20-40 years of age) and is a polysymptomatic disease. The most common clinical features include optic neuritis, spinal cord and brainstem syndromes, sensory disorders, and ataxia [11-13]. As for AD, the causes of MScl are not yet clear, however, some factors have been recognised as risk drivers. The list includes deficiency of vitamin D, Epstein–Barr virus (EBV) infection, obesity, smoking, and genetic susceptibility [14-16].

The pathology of MScl is characterised by neuroinflammation that causes multifocal lesions in the white and grey matter with demyelination plaques and progressive axonal damage [11, 17]. Neurodegeneration diffuses with the progression of the disease, causing brain atrophy and hypoxia-like injuries [18]. As previously mentioned for AD, with MScl also microglia get activated and undergo microglial priming, releasing a variety of pro- and anti-inflammatory cytokines and mediators [19].

AD is a neurodegenerative disease, whereas MScl is primarily neuroinflammatory. The course, the pathology, and the affected population of the two conditions present many differences. Nevertheless, as briefly mentioned above, they have several aspects in common: both disorders show neuroinflammation, microglial activation, and neurodegeneration. Another commonality, and starting point of this research work, is the infiltration of myeloid cells into the CSF caused by the disruption of the BCSFB. This integrity loss, driven by both diseases and their subsequent neuroinflammation, is shown in Figure 1 and has been previously reported [20-25].

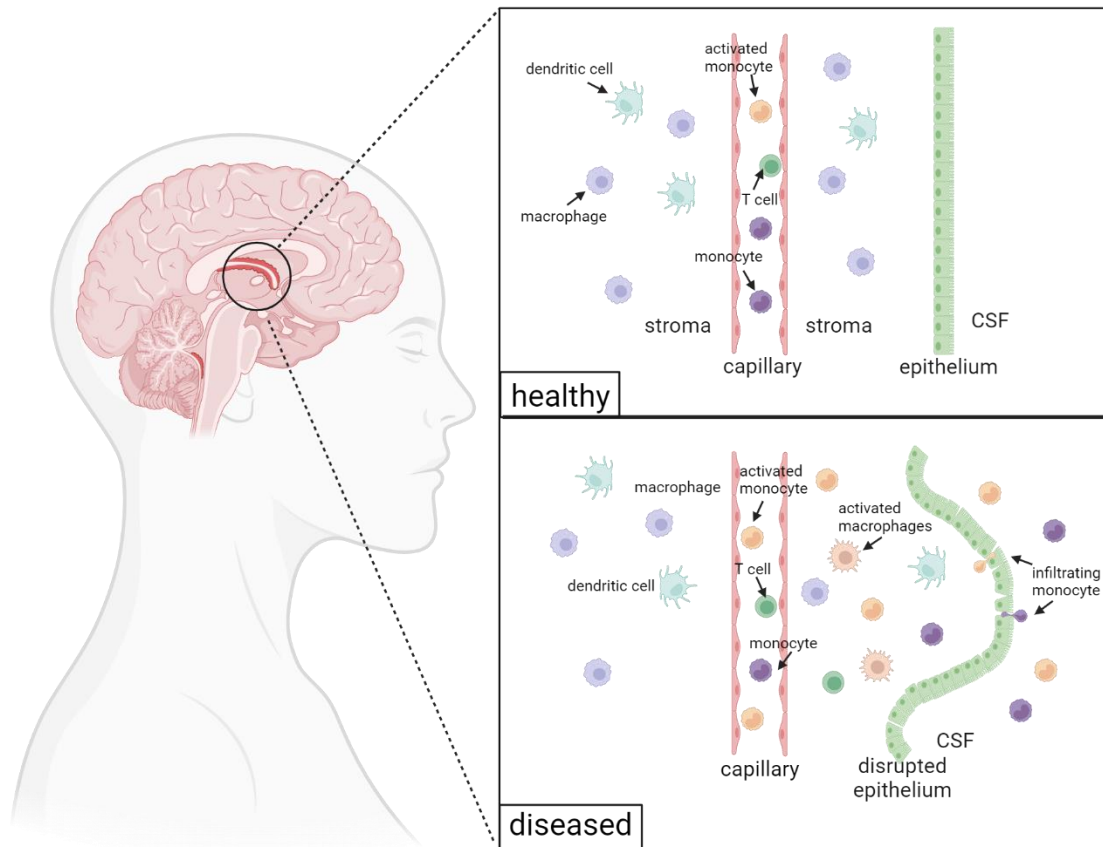


Figure 1: Barrier between CSF and blood in the choroid plexus in healthy individuals (upper pane) and patients with AD or MScl (lower pane). In the case of diseased people, the tight junctions of the epithelium lose their integrity, allowing the passage of myeloid cells into the CSF [26-29] (figure created with BioRender.com).

The role of immune cells (monocytes, dendritic cells, and macrophages) in infiltrating the CSF is still under debate. Understanding their function in the diseases is necessary not only for prognostic but also for potential therapeutics purposes. It is essential to evaluate how the compartment change and the new microenvironment affect the monocytes and to obtain a clear picture of their function in the CSF.

1.2 Cell metabolism

The metabolism regulates every aspect of cellular life. The well-being or distress, every biosynthetic process, phenotypic alterations, the energy consumption or production, all these processes are strictly correlated to glucose catabolism. Moreover, the disruption of the homeostasis of the metabolic

system can be a red flag for starting or ongoing inflammation [30]. Assessment of metabolic changes is a valuable tool for estimating the effect of a change in environment on a cell. Reprogramming a cell phenotype, or cell activation and release of cytokines, requires a rewiring of the metabolism to support the adaptive changes of the cell to the new role or environment.

The major metabolic pathways of a cell (Figure 2) include:

- **glycolysis (A):** catabolism of glucose for producing energy and pyruvate. It takes place in the cytosol of a cell. The overall process transforms a six-carbon molecule (glucose) into two three-carbon molecules (pyruvate), two molecules of adenosine triphosphate (ATP) —the energy storage and source of a cell—, and two molecules of reduced nicotinamide-adenine dinucleotide phosphate (NADPH).
- **pentose phosphate pathway (PPP) (B):** branch of the glycolysis that produces ribose-5-phosphate, the sugar necessary for synthesising nucleotides. It takes place in the cytosol, where is one of the first sources of NADPH production.
- **glutamate/glutamine metabolism (C):** necessary to maintain nitrogen balance in the cell. Glutamate is produced from α -ketoglutarate (intermediates of the tricarboxylic acid (TCA) cycle) and glutamine from glutamate. Glutamine is crucial for synthesising purine and pyrimidines, while glutamate is for gamma-aminobutyric acid, folic acid, proline, and glutathione. Glutamate is also an excitatory neurotransmitter, but if present in concentrations too elevated, it may cause neuronal damage. Therefore, it may be converted into glutamine. If necessary, glutamine and glutamate can fuel the tricarboxylic acid cycle.
- **tricarboxylic acid (TCA) cycle (D):** is an aerobic pathway for the metabolism of glucose-derived acetyl coenzyme A (AcCoA). It occurs in the mitochondria and produces three molecules of NADPH, one of

dihydro-flavine-adenine dinucleotide (FADH₂), and one of ATP. The molecules of NADPH and FADH₂ generated with the TCA cycle are the electron carriers for oxidative phosphorylation and the consequent production of energy in the form of ATP.

- **lactate metabolism (E):** is the transformation of pyruvate into lactate. Lactate is an end-product of glycolysis in both anaerobic and aerobic conditions. Lactate production increases when the metabolic demand per time for ATP is higher or under stressful conditions.
- **serine/glycine metabolism (F):** glycine derives from serine, and serine comes from the intermediate of glycolysis 3-phosphoglycerate. The conversion between serine and glycine is reversible and, as amino acids, they are both building blocks of proteins. Serine is crucial in the cycles of folate and methionine, in cell proliferation, and in the synthesis of phosphatidylserine and sphingolipids. In the brain, they both have essential roles in neurotransmission.

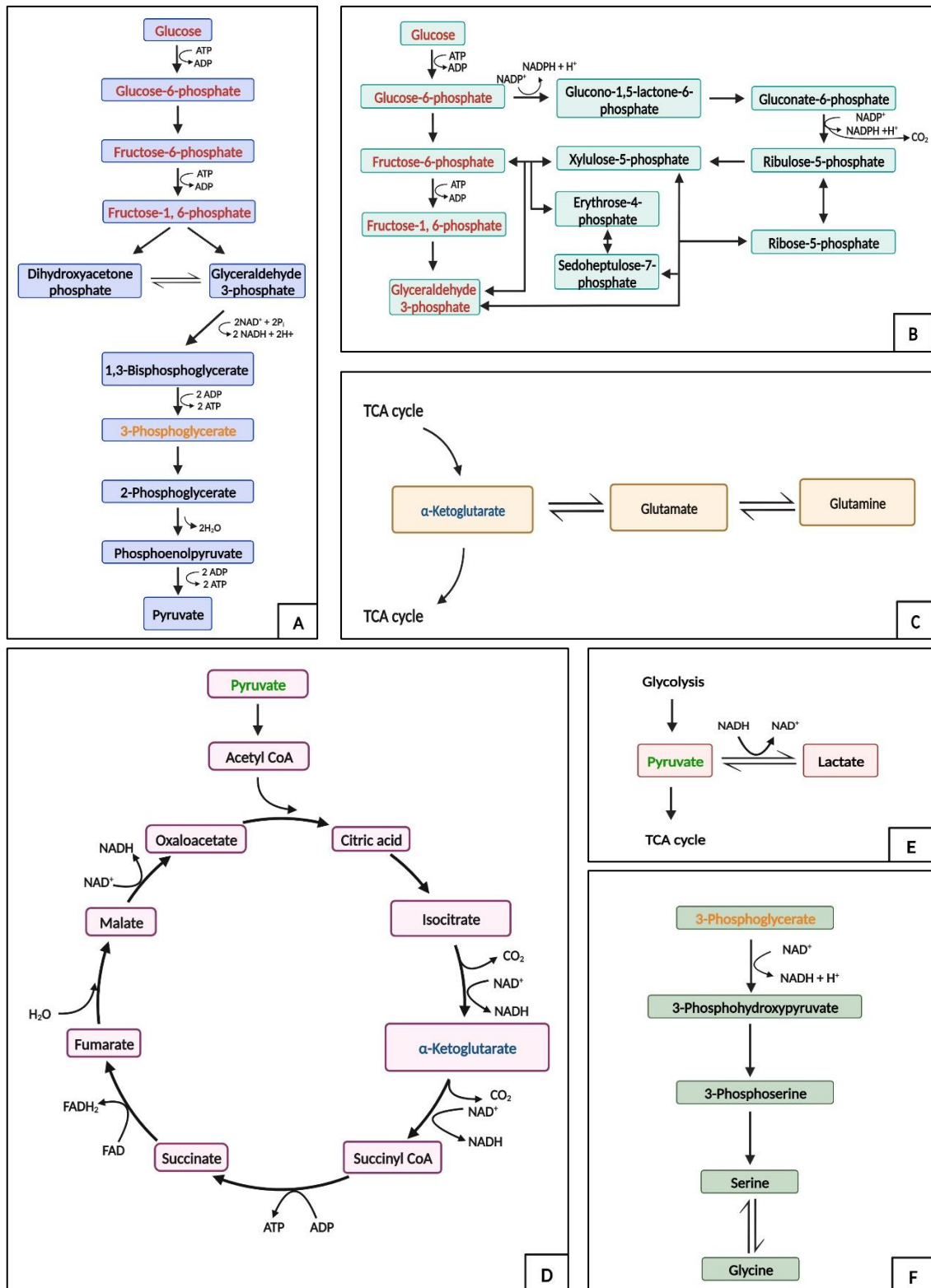


Figure 2: Major metabolic pathways of a cell. A: glycolysis; B: pentose phosphate pathway (PPP); C: glutamate/glutamine metabolism; D: tricarboxylic acid (TCA) cycle; E: lactate metabolism; F: serine/glycine metabolism (figure created with BioRender.com).

2 Methods

2.1 *In vitro* metabolic studies

Investigation of metabolic alterations in CNS cells is complex. First, like every metabolism study, it is a multivariate question, and it is challenging to understand the cause of the overall variation. Second, obtaining certain sample types (i.e. CSF) is difficult, particularly from healthy individuals. Third, the number of available cells is meagre for some specimens like CSF.

There are mainly two approaches for addressing an *in vitro* cell (metabolism) study, depending on the aim of the research [31].

- **immortalised cell lines:** do not require ethical approval, are easy to use, provide an unlimited source of cells, and are cost-friendly. Moreover, they are a single and pure cell population, guaranteeing reproducible results. Certain immortalised cell lines may present a loss of metabolising enzymes after multiple passages, thus affecting the validity and reproducibility of the experiments [32, 33]. Due to genetic manipulation, they may not maintain the same functional, physiological, and reactive features as their corresponding primary cells [31]. They are mainly used to test drugs, their metabolism and cytotoxicity, optimise and produce vaccines and antibodies, and biotechnological syntheses [34-36].
- **primary cells:** need the ethical committee approval and incubation may be challenging. They are a limited source and are more expensive. These cells are more responsive towards stimulations and are a more accurate model for biochemical, metabolic, and pathophysiological studies [37]. They mimic the *in vivo* physiology and state more truthfully than their corresponding immortalised cell lines. Therefore, the results obtained are biologically more relevant.

Primary cells can proliferate for a limited time before undergoing genetic transformation. These cells are typically used for biological and preclinical studies, metabolism, intracellular communication, and disease-related mechanisms [38].

This research focuses on studying the alterations in the immunometabolism related to AD and MScl. Therefore, *ex vivo* peripheral blood mononuclear cell (PBMC)-derivated monocytes were incubated alone or in the presence of CSF of healthy individuals, AD or MScl patients, to mimic the compartment change (from the peripheral blood into the CSF) and the characteristics of the environment presented by the different diseases.

2.2 Isotopic tracing metabolic studies

To better understand towards which pathways monocytes rewire their metabolism under different stimuli, isotopically labelled tracers are powerful tools. They provide a complete overview of the preferential biochemical pathway and metabolic changes associated with cell activation and function under various conditions (e.g. CSF microenvironment of AD or MScl patients).

The most commonly used tracer for *in vitro* studies of cell metabolism is glucose. Incubating the cells in the presence of labelled glucose as the only source of nourishment can give an insight into their physiological state. Moreover, the use of different isotopologues of glucose (e.g. [U-¹³C]glucose (uniformly labelled with ¹³C), [1-¹³C]glucose, or [1,2-¹³C₂]glucose) offers multiple and sometimes complementary data. For instance, incubating cells with [1,2-¹³C₂]glucose instead of [U-¹³C]glucose provides specific information on the synthetic pathway of ribose-5-phosphate (oxidative and non-oxidative PPP) and fructose-6-phosphate [39-41] or lactate [42, 43], thanks to different isotopomeric or isotopologues distributions. Figure 3 shows an example of the results obtained by incubating cells with [1,2-¹³C₂]glucose as substrate:

fructose-6-phosphate and lactate present different isotopologues depending on the formation pathway.

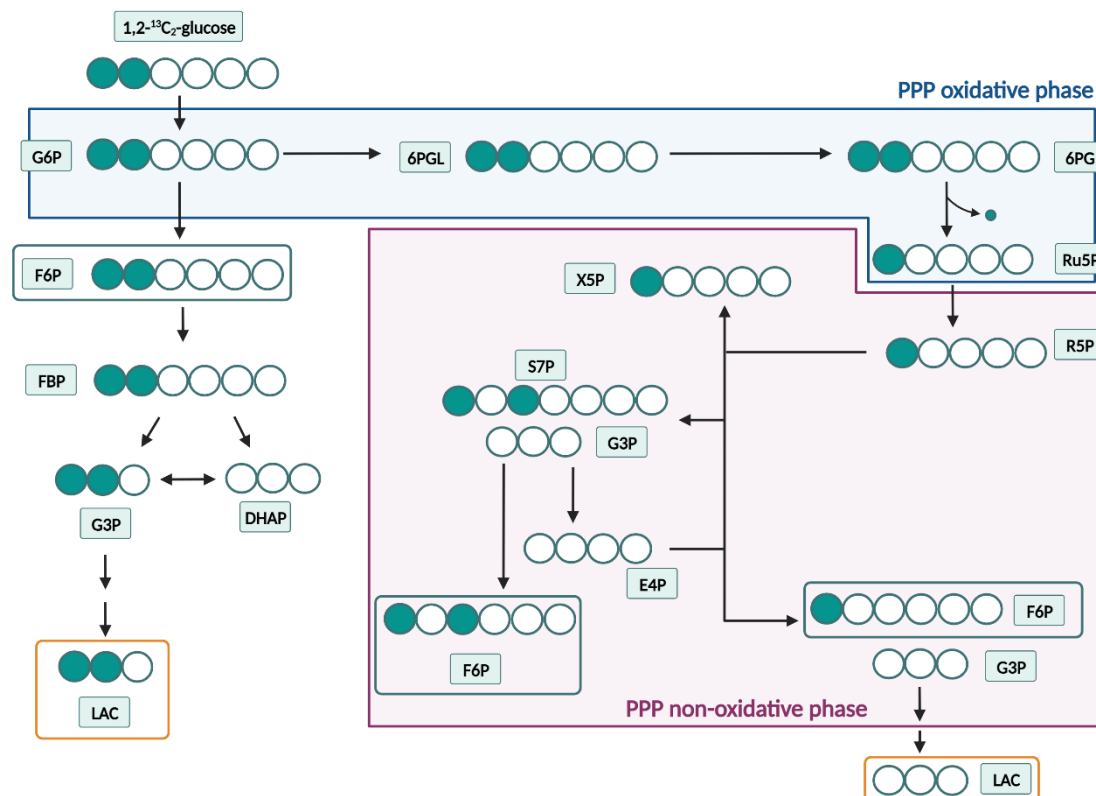


Figure 3: Metabolism (glycolysis and pentose phosphate pathway (PPP)) of $[1,2-^{13}\text{C}_2]$ glucose. The isotopic distribution of labelled carbons makes it possible to distinguish between the formation pathways of fructose-6-phosphate (green squared frames) and lactate (orange squared frames). G6P: glucose-6-phosphate; F6P: fructose-6-phosphate; FBP: fructose-1,6-biphosphate; G3P: glyceraldehyde-3-phosphate; DHAP: dihydroxyacetone phosphate; LAC: lactate; 6PGL: glucono-1,5-lactone-6-phosphate; 6PG: gluconate-6-phosphate; Ru5P: ribulose-5-phosphate; R5P: ribose-5-phosphate; X5P: xylulose-5-phosphate; S7P: sedoheptulose-7-phosphate; E4P: erythrose-4-phosphate (figure created with BioRender.com).

^{13}C -Glucose isotopologues are the most commonly used but are not the only isotopic tracers available. Depending on the focus of the study, there are different possible solutions. $[\text{U}-^{13}\text{C}]$ Glutamine, for example, has been used to elucidate the TCA cycle metabolites [44-46]. $[\text{U}-^{13}\text{C}]$ xylose was used for the investigation of the PPP [47, 48]. For studies on amino acids, glutathione metabolism, and pyrimidine nucleotide synthesis, however, the use of $^{15}\text{N}_2$ -glutamine has been reported [49].

Ultimately, it is necessary to plan the experiments carefully before the incubation. Many metabolic substrates (e.g. glucose, glutamine, xylose),

different stable isotopes (e.g. ^{13}C , ^{15}N , ^2H), and isotopologues or isotopomers can be used. The aim of the research and the targeted pathway must guide the selection of the most suitable isotopic tracer or tracers.

In this research, [1,2- $^{13}\text{C}_2$]glucose was selected as an isotopically labelled tracer to comprehensively overview the general metabolism of monocytes while keeping track of each specific pathway (as illustrated in Figure 3).

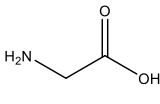
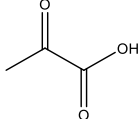
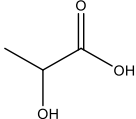
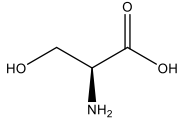
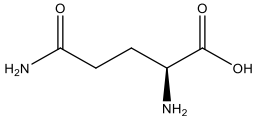
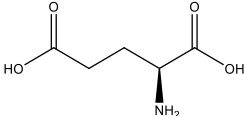
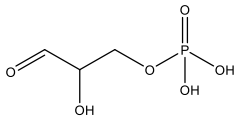
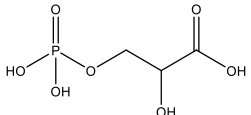
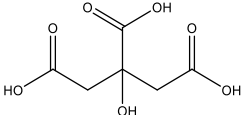
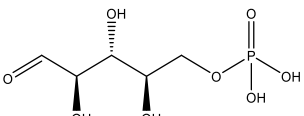
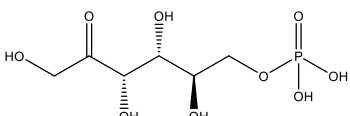
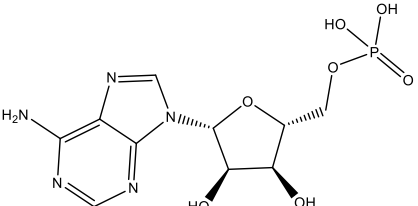
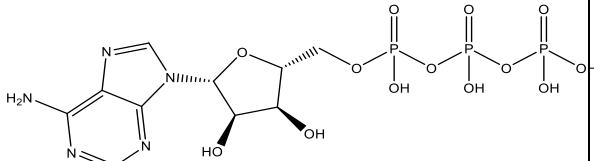
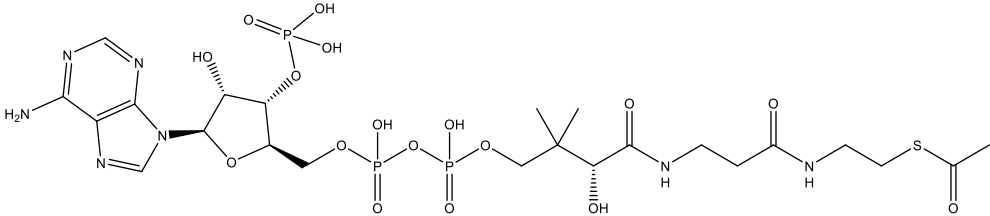
2.3 Analysis of the metabolites and their analytical challenges

The most common approach for analysing the alterations of the metabolism is liquid chromatography (LC) or gas chromatography (GC) coupled to mass spectrometry (MS). By hyphenating these techniques, it is possible to take full advantage of both: the resolution power and selectivity of chromatography and the high sensitivity and selectivity of MS. This is critical, especially in the case of limited samples (e.g. monocytes and CSF) or complex matrices. GC is mainly used for volatile or derivatised analytes, while LC is preferred for non-volatile and for both polar and non-polar compounds [50].

The targeted analysis of several labelled and non-labelled metabolites has been optimised and performed in this research. Due to heterogeneous physicochemical properties (e.g. different polarity, pKa, stability, solubility) among the analytes, LC hyphenated with a triple quadrupole (QQQ) analysis is the technique of choice. In fact, QQQ tandem mass spectrometry (MS/MS) is considered the most suitable choice for targeted metabolomics [51-53]. The analysed unlabelled metabolites are summarised in Table 1. As can be inferred from the chemical structures, the metabolites are all either polar or very polar substances. The high polarity of an analyte can be a challenge for chromatographic separation. In this case, the most common chromatographic approaches (combined with MS detection) are mainly three: reversed-phase

(RP), mixed-mode (MM), or hydrophilic interaction liquid chromatography (HILIC).

Table 1: Metabolites (displayed as unlabelled form) of the major metabolic pathways targeted in this study (structures created with ChemDraw Professional 15.1)

			
glycine	pyruvic acid	lactic acid	serine
			
glutamine	glutamic acid	glyceraldehyde-3-phosphate	
			
3-phosphoglyceric acid	citric acid		
			
ribose-5-phosphate	fructose-6-phosphate		
			
adenosine monophosphate	adenosine triphosphate		
			
acetyl coenzyme A			

- **Reversed-phase chromatography:** it is characterised by a non-polar stationary phase, such as C18 or fluoro-phenyl, and a polar mobile phase (usually water and organic solvents like methanol or acetonitrile). Due to the insufficient retention of very polar analytes on the column, RP is not feasible unless ion pairing agents (IP) (e.g. alkylsulfonic acids, alkylamines, fluorinated carboxylic acids) are added to the eluents. The use of IP, though, can affect the sensitivity of the analysis due to ion suppression and can contaminate the system causing a persistent carry-over. Moreover, some IP are not suitable for MS analysers [54, 55].
- **Mixed mode chromatography:** it is a combination of two (or more) different retention modes (e.g. C18 and anion exchange (AX), ion exchange (IEX) and neutral polar) and, therefore, mixed stationary phases. The composition of the mobile phase depends on the typology of the column. In practice, though, often only one separation mode can be used at a time, depending on the ratio of mobile phases [56, 57].
- **HILIC:** is the most commonly used mode for very polar compounds when coupled to MS. It consists of a polar stationary phase and an organic-rich mobile phase (methanol or acetonitrile). The separation occurs thanks to the intermolecular interactions of the analytes with the aqueous layer formed on the surface of the stationary phase (e.g. H-bonding, dipole-dipole interaction, electrostatic). HILIC coupled with MS usually allows a better sensitivity than RP for polar analytes since no IP are needed, and the polar organic-rich mobile phases are more volatile [58]. Moreover, it enables the separation of anions, cations, and polar neutral compounds in one analytical run. The limitations of HILIC separation are mainly four. First, the sample must be soluble in an organic-rich mobile phase; second, the choice of the sample solvent is critical; third, the high amount of organic

solvents in the mobile phase limits the use of buffers; four, the column requires a longer time to equilibrate. There is a wide variety of different HILIC stationary phases.

One of the most used in targeted metabolomics is the zwitterionic HILIC (z-HILIC) [59-61], which adds the zwitterionic interaction with those mentioned above for partitioning the analytes between the mobile phases and the aqueous layer.

There is one last point to consider when analysing metabolites of the central carbon metabolism. Most of the targeted compounds contain vicinal hydroxylic or phosphate groups, which can cause severe peak tailing and sometimes solute adsorption. Examples include citric acid and all the analytes containing a phosphate group, like adenosine triphosphate (ATP) or fructose-6-phosphate (F6P). This effect is caused by the interaction or non-specific adsorption of the solute with the metallic components of the instrument [62-66]. It is known that phosphates [67, 68] and citrate [69, 70] have a coordinating affinity towards Fe^{3+} . The resulting peak broadening can be extreme, making the integration difficult or sometimes impossible. Figure 4A depicts an example (ribose-5-phosphate) of the effect on retention of the chelating interaction between the analyte and the metallic parts of the instrument.

There are different approaches to overcome this problem. Pesek *et al.* used ethylenediaminetetraacetic acid (EDTA) in aqueous normal phase analysis. They 1) added it to the mobile phases in low concentrations, 2) injected a significant volume, highly concentrated, before the beginning of the analysis of each batch, or 3) used it as part of the sample solvent [71]. Since EDTA is highly ionisable, significant signal suppression has been highlighted in all three options. The most effective approach was the continuous, low-concentrated perfusion of EDTA through the mobile phases. A similar method was used by Myint *et al.* [72] with HILIC nano-column.

Another additive used in HILIC [60, 73, 74] and RP-LC [75] analysis is medronic acid. Similarly to the first method, adding a competing, more appealing, and constant chelating agent into the mobile phases results in a better peak shape. Medronic acid has the advantage of causing minimal ion suppression. The optimised peak is shown in Figure 4B.

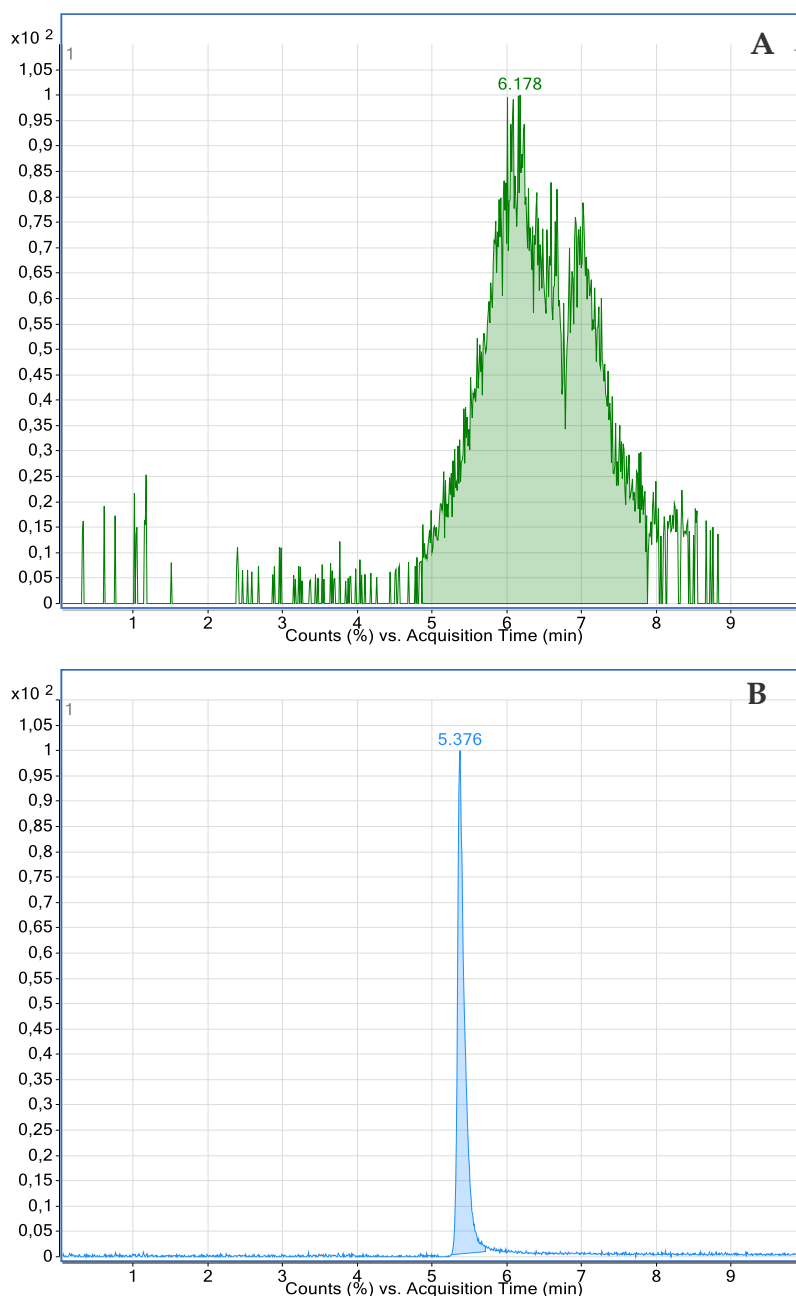


Figure 4: Chromatographic peaks of ribose-5-phosphate (R5P). A: chromatogram of R5B with no additives in the mobile phases. The peak is broad due to the coordinating interactions of the phosphate group of the analyte with the metallic parts of the instrumentation (iron cations). B: chromatogram of R5B with medronic acid as additive in both the mobile phases (method detailed in Manuscript I). The peak shape is optimised, allowing the identification and quantification of the analyte. Column: Agilent InfinityLab Poroshell 120 HILIC-Z, 2.1 x 100 mm, 2.7 μ m; extracted ion chromatograms in negative mode (EIC-) of ribose-5-phosphate ([M-H]⁻ m/z 229.0).

Another possibility is the substitution of all the capillaries, tubing, and sample loop with inert polyether ether ketone (PEEK) and the use of metal-free or bioinert systems [65, 76]. This method is probably the most effective but is also not a real solution for laboratories where bioinert systems are not available.

In this study, intracellular and extracellular key-role metabolites were analysed with high-performance liquid chromatography coupled with tandem mass spectrometry (HPLC-MS/MS) to overview the metabolic profiles comprehensively. Medronic acid was used to optimise the peak shape with a z-HILIC column.

3 Manuscripts

3.1 Manuscript I: “Isotopic tracing of glucose metabolites in human monocytes to assess changes in inflammatory conditions”

Ginevra Giacomello, Chotima Böttcher, and Maria Kristina Parr

STAR Protocols; 3 (2022) 101715

DOI: 10.1016/j.xpro.2022.101715

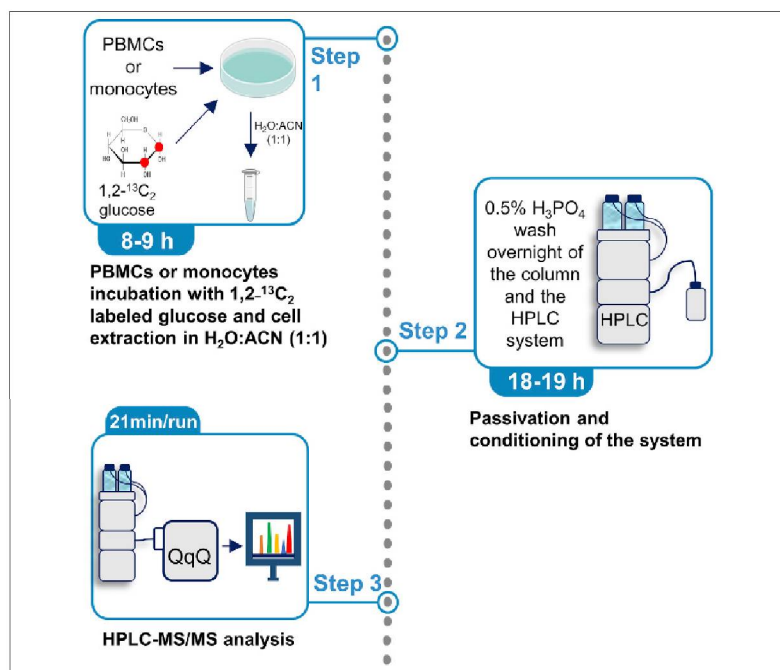
Abstract: Differences in metabolic profiles can link to functional changes of immune cells in disease conditions. Here, we detail a protocol for the detection and quantitation of 19 metabolites in one analytical run. We provide the parameters for chromatographic separation and mass spectrometric analysis of isotopically labeled and unlabeled metabolites. We include steps for incubation and sample preparation of PBMCs and monocytes. This protocol overcomes the chromatographic challenges caused by the chelating properties of some metabolites.

STAR Protocols

CellPress
OPEN ACCESS

Protocol

Isotopic tracing of glucose metabolites in human monocytes to assess changes in inflammatory conditions



Differences in metabolic profiles can link to functional changes of immune cells in disease conditions. Here, we detail a protocol for the detection and quantitation of 19 metabolites in one analytical run. We provide the parameters for chromatographic separation and mass spectrometric analysis of isotopically labeled and unlabeled metabolites. We include steps for incubation and sample preparation of PBMCs and monocytes. This protocol overcomes the chromatographic challenges caused by the chelating properties of some metabolites.

Publisher's note: Undertaking any experimental protocol requires adherence to local institutional guidelines for laboratory safety and ethics.

Ginevra Giacomello,
Chotima Böttcher,
Maria Kristina Parr

ginevra@zedat.fu-berlin.de (G.G.)
maria.parr@fu-berlin.de (M.K.P.)

Highlights

Protocol for the quantitation of glucose metabolites

Protocol for the incubation and sample preparation of PBMCs and monocytes

Chromatographic separation of cell metabolites in major metabolic pathways

dMRM parameters for cell metabolites in major metabolic pathways

Giacomello et al., STAR
Protocols 3, 101715
December 16, 2022 © 2022
The Authors.
<https://doi.org/10.1016/j.xpro.2022.101715>



STAR Protocols

CellPress
OPEN ACCESS



Protocol

Isotopic tracing of glucose metabolites in human monocytes to assess changes in inflammatory conditions

Ginevra Giacomello,^{1,5,*} Chotima Böttcher,^{2,3,4} and Maria Kristina Parr^{1,6,*}

¹Institute of Pharmacy, Freie Universität Berlin, Königin-Luise-Str. 2–4, 14195 Berlin, Germany

²Experimental and Clinical Research Center, a cooperation between the Max Delbrück Center for Molecular Medicine in the Helmholtz Association and Charité Universitätsmedizin Berlin, Berlin, Germany

³Max Delbrück Center for Molecular Medicine in the Helmholtz Association (MDC), Berlin, Germany

⁴Department of Neuropsychiatry and Laboratory of Molecular Psychiatry, Charité – Universitätsmedizin Berlin, corporate member of Freie Universität Berlin and Humboldt-Universität zu Berlin, Berlin, Germany

⁵Technical contact

⁶Lead contact

*Correspondence: ginevra@zedat.fu-berlin.de (G.G.), maria.parr@fu-berlin.de (M.K.P.)
<https://doi.org/10.1016/j.xpro.2022.101715>

SUMMARY

Differences in metabolic profiles can link to functional changes of immune cells in disease conditions. Here, we detail a protocol for the detection and quantitation of 19 metabolites in one analytical run. We provide the parameters for chromatographic separation and mass spectrometric analysis of isotopically labeled and unlabeled metabolites. We include steps for incubation and sample preparation of PBMCs and monocytes. This protocol overcomes the chromatographic challenges caused by the chelating properties of some metabolites.

BEFORE YOU BEGIN

Institutional permissions

The protocol involves human immune cells and, therefore, the approval of the ethical committee is necessary before starting the analysis. The study was registered and approved by the Ethics Commission of Charité–Universitätsmedizin Berlin (Ethikkommission der Charité–Universitätsmedizin Berlin; registration number EA1/187/17), Berlin, Germany.

This protocol can be applied to the incubation of different cell types. The following paragraphs will show its application to the analysis and quantitation of the metabolites extracted from peripheral blood mononuclear cells (PBMCs) and monocytes.

Metabolic pathway(s), related metabolites, and cell type of interest should be identified before performing an experiment. It should be taken into consideration that different cell types require different culture conditions including the incubation time. For example, human cell lines are in general more stable than human primary cells (e.g., human PBMCs) and thus can commonly be longer incubated *in vitro*.

Another aspect to take into consideration is that if the analysis involves a labeled precursor, an enrichment of isotope-labeled metabolites is generally required. In this protocol, we were interested in assessing glucose metabolism in human PBMCs and monocytes (primary cells) using ¹³C-labeled glucose. Therefore, the cells had to be cultured in ¹²C-glucose-free medium supplemented with ¹³C-glucose for 4–6 h (an exact incubation time should be first validated) for an





enrichment of ^{13}C -labeled metabolites derived from glucose. Of note, every metabolic pathway requires a specific time to convert the precursor into related metabolites. The glycolytic intermediates are usually produced within minutes from the introduction of labeled glucose, while those of the tricarboxylic acid (TCA) cycle will need several hours (Buescher et al., 2015).

Finally, it is also challenging to distinguish metabolites that are present both in the culture medium and intracellular compartment, such as amino acids (Shlomi et al., 2014), pyruvate, or lactate (Quek et al., 2016). This continuous exchange between extra- and intracellular compartment may interfere with the incorporation of the labeled precursor and, therefore, in the determination of the metabolic fluxes.

Regarding glucose metabolism, some of the metabolites involved in the TCA cycle, glycolysis, and pentose phosphate pathway are phosphorylated substances and, therefore, are good chelating agents. The same applies to citric acid. In terms of analytics, that means a broad chromatographic peak, when even a chromatographic peak is obtainable. To overcome this issue, it is necessary to passivate the entire system with a phosphoric acid wash, as will be described in step-by-step method details. In addition, the InfinityLab deactivator (medronic acid) must be added to both mobile phase constituents. The use of alternative chelating additives to improve the peak shapes of metal-sensitive analytes has been reported, especially EDTA and other ion-pairing reagents. These alternatives, however, present some problems such as ion suppression or longer persistence in the column and the HPLC system (Hsiao et al., 2018; Pesek et al., 2011).

^{12}C -glucose-free medium supplemented with 1,2- $^{13}\text{C}_2$ -glucose

⌚ Timing: 5 min

1. Add 10% fetal bovine serum (FBS) to Dulbecco's Modified Eagle's Medium (DMEM), without glucose, pyruvate, glutamine, and phenol red (e.g., for the incubation of 40 million PBMCs, add 1 mL of FBS to 9 mL of DMEM).
2. Add 1,2- $^{13}\text{C}_2$ -D-glucose in 1. to a final concentration of 4.5 g/L.

Culture medium with unlabeled glucose

⌚ Timing: 5 min

3. Add 10% FBS in DMEM, without glucose, pyruvate, glutamine, and phenol red.
4. Add unlabeled glucose (^{12}C -glucose) to the culture medium (3) to a final concentration of 4.5 g/L.

Passivation solution: 0.5% phosphoric acid wash

⌚ Timing: 10 min

5. Add 0.5% ortho-phosphoric acid (H_3PO_4) to 90% acetonitrile (ACN) and 10% water.

To obtain 0.5 L of phosphoric acid washing solution, mix 450 mL of ACN, 50 mL of H_2O , and 2.5 mL of H_3PO_4 (85%).

⚠ CRITICAL: Ortho-phosphoric acid (H_3PO_4) 85% causes severe skin burns and serious eyes damages. Use suitable chemical protection gloves and goggles while handling it. It is also corrosive to metals, avoid contact.

⚠ CRITICAL: ACN is toxic by oral ingestion, dermal contact, and inhalation. It also causes eye irritation. Always use gloves, google, and lab coat and work under fume hood while handling it.

STAR Protocols Protocol



Ammonium acetate ($\text{CH}_3\text{COONH}_4$) buffer stock solution

⌚ Timing: 15 min

6. Prepare a 100 mM solution of $\text{CH}_3\text{COONH}_4$ in H_2O . To obtain 0.5 L of buffer stock solution weigh 3.85 g of $\text{CH}_3\text{COONH}_4$ and bring to volume in a 0.5 L volumetric flask.
7. Adjust pH with ammonia solution (NH_3) to pH 9.

⚠ **CRITICAL:** NH_3 causes severe skin burns and eye damage. Always wear gloves, google, and lab coat while handling it. It may cause respiratory irritation. Work under fume hood. It may be corrosive to metals, avoid contact. It is very toxic to aquatic life and with long lasting effects. Avoid release to the environment.

KEY RESOURCES TABLE

REAGENT or RESOURCE	SOURCE	IDENTIFIER
Biological samples		
PBMCs	The German Red Cross	www.drk.de
Chemicals, peptides, and recombinant proteins		
InfinityLab Deactivator Additive	Agilent	Cat#5191-3940
RPMI 1640 Medium	Gibco™	Cat#21875034
DMEM, no glucose, no glutamine, no phenol red	Thermo Fisher Scientific	Cat#A1443001
Acetyl-Coenzyme A Trilithium Salt BioChemica	PanReac AppliChem ITW Reagents	Cat#A3753
[1- ^{13}C] Adenosine 5'-monophosphate (disodium salt)	Omicron Biochemicals, Inc.	Cat#NCT-001
Adenosine 5'-monophosphate monohydrate	Sigma-Aldrich	Cat#A2252
Adenosine 5'-triphosphate (ATP) disodium salt hydrate	Sigma-Aldrich	Cat#A1852
Citric acid	Sigma-Aldrich	Cat#251275
D-Fructose 6-phosphate disodium salt hydrate	Sigma-Aldrich	Cat#F3627
D-Glucose	Sigma-Aldrich	Cat#G7021-1KG
D-Glucose-1,2- $^{13}\text{C}_2$	Sigma-Aldrich	Cat#453188
DL-Glyceraldehyde 3-phosphate solution	Sigma-Aldrich	Cat#G5251
Glycine	Sigma-Aldrich	Cat#94119
Glycine (2- ^{13}C , 99%)	Eurisotop	Cat#CLM-136
L-Glutamic acid (1,2- $^{13}\text{C}_2$, 99%)	Cambridge Isotope Laboratories, Inc.	Cat#CLM-2024-PK
L-Glutamic acid hydrochloride	Sigma-Aldrich	Cat#G2128
L-Glutamine (1,2- $^{13}\text{C}_2$, 99%)	Cambridge Isotope Laboratories, Inc.	Cat#CLM-2001-PK
Glutamine	United States Pharmacopeia (USP) Reference Standard	Cat#1294808
Sodium L-lactate	Sigma-Aldrich	Cat#L7022
Sodium pyruvate	Sigma-Aldrich	Cat#P5280
Sodium pyruvate-2,3- $^{13}\text{C}_2$	Sigma-Aldrich	Cat#486191
D-(-)-3-Phosphoglyceric acid (disodium salt)	Sigma-Aldrich	Cat#P8877
D-Ribose 5-phosphate disodium salt dihydrate	Sigma-Aldrich	Cat#83875
DL-Serine	Sigma-Aldrich	Cat#68353
Acetonitrile (LC-MS grade $\geq 99.9\%$)	Fisher Scientific	Cat#326810025
Ammonium acetate ($\geq 99\%$)	VWR Chemicals	Cat#84885.180
Ortho-phosphoric acid 85%	Merck	Cat#1.00563
NH_3 solution 25% for LC-MS LiChropur®	Merck	Cat#5330030050
Benzonase nuclease	Sigma-Aldrich	Cat#E1014-25KU
Monensin solution (1000x)	BioLegend	Cat#420701

(Continued on next page)



Continued

REAGENT or RESOURCE	SOURCE	IDENTIFIER
FBS (heat inactivated)	Gibco™	Cat#10082147
LPS from E. coli O111:B4	Sigma-Aldrich	Cat#L4391-1MG
PBS (DPBS, no calcium, no magnesium)	Gibco™	Cat#14200-067
Critical commercial assays		
MACS (Pan Monocyte Isolation Kit (human))	Miltenyi Biotec	Cat#130-096-537
Software and algorithms		
MassHunter 10 Quantitative Analysis program G3336	Agilent Technologies	https://www.agilent.com/
MassHunter 10 Acquisition software G3335	Agilent Technologies	https://www.agilent.com/
ChemDraw Professional 18.0	PerkinElmer	https://www.perkinelmer.com/category/chemdraw
Prism 9	GraphPad	https://www.graphpad.com/updates/prism-900-release-notes
Other		
1290 Infinity II LC System	Agilent Technologies	N/A
InfinityLab Poroshell 120 HILIC-Z, 2.1 × 100 mm, 2.7 μm, PEEK lined	Agilent Technologies	Cat#675775-924
1290 Infinity II in-line filter, 0.3 μm, 2 mm ID, SST	Agilent Technologies	Cat# 5067-6189
6495 QqQ with AJS-ESI source	Agilent Technologies	N/A
Water purification system LaboStar™ 2-DI-UV	LaboStar®	Cat#2206/2207
Membrane filter, non-sterile, nylon, 0.2 μm, 47 mm	Thermo Scientific	Cat#DS0215-4020
Syringe filters ROTILABO®, cellulose acetate (CA), 0.2 μm, 25 mm, sterile	Roth	Cat#KC70.1

MATERIALS AND EQUIPMENT

LC-MS setting

For this protocol an Agilent 1290 Infinity II HPLC system was hyphenated to an Agilent 6495 QqQ mass spectrometer (MS) with an Agilent jet stream source with electrospray ionization (AJS-ESI), both controlled by MassHunter Data Acquisition software (Agilent, Waldbronn, Germany). For the separation of the metabolites, an Agilent InfinityLab Poroshell 120 HILIC-Z column (PEEK-lined, 2.1 × 100 mm, 2.7 μm) was used.

Table 1 shows the HPLC conditions and Table 2 the MS parameters. Fragmentation and source parameters were optimized using Agilent Optimizer and Agilent Source Optimizer software. The acquisition was conducted in dynamic multiple reaction monitoring (dMRM) mode in both, positive and negative mode.

Table 1. HPLC conditions

Autosampler temperature	4°C		
Column temperature	30°C		
Injection volume	1 μL		
Total run time	21 min		
Flow	0.3 mL/min		
Mobile phase A	10 mM CH ₃ COONH ₄ (from stock solution "before you begin 6.-7.") in H ₂ O + 5 μM InfinityLab deactivator additive		
Mobile phase B	10 mM CH ₃ COONH ₄ (from stock solution "before you begin 6.-7.") in ACN + 5 μM InfinityLab deactivator additive		
Gradient	min	Solvent A (%)	Solvent B (%)
	0	10	90
	2	10	90
	12	40	60
	14	40	60
	15	10	90
	20	10	90
	Post-run (1 min)	10	90

STAR Protocols Protocol

CellPress
OPEN ACCESS



Table 2. MS parameters

Agilent 6495 QcQ		
	Positive	Negative
Ionization mode	Positive	Negative
Sheath gas flow (L/min)	12	12
Sheath gas temperature (°C)	350	350
Capillary voltage (V)	4500	3500
Nozzle voltage (V)	750	0
Drying gas temperature (°C)	210	210
Drying gas flow (L/min)	20	20
Nebulizer (psi)	30	30
Funnel	High P RF 190 Low P RF 40	High P RF 110 Low P RF 60

STEP-BY-STEP METHOD DETAILS

This protocol can be applied to different cell cultures. Conditions of cell incubation will need previous evaluation and adjustment.

We show here, the protocols used for the incubation of PBMCs and monocytes.

Two different conditions were used in both cases: with labeled (1,2-¹³C₂-D-glucose) and unlabeled glucose.

PBMC incubation

⌚ Timing: 8–9 h

This part describes experimental steps starting with about 40 million PBMCs.

- Thawing of PBMCs and preparation for the incubation.
 - Warm 10 mL washing medium (10% FBS in Roswell Park Memorial Institute (RPMI) 1640 medium) in a falcon tube to 37°C in a water bath.
 - Warm 5 mL washing medium containing benzonase (25 U/mL) at 37°C in a water bath.
 - Thaw frozen PBMCs (max of 40 × 10⁶ cells) in a water bath (37°C). When almost completely thawed, transfer the cells under sterile condition to the falcon tube containing 10 mL washing medium (a., without benzonase).
 - Centrifuge at 300 × g for 10 min at room temperature, then remove the supernatant.
 - Gently resuspend each cell pellet in 1 mL of warmed medium with benzonase (b.), then add another 4 mL of benzonase medium. Mix well and incubate at 37°C in a water bath for 5 min.
 - Centrifuge at 300 × g for 10 min at room temperature, then remove the supernatant.
- PBMC incubation in an ultra-low attachment 6-well plate.
 - Sterile-filter (with 0.2 μm filter) the medium supplemented with either unlabeled or 1,2-¹³C₂-D-glucose (see the paragraph “before you begin” points 1.–2. or 3.–4).
 - Warm the culture medium (2.a.) to 37°C in a water bath.
 - Gently resuspend each cell pellet (1.f.) in the sterilized, warm medium (2.b.) and adjust the cell concentration to 1 × 10⁶/100 μL.
 - Transfer about 5 × 10⁶ cells (about 500 μL) into an ultra-low attachment surface 6-well plate, add culture medium to a final volume of 1,800 μL.
 - Incubate for 2 h at 37°C, 5% CO₂.
 - Add 200 μL of PBS (negative control) or 200 μL of lipopolysaccharide (LPS) solution (100 ng/mL, as a stimulant). The final volume is 2,000 μL/well.
 - Incubate at 37°C, 5% CO₂ for another 4 h.



CellPress
OPEN ACCESS

STAR Protocols
Protocol

3. Cell harvest.
 - a. Transfer cell suspension into 2 mL Eppendorf tubes.
 - b. Centrifuge at $300 \times g$, for 10 min at 4°C .
 - c. Transfer the supernatant into new tubes, then centrifuge at $15,000 \times g$, for 10 min at 4°C . Take out 1 mL of supernatant and store at -80°C until measurement.
 - d. Shock freeze the cell pellet in liquid N_2 and leave it for 5 min.
 - e. Take out frozen cell pellet from liquid N_2 , then add 100 μL of $\text{H}_2\text{O}:\text{ACN}$ (1:1). Vortex thoroughly and incubate on ice for 5 min.
 - f. Centrifuge at $15,000 \times g$, for 10 min at 4°C .
 - g. Carefully take 75 μL of the supernatant, without disturbing the cell pellet. Store the cell lysate at -80°C .

⚠ CRITICAL: All cell culture experiments should be carried out under laminar flow hood under a sterile condition.

⚠ CRITICAL: The use of human cells for research purposes underlies to ethical restrictions. It is necessary to obtain appropriate approvals before starting the research.

⚠ CRITICAL: Incubation time should be validated prior to experiment (i.e., the incubation time in 2.e. and g. can be varied and tested).

Note: After isolation, PBMCs were stored in liquid N_2 until the experiment.

Optional: In step 2.f other stimulants may be applied instead of LPS.

Monocyte incubation

⌚ Timing: 9–10 h

This step begins with about 40 million PBMCs.

4. Thawing of PBMCs.
 - a. Warm 10 mL of medium (10% FBS in RPMI 1640 medium) in a falcon tube to 37°C in a water bath.
 - b. Warm 5 mL of washing medium containing benzonase (25 U/mL) at 37°C in a water bath.
 - c. Thaw frozen PBMCs (max of 40×10^6 cells) in a water bath (37°C). When almost completely thawed, transfer the cells under sterile condition to the falcon tube containing 10 mL washing medium (a., without benzonase).
 - d. Centrifuge at $300 \times g$ for 10 min at room temperature, then remove the supernatant.
 - e. Gently resuspend each cell pellet in 1 mL of warmed medium with benzonase (b.), then add another 4 mL of benzonase medium. Mix well and incubate at 37°C in a water bath for 5 min.
 - f. Centrifuge at $300 \times g$ for 10 min at room temperature, then remove the supernatant.
5. Separation of monocytes with the magnetic-activated cell sorting (MACS) (negative selection approach using Pan Monocyte Isolation Kit, human).
 - a. Prior to MACS sorting, put the LS column at -20°C , to minimize unspecific binding.
 - b. Wash the cell pellet (4.f.) with 1 mL of MACS buffer (0.5% BSA in PBS containing 2 mM EDTA) and transfer to 1.5 mL Eppendorf tubes.
 - c. Centrifuge at $300 \times g$, for 10 min at 4°C , then take out the supernatant.
 - d. Resuspend the cell pellet in 400 μL of MACS buffer (for 5×10^6 cells).
 - e. Add 100 μL of FcR blocking reagent (for 5×10^6 cells).
 - f. Add 100 μL of biotin-antibody cocktail (for 5×10^6 cells).
 - g. Mix well and incubate for 5 min in the refrigerator (2°C – 8°C).
 - h. Add 300 μL of MACS buffer (for 5×10^6).

STAR Protocols

Protocol

CellPress
OPEN ACCESS



- i. Add 200 μL of anti-biotin micro beads (for 5×10^6 cells).
 - j. Mix well and incubate for 10 min in the refrigerator (2°C – 8°C).
 - k. Wash with 1 mL of MACS buffer.
 - l. Centrifuge at $300 \times g$, for 10 min at 4°C , take out the supernatant, and then resuspend the cell pellet with 500 μL MACS buffer.
 - m. Place the LS column in the magnetic field of a MACS separator.
 - n. Precondition the column by rinsing with 3 mL of MACS buffer.
 - o. Load the cell suspension (l.) onto the column through the pre-separation filter.
 - p. Collect flow-through, which contains unlabeled cells, representing the enriched pan-monocytes.
 - q. Wash column with 3×3 mL of MACS buffer and combine all four flow-through.
 - r. Take an aliquot of 10 μL for cell count, then centrifuge the remaining cells at $300 \times g$, for 10 min at 4°C and remove supernatant.
6. Monocytes incubation in an ultra-low attachment 24-well plate.
- a. Sterile-filter (with 0.2 μm filter) the medium supplemented with either unlabeled or $1,2\text{-}^{13}\text{C}_2$ -D-glucose (see the paragraph “before you begin”).
 - b. Warm the culture medium to 37°C in a water bath.
 - c. Gently resuspend each cell pellet (5.r.) in the sterilized, warm medium (6.b.) and adjust the cell concentration to ca. $8 \times 10^5/100 \mu\text{L}$.
 - d. Transfer about 8×10^5 cells (about 100 μL) of cell suspension into an ultra-low attachment surface 24-well plate and add culture medium to a final volume of 300 μL .
 - e. Add 0.3 μL of Monensin per well.
 - f. Incubate for 5 h at 37°C , 5% CO_2 .
7. Cell harvest.
- a. Transfer cell suspension in 2 mL Eppendorf tubes.
 - b. Centrifuge at $300 \times g$, for 10 min at 4°C .
 - c. Separate the supernatant from the cell pellet (attention not to disturb cell pellet; do not aliquot the entire volume of supernatant). To analyze the culture medium, centrifuge it at $15,000 \times g$, for 10 min at 4°C before LC-MS analysis.
 - d. Shock freeze the cell pellet into liquid N_2 and leave it for 5 min.
 - e. Take out from liquid N_2 and add 100 μL of $\text{H}_2\text{O}:\text{ACN}$ (1:1).
 - f. Vortex thoroughly and incubate on ice for 5 min.
 - g. Centrifuge at $15,000 \times g$, for 10 min at 4°C .
 - h. Carefully take 75 μL of the supernatant, without disturbing the cell pellet to obtain the samples of cell extract.
 - i. Put the samples at -80°C or on dry ice.

△ **CRITICAL:** The incubation of monocytes is particularly delicate in a culture medium without pyruvate and glutamine. Verify regularly during the incubation the well-being of the cells and consider that reaching the isotopic steady state might be challenging.

△ **CRITICAL:** All cell culture experiments should be carried out under laminar flow box in a sterile environment.

△ **CRITICAL:** The use of human cells for research purposes underlies to ethical restrictions. It is necessary to obtain appropriate approvals before starting the research.

Note: After collection and before the incubation, PBMCs from where monocytes were extracted, were stored at -80°C .

Optional: In step 6.e different stimulants can be used, for instance, LPS to simulate different incubation conditions.



Preparation of mobile phases

⌚ Timing: 15 h

8. Deactivation solution A (mobile phase A: 10 mM CH₃COONH₄ in H₂O + InfinityLab deactivator additive).
 - a. To obtain 1 L of mobile phase A, add 100 mL of CH₃COONH₄ stock solution (“before you begin”) to 900 mL of milli-Q water.
 - b. Add 1 mL of InfinityLab deactivator additive per liter of mobile phase (final concentration of 5 μM).
 - c. Let it rest overnight at room temperature.
 - d. Filter with a 2 μm filter (non-sterile, nylon, 0.2 μm, 47 mm).
 - e. Sonicate the mobile phase for 5–10 min to degas.
9. Deactivation solution B (mobile phase B: 10 mM CH₃COONH₄ in ACN + InfinityLab deactivator additive).
 - a. To obtain 1 L of mobile phase B, add 100 mL of CH₃COONH₄ stock solution (“before you begin”) to 900 mL of LC-MS grade ACN.
 - b. Add 1 mL of InfinityLab deactivator additive per liter of mobile phase (final concentration of 5 μM).
 - c. Let it rest overnight at room temperature.
 - d. Filter with a 2 μm filter (non-sterile, nylon, 0.2 μm, 47 mm).
 - e. Sonicate the mobile phase for 5–10 min to degas.

⚠ CRITICAL: There might be some precipitation in the mobile phases, especially in the organic one (B). It is recommended to add the buffer stock solution slowly to the ACN, and only after 10–15 min the InfinityLab deactivator additive.

⚠ CRITICAL: ACN is toxic by oral ingestion, dermal contact, and inhalation. It also causes eye irritation. Always use gloves, google, and lab coat and work under fume hood while handling it.

Passivation and conditioning of the system

⌚ Timing: 18–19 h

The passivation and conditioning of the system was conducted accordingly to Agilent’s protocol for the use of the InfinityLab deactivator (Agilent Technologies, 2018).

10. Phosphoric acid wash.
 - a. Put milli-Q water as mobile phase for both channels.
 - b. Purge the system for 5 min at 5 mL/min directly to waste. If the system does not have a purge valve, momentarily detach the column, and put the inlet capillary to a waste container.
 - c. Set the flow of milli-Q water to 0.25 mL/min and run for 30 min through the system and the column.
 - d. Change the flow rate to 0 mL/min.
 - e. Take out the spray needle from the MS source and fix it vertically in a waste container (Figure 1). Do not inject phosphoric acid wash in the MS.
 - f. Switch the solvent in both channels to the 0.5% phosphoric acid wash (“before you begin: passivation solution: 0.5% phosphoric acid wash”).
 - g. Purge the system, for 5 min at 5 mL/min with the phosphoric acid wash.
 - h. Set the flow of 0.5% phosphoric acid wash to 0.1 mL/min and run for 14 h.
 - i. Change the flow rate to 0 mL/min.
 - j. Switch the solvent in both channels to milli-Q water.

STAR Protocols
ProtocolCellPress
OPEN ACCESS

Figure 1. Waste container and holder for the spray needle during the passivation of the HPLC-MS system

- k. Purge the system at 5 mL/min for 10 min with milli-Q water.
- l. Set the flow of milli-Q water to 0.25 mL/min and run for 1 h through the system and the column.
- m. Change the flow rate to 0 mL/min.
- n. Switch the solvent to mobile phase A and B ("mobile phases preparation").
- o. Purge the system with mobile phases A and B (50:50) at 5 mL/min for 5 min.
- p. Reinstall the spray needle into the MS.

Δ **CRITICAL:** Take out the spray needle from the MS during the phosphoric acid wash. Do not inject phosphoric acid into the MS.

Δ **CRITICAL:** During the passivation keep the spray needle in a vertical position, as shown in Figure 1, and let the sheath gas flow to prevent the formation of persistent drops of phosphoric wash along the capillary.

11. Column conditioning.
 - a. Set the flow of the mobile phase to 0.2 mL/min (60% A – 40% B) and run for 30 min through the system and column.
 - b. Set the flow of the mobile phase to 0.3 mL/min (60% A – 40% B) and run for 15 min through the system and column.
 - c. Change the composition to 50% A – 50% B and run for 30 min through the system and column.
 - d. Change the composition to 10% A – 90% B and run for at least 1 h through the system and column.

Δ **CRITICAL:** The step-by-step increase of the percentage of mobile phase B, minimizes the risk of precipitate formation in the system.

HPLC-MS analysis

⊙ **Timing:** 21 min per run

12. After conditioning of the analytical column, it is possible to start the analysis.



Table 3. dMRM method details for target analytes

Compound	Ionization	RT (min)	Quantifier (transition)	CE (eV)	Qualifier (transitions)	CE (eV)
2,3- ¹³ C ₂ pyruvate	[M-H] ⁻	1.48	89.1 → 45.2	4		
pyruvate	[M-H] ⁻	1.48	87.0 → 43.2	4		
1,2- ¹³ C ₂ lactate	[M-H] ⁻	2.15	91.1 → 45.2	8	91.1 → 44.2	8
					91.1 → 43.1	32
lactate	[M-H] ⁻	2.15	89.0 → 43.2	8	89.0 → 41.1	32
2- ¹³ C glycine	[M+H] ⁺	4.64	77.1 → 30.4	12		
glycine	[M+H] ⁺	4.64	76.0 → 30.3	12		
2,3- ¹³ C ₂ serine ^{a,b}	[M+H] ⁺	4.77	108.1 → 62.0	12	108.1 → 44.2	28
					108.1 → 31.3	28
2,3- ¹³ C ₂ serine ^{a,b}	[M-H] ⁻	4.77	106.1 → 75.0	8		
serine	[M+H] ⁺	4.77	106.1 → 60.2	12	106.1 → 42.2	28
					106.1 → 30.3	28
serine ^a	[M-H] ⁻	4.77	104.0 → 74.0	8		
1,2- ¹³ C ₂ glutamine	[M+H] ⁺	4.79	149.1 → 85.0	16	149.1 → 131.8	8
					149.1 → 57.1	36
1,2- ¹³ C ₂ glutamine ^a	[M-H] ⁻	4.79	147.1 → 128.9	8	147.1 → 42.1	36
glutamine	[M+H] ⁺	4.79	147.1 → 84.0	16	147.1 → 130.0	8
					147.1 → 56.0	36
glutamine ^a	[M-H] ⁻	4.79	145.0 → 126.9	8	145.0 → 42.1	36
1,2- ¹³ C ₂ glutamic acid	[M+H] ⁺	6.51	150.1 → 85.1	16	150.1 → 102.9	8
					150.1 → 57.1	32
					150.1 → 42.1	28
1,2- ¹³ C ₂ glutamic acid ^a	[M-H] ⁻	6.51	148.1 → 130.0	8	148.1 → 104.0	12
glutamic acid	[M+H] ⁺	6.51	148.0 → 84.0	16	148.0 → 101.9	8
					148.0 → 56.1	32
glutamic acid ^a	[M-H] ⁻	6.51	146.0 → 102.0	12	146.0 → 128.1	8
1- ¹³ C AMP	[M+H] ⁺	6.83	349.1 → 135.9	16	349.1 → 118.9	64
					349.1 → 98.0	32
1- ¹³ C AMP ^a	[M-H] ⁻	6.83	347.1 → 79.0	28	347.1 → 133.9	36
					347.1 → 97.0	24
AMP	[M+H] ⁺	6.83	348.0 → 135.9	16	348.0 → 118.9	64
					348.0 → 96.8	32
AMP ^a	[M-H] ⁻	6.83	346.0 → 79.0	28	346.0 → 133.9	36
					346.0 → 97.0	24
1- ¹³ C acetyl CoA	[M+H] ⁺	7.57	811.2 → 304.1	20	811.2 → 428.1	20
					811.2 → 158.8	64
					811.2 → 135.8	48
acetyl CoA	[M+H] ⁺	7.57	810.1 → 303.1	20	810.1 → 428.1	20
					810.1 → 158.8	64
					810.1 → 135.8	48
1- ¹³ C ribose-5-phosphate ^a	[M-H] ⁻	7.53	230.1 → 96.9	16	230.1 → 138.9	12
					230.1 → 79.0	40
ribose 5-phosphate	[M-H] ⁻	7.53	229.0 → 96.9	16	229.0 → 138.9	12
					229.0 → 79.0	40
ribose 5-phosphate ^a	[M+H] ⁺	7.53	231.0 → 97.0	12		
2,3- ¹³ C ₂ glyceraldehyde 3-phosphate ^a	[M+H] ⁺	7.67	173.0 → 99.0	20		
2,3- ¹³ C ₂ glyceraldehyde 3-phosphate ^{a,b}	[M-H] ⁻	7.67	171.0 → 79.1	20		
glyceraldehyde 3-phosphate	[M+H] ⁺	7.67	171.0 → 99.0	20		
glyceraldehyde 3-phosphate ^a	[M-H] ⁻	7.67	169.0 → 79.1	20		
1,2- ¹³ C ₂ fructose 6-phosphate	[M-H] ⁻	7.78	261.1 → 97.0	20	261.1 → 169.0	8
					261.1 → 139.0	12
					261.1 → 78.9	52
fructose 6-phosphate	[M-H] ⁻	7.78	259.0 → 97	20	259.0 → 169.0	8
					259.0 → 139.0	12
					259.0 → 78.9	52

(Continued on next page)

STAR Protocols Protocol

CellPress
OPEN ACCESS

Table 3. Continued

Compound	Ionization	RT (min)	Quantifier (transition)	CE (eV)	Qualifier (transitions)	CE (eV)
1,2- ¹³ C ₂ phosphoglyceric acid	[M+H] ⁺	8.50	189.0 → 98.9	16	189.0 → 80.9 189.0 → 64.9	44 76
1,2- ¹³ C ₂ phosphoglyceric acid ^b	[M-H] ⁻	8.50	187.0 → 78.9	40	187.0 → 96.8	12
phosphoglyceric acid	[M+H] ⁺	8.50	187.0 → 98.9	16	187.0 → 80.9 187.0 → 62.9	44 76
phosphoglyceric acid ^b	[M-H] ⁻	8.50	185.0 → 78.9	40	185.0 → 96.8	12
1- ¹³ C ATP	[M+H] ⁺	8.38	509.1 → 136.0	24	509.1 → 411.0	16
1- ¹³ C ATP ^b	[M-H] ⁻	8.38	507.1 → 158.6	32	507.1 → 409.0 507.1 → 134.0	20 40
ATP	[M+H] ⁺	8.38	508.0 → 136.0	24	508.0 → 410.0	16
ATP ^b	[M-H] ⁻	8.38	506.0 → 158.6	32	506.0 → 407.9 506.0 → 134.0	20 40
1,2- ¹³ C ₂ citric acid	[M-H] ⁻	8.54	193.1 → 87.0	12	193.1 → 113.0 193.1 → 87.0 193.1 → 85.0 193.1 → 67.0	12 16 12 24
citric acid	[M-H] ⁻	8.54	191.0 → 111.0	12	191.0 → 87.0 191.0 → 85.0 191.0 → 67.0	16 12 24

^aTransition/transitions used only for confirmation, not for quantitation.

^bTransition/transitions were not experimentally confirmed due to a lack of appropriate reference material but hypothesized from the fragmentation pattern of the relative unlabeled compound.

Table 3 shows the details of the dMRM method.

△ **CRITICAL:** Always run a couple of blanks before starting the analysis to be sure that the column is well conditioned and the pressure stable. Be aware that analysis with HILIC needs longer column conditioning.

△ **CRITICAL:** There might be some precipitation in the mobile phases. To our knowledge there is no suitable pre-column for both conditions of phosphoric wash and pH 9 analysis, thus the use of an in-line filter is recommended to preserve the column.

Troubleshooting 1 → Problem 1: Precipitation in the mobile phases.

If precipitation occurs in the mobile phases (particularly in B) there will be some drops in the pressure curve of the instrument. See the protocol section "troubleshooting, problem 1" for more details.

EXPECTED OUTCOMES

Data were obtained from the incubation of PBMCs and monocytes. Figure 2 shows the metabolic pathways considered, and the intermediate metabolites highlighted in red were identifiable and quantifiable in this study. The incubation of 5 million PBMCs was conducted in two different conditions: with unlabeled glucose and 1,2-¹³C₂ labeled glucose. The amounts of the above-mentioned metabolites after incubation with glucose are shown in Figure 3 (unlabeled glucose) and Figure 4 (labeled glucose). As result, most of the labeled glucose was transformed into lactate and barely reached the TCA cycle. As discussed before, the labeled glucose may require several hours to reach the TCA cycle.

The incubation of 5 million PBMCs with unlabeled glucose (Figure 3) allowed for the detection and quantitation in the cell lysate of pyruvate, glycine, serine, glutamine, glutamic acid, AMP, 1-¹³C AMP, fructose 6-phosphate, ATP, 1-¹³C ATP, phosphoglyceric acid, citric acid, and lactate. The presence of labeled AMP and ATP is expected and justified by the natural abundance of the ¹³C

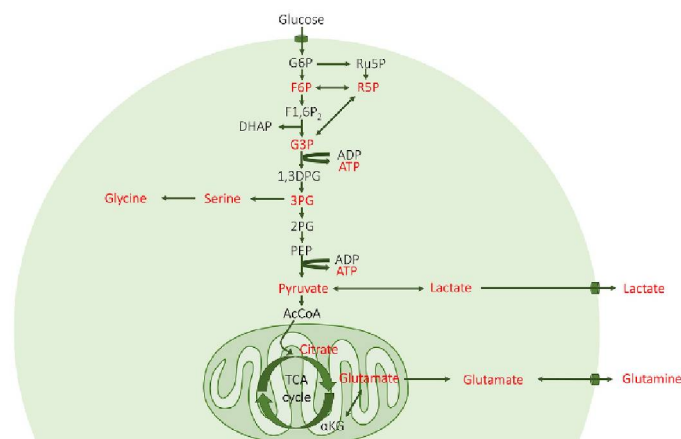


Figure 2. Metabolic pathways considered in this study

The compounds highlighted in red were detectable and quantifiable.

isotope on earth. In fact, the higher number of carbons in ATP and AMP increases the probability of finding heavy isotope in these molecules. The incubation of 5 million PBMCs with $1,2\text{-}^{13}\text{C}_2$ labeled glucose (Figure 4) allowed for the detection and quantitation in the cell lysate of pyruvate, glycine, serine, glutamine, $1,2\text{-}^{13}\text{C}_2$ glutamine, glutamic acid, $1,2\text{-}^{13}\text{C}_2$ glutamic acid, AMP, $1\text{-}^{13}\text{C}$ AMP, fructose 6-phosphate, $1,2\text{-}^{13}\text{C}_2$ fructose 6-phosphate, ATP, $1\text{-}^{13}\text{C}$ ATP, phosphoglyceric acid, $1,2\text{-}^{13}\text{C}_2$ phosphoglyceric acid, citric acid, lactate, and $1,2\text{-}^{13}\text{C}_2$ lactate.

Monocytes ($N=8 \times 10^5$) were incubated in two different conditions: without a stimulation, therefore only with medium (CON) and with the addition of lipopolysaccharides (LPS). Both, cell extract and medium of the incubation, were analyzed.

These incubations allowed for the detection and quantitation in the cell lysate of pyruvate, glycine, serine, glutamine, $1,2\text{-}^{13}\text{C}_2$ glutamine, glutamic acid, AMP, $1\text{-}^{13}\text{C}$ AMP, ATP, lactate, $1,2\text{-}^{13}\text{C}_2$ lactate, and citric acid (Figures 5 and 6 show, respectively, the unlabeled and labeled analytes).

In the medium of incubation were detected and quantified pyruvate, $2,3\text{-}^{13}\text{C}_2$ pyruvate, glycine, serine, glutamine, $1,2\text{-}^{13}\text{C}_2$ glutamine, glutamic acid, AMP, $1\text{-}^{13}\text{C}$ AMP, lactate, $1,2\text{-}^{13}\text{C}_2$ lactate, and citric acid (Figures 7 and 8 show, respectively, the unlabeled and labeled analytes).

The presence of lactate, glutamine, and amino acids in the incubation medium is not unexpected. On the contrary, the detection of glutamic acid, pyruvate, and citric acid is a warning sign of the well-being of the cells. These compounds cannot pass through the cell membrane, and therefore, their presence in the medium is probably due to the disruption of the membrane after the death of the cells.

In conclusion, this protocol allowed the detection and quantitation of specific compounds that are necessary to have a general overview of the well-being or the metabolic alterations of the cells. Depending on the focus of the future research and on the typology of cells used, the protocol might need adaptations. We gave an example of application to the analysis of PBMCs and monocytes, highlighting pros and cons of the method.

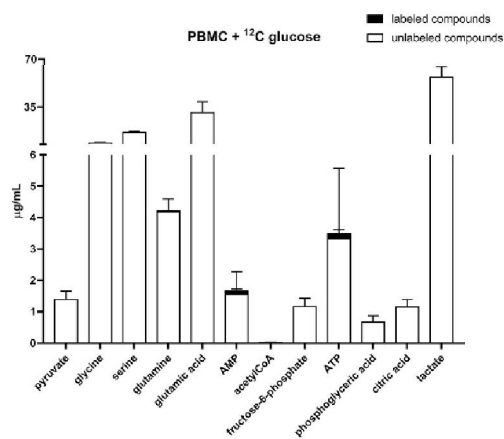


Figure 3. Cell extract from the incubation of PBMCs for 6 h with unlabeled glucose

The white bars show the amounts of unlabeled analytes quantified in the cell extract of 5 million PBMCs. The black bars on top of the unlabeled compounds, show the detected labeled analytes. In this case only $1\text{-}^{13}\text{C}$ AMP and $1\text{-}^{13}\text{C}$ ATP were detected because of their masses and the natural abundance of ^{13}C . The experiments were conducted in triplicates. Data are represented as mean \pm SD.

QUANTIFICATION AND STATISTICAL ANALYSIS

The method was validated based on the ICH guideline M10 on bioanalytical method validation (EMA, 2019).

Since the matrix used is rare (PBMCs and monocytes), the validation was performed in double blanks (ACN:H₂O), except for the matrix effect and the recovery study. Therefore, stock solutions and

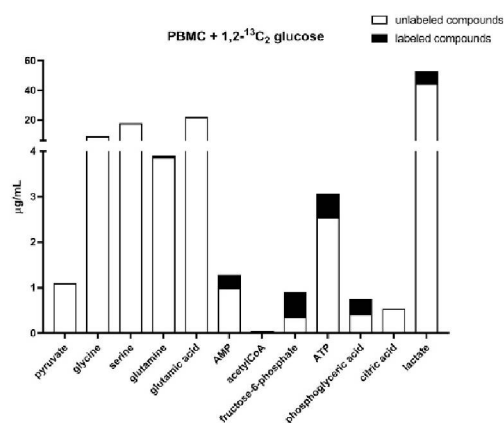


Figure 4. Cell extract from the incubation of PBMCs for 6 h with $1,2\text{-}^{13}\text{C}_2$ labeled glucose

The white bars show the amounts of unlabeled analytes quantified in the cell extract of 5 million PBMCs. The black bars on top of the unlabeled compounds, show the corresponding labeled analytes detected and quantified. The experiment was conducted in one replicate.



STAR Protocols
Protocol

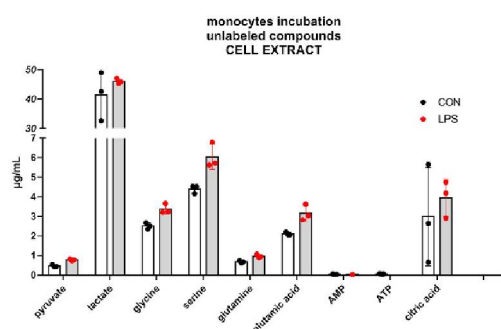


Figure 5. Concentration of unlabeled compounds in the cell lysate

The incubation was performed with 8×10^5 monocytes for 5 h with the addition of $1,2\text{-}^{13}\text{C}_2$ glucose to the medium. The incubation was conducted in two different conditions: without stimulation (CON) and with the addition of LPS (LPS). The experiments were conducted in triplicates. All data points are illustrated in the graphic, and the bars represent the mean value \pm SD.

quality control solutions (QCs) of each standard were prepared with a concentration of 1 mg/mL in ACN:H₂O (1:1) and stored at -80°C .

Specificity/selectivity

The chromatographic run of 21 min and the fragmentation patterns permitted the separation of 19 compounds between labeled and unlabeled: $2,3\text{-}^{13}\text{C}_2$ pyruvate, pyruvate, lactate, $2\text{-}^{13}\text{C}$ glycine, glycine, serine, $1,2\text{-}^{13}\text{C}_2$ glutamine, glutamine, $1,2\text{-}^{13}\text{C}_2$ glutamic acid, glutamic acid, $1\text{-}^{13}\text{C}$ AMP, AMP, acetyl CoA, ribose-5-phosphate, glyceraldehyde-3-phosphate, fructose-6-phosphate, phosphoglyceric acid, ATP, and citric acid.

Some of the targeted analytes, such as $1,2\text{-}^{13}\text{C}_2$ lactate, $2,3\text{-}^{13}\text{C}_2$ serine, $1\text{-}^{13}\text{C}$ acetylCoA, $1\text{-}^{13}\text{C}$ ribose-5-phosphate, $2,3\text{-}^{13}\text{C}_2$ glyceraldehyde, $1,2\text{-}^{13}\text{C}_2$ fructose-6-phosphate, $1,2\text{-}^{13}\text{C}_2$ phosphoglyceric acid, $1\text{-}^{13}\text{C}$ ATP, and $1,2\text{-}^{13}\text{C}_2$ citric acid are not commercially available to our knowledge. It is assumed, that the retention times of the labeled compounds are the same of the corresponding

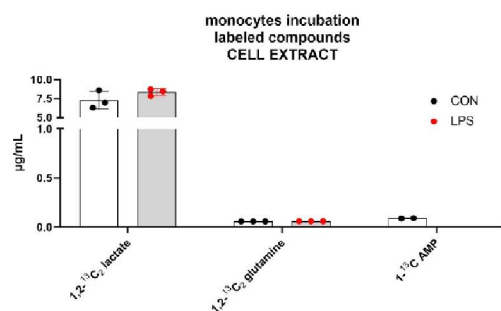


Figure 6. Concentration of labeled compounds in the cell lysate

The incubation was performed with 8×10^5 monocytes for 5 h with the addition of $1,2\text{-}^{13}\text{C}_2$ glucose to the medium. The incubation was conducted in two different conditions: without stimulation (CON) and with the addition of LPS (LPS). The experiments were conducted in triplicates. All data points are illustrated in the graphic, and the bars represent the mean value \pm SD.

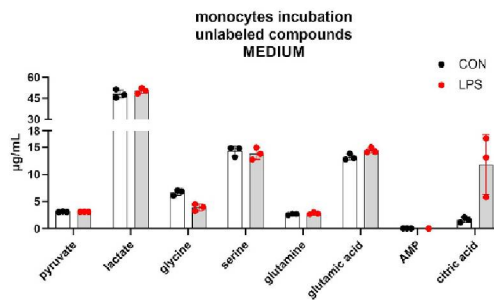


Figure 7. Concentration of unlabeled compounds in the incubation medium
The incubation was performed with 8×10^5 monocytes for 5 h with the addition of $1,2\text{-}^{13}\text{C}_2$ glucose to the medium. The incubation was conducted in two different conditions: without stimulation (CON) and with the addition of LPS (LPS). The experiments were conducted in triplicates. All data points are illustrated in the graphic, and the bars represent the mean value \pm SD.

unlabeled ones, allowing for the identification of the targeted analyte. The suitable transitions were hypothesized based on fragmentation patterns of the unlabeled analytes. For some of them (lactate, fructose-6-phosphate, phosphoglyceric acid, ATP) the fragmentation patterns were confirmed by the results of the cell extract of PBMCs.

Figure 9 shows the general chromatogram of the unlabeled substances. The retention times of the relative labeled substances are virtually the same. Those analytes that could not be chromatographically separated could be distinguished by different MRM transitions as shown in Table 3.

Some compounds present in the matrix show the same molecular weight and the same ion transitions and, therefore, cause interference in the identification and quantitation. This is the case for glucose-6-phosphate and fructose-6-phosphate that have the same precursor and the same product ions and the transitions are listed in Table 3. As shown in Figure 10 though, they are chromatographically separated.

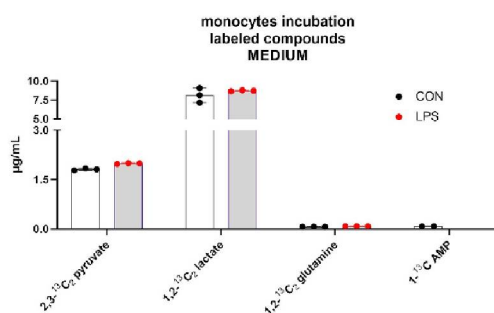


Figure 8. Concentrations of labeled compounds in the incubation medium
The incubation was performed with 8×10^5 monocytes for 5 h with the addition of $1,2\text{-}^{13}\text{C}_2$ glucose to the medium. The incubation was conducted in two different conditions: without stimulation (CON), with the addition of LPS (LPS). The experiments were conducted in triplicates. All data points are illustrated in the graphic, and the bars represent the mean value \pm SD.



CellPress
OPEN ACCESS

STAR Protocols
Protocol

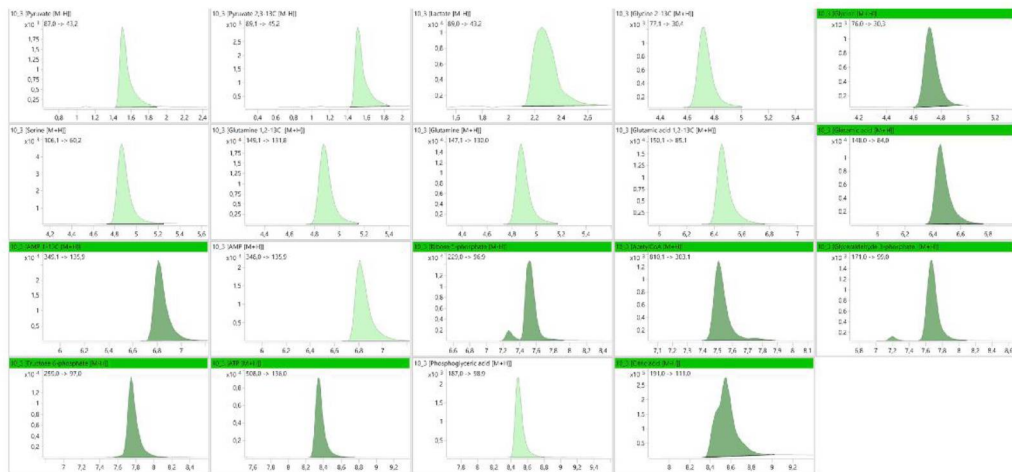


Figure 9. Chromatogram of a double blank spiked with standards of the targeted analytes

The considered references are the following (from upper left to lower right): pyruvate, lactate, glycine, serine, glutamine, glutamic acid, AMP, acetyl CoA (acCoA), ribose-5-phosphate (R5P), glyceraldehyde-3-phosphate (G3P), fructose-6-phosphate (F6P), phosphoglyceric acid (phAc), ATP, and citric acid.

Citric acid and isocitrate have the same fragmentation pattern except for the transition m/z 191.0 \rightarrow 73.0 which is characteristic for the isocitrate only. Unfortunately, they are not chromatographically separable.

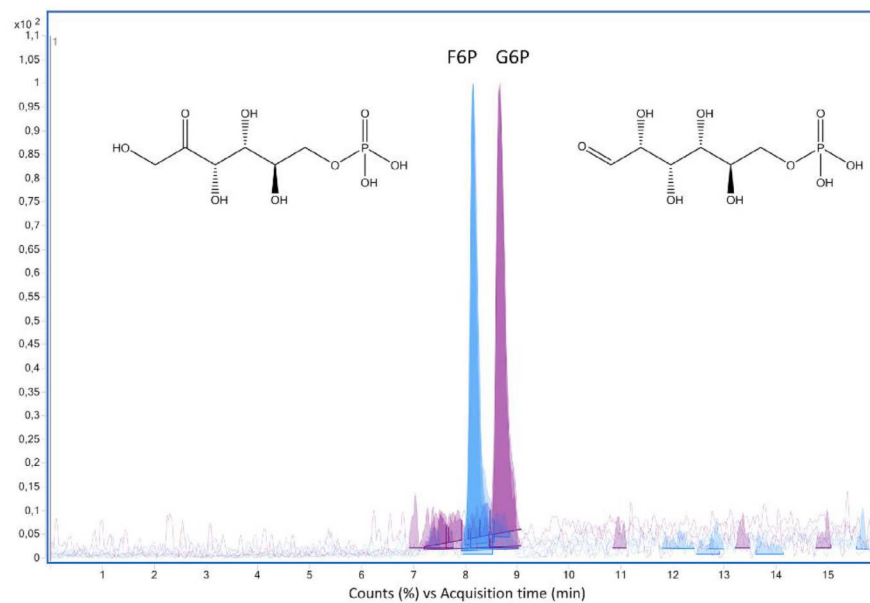


Figure 10. Chromatographic separation of fructose-6-phosphate (F6P) and glucose-6-phosphate (G6P)

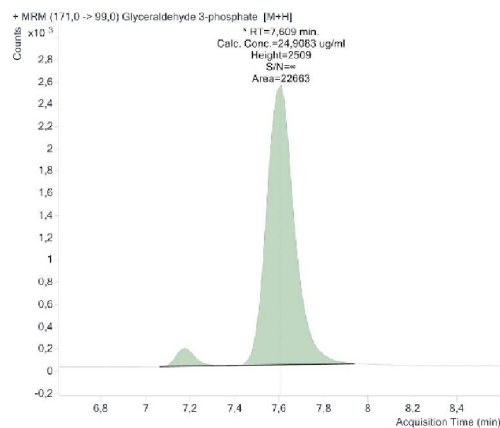


Figure 11. Chromatographic double peaks of glycerinaldehyde-3-phosphate

Glycerinaldehyde-3-phosphate presents two chromatographic peaks (Figure 11), probably due to the conversion to the enolic form as shown by the structures in Figure 12.

Glycerinaldehyde and dihydroxyacetone phosphate (DHAP) have the same molecular weight and fragmentation pattern (m/z 169 \rightarrow 79.1, m/z 169 \rightarrow 96.9) but they are chromatographically separated as shown in Figure 13.

Calibration curve

For the calibration curves, at least 8 concentration levels of calibration standards were used, including lower limit quality control (LLQC), lower limit of quantitation (LOQ), middle quality control (MQC), and high quality control (HQC). The Mandel test was performed to assess the better fitting, linear or quadratic, the analysis of the variances was conducted, and the values of LOD and LOQ were calculated with the intercept of the linear regression (LOD = $3.3 \times$ standard error intercept/slope; LOQ = $10 \times$ standard error intercept/slope). Table 4 summarizes the regression data, the LOD, and the LLOQ.

Matrix effect

In electrospray ionization, matrix effect is a confounding factor that may have a strong impact on the peak areas due to variations of ionization yield of the individual analyte.

The matrix effect was evaluated for all the target analytes in PBMCs at three different concentrations: high, medium, and different low concentrations. The analytes are endogenous compounds; therefore, their amounts were evaluated before (blank matrix) and after the spike (spiked matrix) at high,

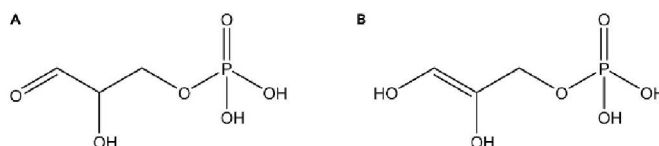


Figure 12. Chemical structures of glycerinaldehyde-3-phosphate and its possible isomer

(A) The (A) (left) shows the chemical structure of glycerinaldehyde-3-phosphate.

(B) The (B) (right) shows the chemical structure of the enolized form of glycerinaldehyde-3-phosphate.

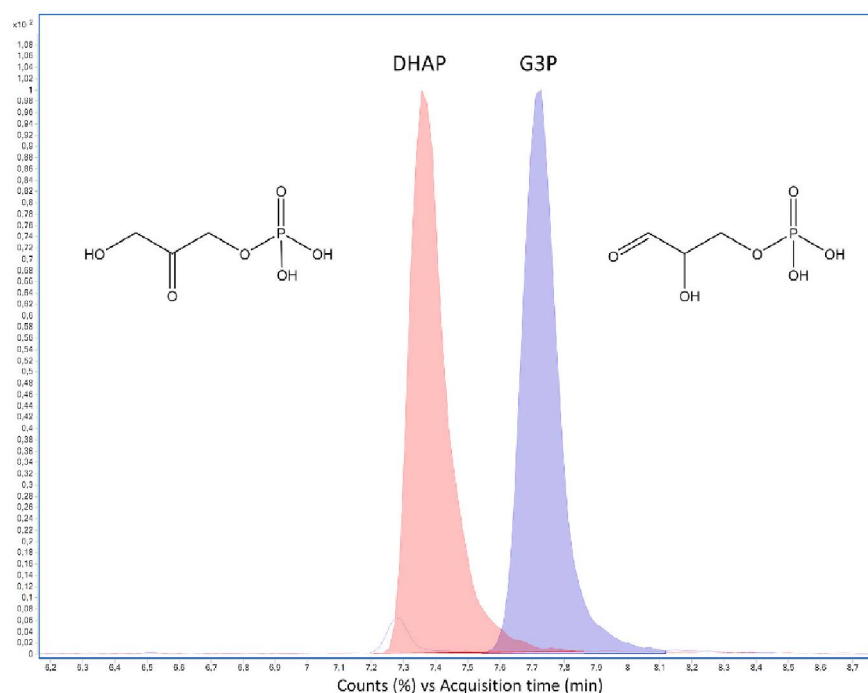


Figure 13. Chromatographic separation of DHAP and glyceraldehyde-3-phosphate (G3P)

medium, and low concentrations to calculate the matrix effect. The spiked double blanks are in H₂O:ACN (1:1).

$$\text{matrix effect (\%)} = \frac{\text{spiked matrix} - \text{blank matrix}}{\text{spiked double blank}} \times 100$$

Results are shown in Figure 14 for the unlabeled compounds and in Figure 15 for the labeled compounds.

Recovery

The recovery was evaluated for all the target analytes in PBMCs at three different concentrations: 10 µg/mL (HIGH), 5 µg/mL (MEDIUM), and different low concentrations (LOW): 0.01 µg/mL for acetyl CoA, ¹³C AMP, ATP; ¹³C glutamic acid, 0.05 µg/mL for ¹³C glutamine, ¹³C glycine, 0.1 µg/mL for glutamic acid and glutamine, 0.25 µg/mL for pyruvate and ¹³C pyruvate, 0.5 µg/mL for citric acid, fructose-6-phosphate, glyceraldehyde-3-phosphate, glycine, phosphoglyceric acid, 1 µg/mL for ribose-5-phosphate, serine, and lactate. The results obtained are shown in Figure 16 for the unlabeled compounds and in Figure 17 for the labeled compounds.

Accuracy and precision

Intra-day and inter-day precision and accuracy were evaluated for all compounds. Four concentrations (LLQC, LQC, MQC, HQC) were injected in quintuplicates three times on the same day (intra day) and on three different days (inter-day). The results were within ±15% for CV% (precision) and ±15% for RE% for all the concentration levels. Details are reported in Table 5.

Table 4. Summary of the regression data, the LOD, and the LLOQ of the targeted analytes

Substance	Calibration curve range ($\mu\text{g/mL}$)	Calibration curve	Weight	Coefficient of correlation	LOD ($\mu\text{g/mL}$)	LLOQ ($\mu\text{g/mL}$)
2,3- $^{13}\text{C}_2$ pyruvate	0.23–50	quadratic	1/x	0.9989	0.23	0.88
pyruvate	0.18–50	quadratic	1/x	0.9947	0.18	0.3
lactate	0.42–100	quadratic	1/x	0.9980	0.42	1.29
2- ^{13}C glycine	0.14–50	quadratic	1/x	0.9989	0.14	0.43
glycine	0.05–50	quadratic	1/x	0.9981	0.05	0.75
serine	0.34–50	quadratic	1/x	0.9982	0.34	0.45
1,2- $^{13}\text{C}_2$ glutamine	0.025–50	quadratic	1/x	0.9998	0.025	0.04
glutamine	0.11	quadratic	1/x	0.9994	0.11	0.2
1,2- $^{13}\text{C}_2$ glutamic acid	0.076–50	quadratic	1/x	0.9996	0.076	0.1
glutamic acid	0.22–50	quadratic	1/x	0.9995	0.22	0.5
1- ^{13}C AMP	0.04–50	quadratic	1/x	0.9993	0.04	0.05
AMP	0.028–50	quadratic	1/x	0.9986	0.028	0.045
acetyl CoA	0.07–50	linear	1/x	0.9984	0.07	0.085
ribose-5-phosphate	1–50	linear	1/x	0.9919	1	1.9
glyceraldehyde-3-phosphate	0.1–50	Linear	1/x	0.9995	0.1	1.2
fructose-6-phosphate	0.1–50	Linear	1/x	0.9939	0.1	0.2
phosphoglyceric acid	0.05–50	Linear	1/x	0.9978	0.05	0.08
ATP	0.025–50	Quadratic	1/x	0.9983	0.025	0.077
citric acid	0.1–20	Quadratic	1/x	0.9926	0.1	0.25

Carry-over

The analyzed compounds did not show carry-over.

Stability

The stability of the analytes was evaluated in triplicate and different conditions: at room temperature (0 h, 4 h, 8 h), at 4°C (0 h, 8 h, 24 h, 48 h, 168 h), and at –80°C (1 week, 4 weeks, 6 months, 1 year).

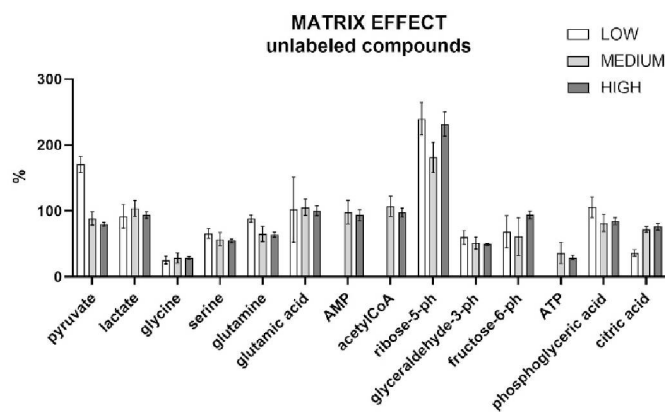


Figure 14. Matrix effect for the targeted unlabeled compounds

The standards were spiked at three different concentrations, high (10 $\mu\text{g/mL}$), medium (5 $\mu\text{g/mL}$), and low: 0.01 $\mu\text{g/mL}$ for acetyl CoA, ATP, 0.05 $\mu\text{g/mL}$ for AMP, 0.1 $\mu\text{g/mL}$ for glutamic acid and glutamine, 0.25 $\mu\text{g/mL}$ for pyruvate, 0.5 $\mu\text{g/mL}$ for citric acid, fructose-6-phosphate, glyceraldehyde-3-phosphate, glycine, phosphoglyceric acid, 1 $\mu\text{g/mL}$ for ribose-5-phosphate, serine, and lactate. All measurements were conducted in sextuplicate. Data are represented as mean \pm SD.

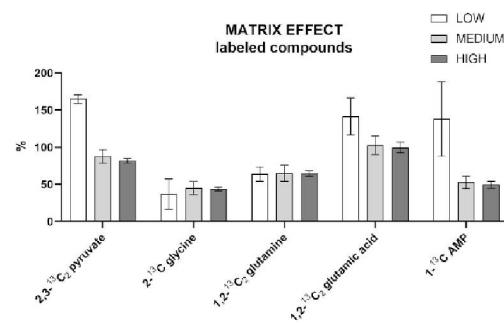


Figure 15. Matrix effect for the targeted labeled compounds

The standards were spiked at three different concentrations, high (10 $\mu\text{g/mL}$), medium (5 $\mu\text{g/mL}$), and low: 0.01 $\mu\text{g/mL}$ for 1-¹³C AMP, and 1,2-¹³C glutamic acid, 0.05 $\mu\text{g/mL}$ for 1,2-¹³C₂ glutamine, and 2-¹³C glycine, 0.25 $\mu\text{g/mL}$ 2,3-¹³C₂ pyruvate. All measurements were conducted in sextuplicate. Data are represented as mean \pm SD.

Moreover, the freeze-thaw stability was evaluated after three cycles. The obtained results are all within $\pm 15\%$.

LIMITATIONS

A limitation of this method is the number of cells that are necessary to obtain a sufficient concentration of compounds to analyze and quantify. Therefore, is not recommended to apply this protocol to experiment sets with a very limited number of cells.

The concentrations taken into consideration in this protocol are wide, and there is a high variability of concentrations in the cell extract. For instance, the concentrations of lactate are clearly in a different range in comparison with ATP or AMP.

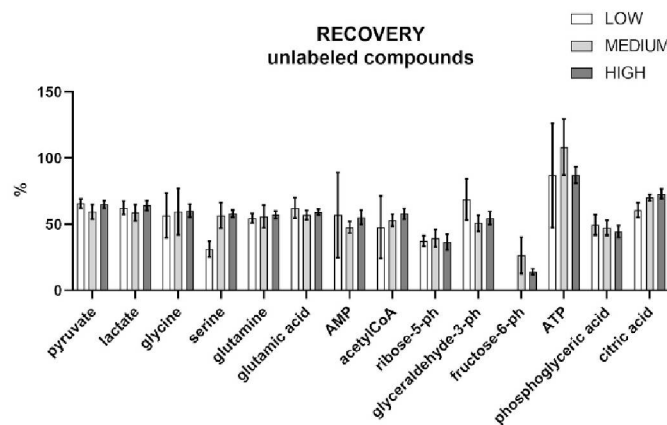


Figure 16. Recovery studies for the targeted unlabeled compounds

The standards were spiked at three different concentrations, high (10 $\mu\text{g/mL}$), medium (5 $\mu\text{g/mL}$), and low: 0.01 $\mu\text{g/mL}$ for acetyl CoA, ATP, 0.05 $\mu\text{g/mL}$ for AMP, 0.1 $\mu\text{g/mL}$ for glutamic acid and glutamine, 0.25 $\mu\text{g/mL}$ for pyruvate, 0.5 $\mu\text{g/mL}$ for citric acid, fructose-6-phosphate, glyceraldehyde-3-phosphate, glycine, phosphoglyceric acid, 1 $\mu\text{g/mL}$ for ribose-5-phosphate, serine, and lactate. All measurements were conducted in sextuplicate. Data are represented as mean \pm SD.

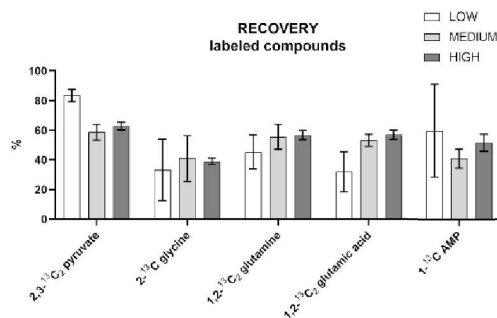


Figure 17. Recovery studies for the targeted labeled compounds

The standards were spiked at three different concentrations, high (10 $\mu\text{g}/\text{mL}$), medium (5 $\mu\text{g}/\text{mL}$), and low; 1-¹³C AMP; 1,2-¹³C₂ glutamic acid, 0.05 $\mu\text{g}/\text{mL}$ for 1,2-¹³C₂ glutamine, 2-¹³C glycine, 0.25 $\mu\text{g}/\text{mL}$ 2,3-¹³C₂ pyruvate. All measurements were conducted in sextuplicate. Data are represented as mean \pm SD.

This protocol describes an *in vitro* study; therefore, it is a model that might differ from the metabolism *in vivo*. This aspect must be taken into consideration while evaluating the data.

TROUBLESHOOTING

Problem 1

Precipitation in the mobile phases.

After some days, if the temperature of the laboratory is not highly controlled, the formation of precipitate in the mobile phases may be observed. As a result, the pressure of the system will show a general increase and some quick and temporary pressure drops as shown in Figure 18. After a while, these drops will become more frequent and longer.

Since there is not a pre-column capable to resist both pH, acidic for the passivation and basic for the analysis, the introduction of an in-line filter with a pore size of 0.2 μm or 0.3 μm is recommended to prevent the possible occlusion of the column due to precipitation in the mobile phases.

Potential solution

The best way to solve these pressure drops is to clean the system with pure water for 15–30 min and redo the passivation of the system afterwards.

Problem 2

Citric acid peak is difficult to integrate.

Potential solution

It is extremely important to use as much as possible steel-free capillaries, column fittings, and connectors. Another possible solution, not yet tested, is the use of a bioinert system.

Problem 3

Some cells, like monocytes, show some vulnerability during the incubation in a medium without glutamine and pyruvate and start to die already after 4–5 h.

Potential solution

Do not plan very long incubation of these vulnerable cells or optimize the incubation conditions in advance. Remember also that the incorporation of labeled glucose into the TCA cycle takes a longer time, and the use of labeled glutamine instead might be considered.



Table 5. Intra-day and inter-day precision and accuracy for the targeted compounds

Precision												
Substance	LLQC			LQC			MQC			HQC		
	Conc	Intra-day	Inter-day	Conc	Intra-day	Inter-day	Conc	Intra-day	Inter-day	Conc	Intra-day	Inter-day
	µg/mL	CV%	CV%	µg/mL	CV%	CV%	µg/mL	CV%	CV%	µg/mL	CV%	CV%
2,3- ¹³ C ₂ pyruvate	1	3.9	4.1	1.5	2.9	4.9	10	2.2	3.2	50	3.9	6.3
pyruvate	0.3	0.6	2.1	0.7	0.6	0.4	10	0.9	2	50	1.5	7
lactate	1.5	3.5	2.1	3	6.2	7.9	50	1.4	4.6	100	1.7	6.5
2- ¹³ C glycine	0.4	2.9	5.4	0.6	4.5	9.6	10	1.7	6.7	50	3.9	10.7
glycine	0.75	0.2	0.4	1.5	0.3	0.3	10	5.0	6.0	50	2.1	12.2
serine	0.45	0.4	0.2	2	1.0	0.8	10	1.5	4.2	50	1.5	6.8
1,2- ¹³ C ₂ glutamine	0.04	5.0	1.8	0.055	1.8	5.1	10	3.2	4.2	50	2.2	10.9
glutamine	0.2	2.1	2.4	0.3	1.7	3.5	10	2.9	3.3	50	3.0	11.3
1,2- ¹³ C ₂ glutamic acid	0.1	5.5	7.0	0.14	7.0	10.7	10	3.9	9.8	50	4.2	12.6
glutamic acid	0.5	3.5	1.7	1	2.5	2.5	10	3.5	7.0	50	4.1	14.2
1- ¹³ C AMP	0.05	14.9	14.5	0.18	3.2	4.4	10	3.5	5.1	50	6.1	10.2
AMP	0.045	6.9	12.7	0.065	3.0	3.3	10	3.6	11.9	50	4.4	9.6
acetyl CoA	0.085	4.5	10.6	0.45	2.6	1.1	10	3.2	6.1	50	5.8	10.2
ribose-5-phosphate	1.9	1.4	1.2	2.8	5.4	1.8	10	9.2	6.8	50	7.8	7.3
glyceraldehyde-3-phosphate	1.2	8.2	7.6	1.5	9.4	3.6	10	5.0	7.4	50	3.1	6.4
fructose-6-phosphate	0.2	1.8	1.1	0.7	3.4	0.5	10	8.4	8.5	50	5.5	6.3
phosphoglyceric acid	0.08	0.6	0.6	0.1	2.2	2.8	10	2.6	6.8	50	2.9	7.2
ATP	0.08	11	7.9	0.25	6.4	7.1	10	4.2	4.0	50	5.3	10.6
citric acid	0.25	0.3	0.6	0.8	0.3	0.3	10	4.5	3.7	50	2.6	1.6

Accuracy												
Substance	LLQC			LQC			MQC			HQC		
	Conc	Intra-day	Inter-day	Conc	Intra-day	Inter-day	Conc	Intra-day	Inter-day	Conc	Intra-day	Inter-day
	µg/mL	RE%	RE%	µg/mL	RE%	RE%	µg/mL	RE%	RE%	µg/mL	RE%	RE%
2,3- ¹³ C ₂ pyruvate	1	2.4	3.9	1.5	2.4	1.2	10	2.8	1.6	50	2.3	0.8
pyruvate	0.3	1.4	0.8	0.7	0.3	0.7	10	2.8	1.7	50	1.4	0.6
lactate	1.5	2.2	3.1	3.0	13.1	6.6	50	4.0	5.6	100	14.2	2.2
2- ¹³ C glycine	0.4	6.4	1.1	0.6	6.1	10.9	10	3.0	4.2	50	8.6	5.3
glycine	0.75	0.1	0.2	1.5	0.0	0.2	10	7.7	1.8	50	14.9	1.7
serine	0.45	0.2	0.1	2.0	1.5	1.1	10	2.6	2.6	50	1.4	1.4
1,2- ¹³ C ₂ glutamine	0.04	0.1	2.6	0.055	2.9	6.5	10	5.3	5.9	50	9.1	2.1
glutamine	0.2	3.1	1.1	0.3	2.4	4.1	10	5.2	5.5	50	7.6	0.2
1,2- ¹³ C ₂ glutamic acid	0.1	2.3	4.6	0.14	0.9	2.0	10	3.7	2.1	50	5.4	2.9
glutamic acid	0.5	0.6	0.2	1	2.8	1.2	10	1.3	9.5	50	2.8	1.2
1- ¹³ C AMP	0.05	-5	6.2	0.18	0.0	-0.1	10	1.0	4.4	50	-0.1	0.6
AMP	0.045	13.2	7.7	0.065	1.5	1.0	10	2.2	6.3	50	4.1	1.9
acetyl CoA	0.085	3.3	5.8	0.45	-0.2	1.0	10	1.7	-5.1	50	-3.2	-6.2
ribose-5-phosphate	1.9	1.6	1.1	2.8	8.4	1.1	10	0.1	9.4	50	15.6	17.6
glyceraldehyde-3-phosphate	1.2	1.7	9.1	1.5	0.1	2.2	10	11	1.2	50	0.8	1.6
fructose-6-phosphate	0.2	0.6	2.0	0.7	-0.7	0.1	10	0.1	-7.6	50	2.6	4.9
phosphoglyceric acid	0.08	0.2	0.1	0.1	5.7	4.9	10	7.3	3.9	50	0.5	-2.9
ATP	0.08	-1.2	0.7	0.25	-0.7	-0.7	10	2.5	-1.9	50	15	8.0
citric acid	0.25	0.2	0.6	0.8	0.5	0.6	10	8.4	3.7	50	-0.4	1.2

Problem 4

Some chromatographic peaks, like citric acid, might need manual integration to obtain the correct quantitation.

STAR Protocols Protocol

CellPress
OPEN ACCESS

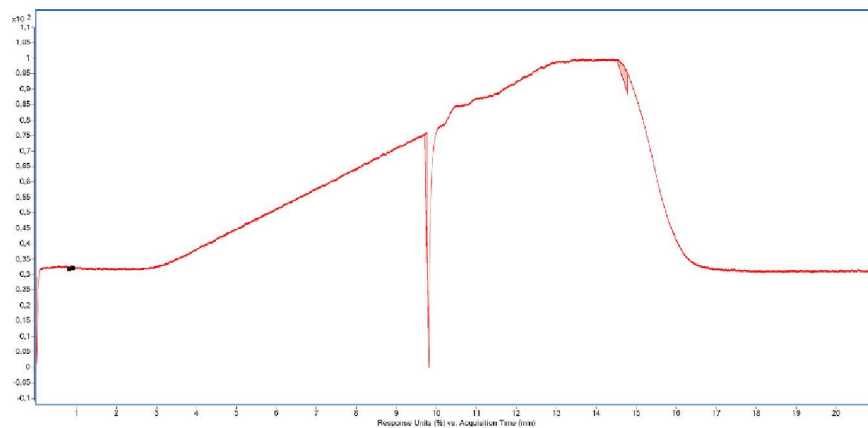


Figure 18. Troubleshooting due to the formation of precipitate in the mobile phases: The pressure line of the pump shows a sudden decrease

Potential solution

Carefully review every data and integrate manually, if necessary. Be consistent, in calibration curves and samples, to obtain a correct quantitation.

Problem 5

If PBMCs are obtained from blood donations, they might not be checked for infectious diseases.

Potential solution

Be sure to handle the samples with the right laboratory equipment: always wear gloves, lab coat, and goggles.

RESOURCE AVAILABILITY

Lead contact

Further information and requests for resources and reagents should be directed to and will be fulfilled by the lead contact, Maria K. Parr (maria.parr@fu-berlin.de).

Materials availability

This study did not generate new unique reagents.

Data and code availability

This study did not generate original code.

ACKNOWLEDGMENTS

Ginevra Giacomello received a scholarship from the NeuroMac School (DFG, the German Research Foundation – Project-ID 259373024 – CRC/TRR 167 (B05)) and was funded by the State of Berlin, Germany, with the Elsa-Neumann PhD scholarship. We would like to acknowledge the support by the OpenAccess Publication Fund of Freie Universität Berlin and the assistance of the Core Facility BioSupraMol supported by the DFG. We thank Bernhard Wüst, Agilent Technologies Inc., for his precious assistance in mass spectrometry and Adeline Dehlinger and Christian Böttcher for the sample collection of CSF and PBMCs and the introduction of G.G. to cell culture.

**STAR Protocols**
Protocol**AUTHOR CONTRIBUTIONS**

Conceptualization, G.G. and M.K.P.; methodology, G.G.; investigation, G.G.; formal analysis, G.G.; visualization, G.G.; resources, C.B. and M.K.P.; supervision, M.K.P.; writing – original draft, G.G.; writing – review & editing, C.B. and M.K.P.

DECLARATION OF INTERESTS

The authors declare no competing interests.

REFERENCES

- Agilent Technologies (2018). Usermanual additive infinitylab-5991-9516EN[Online]. <https://www.agilent.com/cs/library/usermanuals/public/usermanual-additive-infinitylab-5991-9516EN-agilent.pdf>.
- Buescher, J.M., Antoniewicz, M.R., Boros, L.G., Burgess, S.C., Brunengraber, H., Clish, C.B., DeBerardinis, R.J., Ferón, O., Frezza, C., Ghesquiere, B., et al. (2015). A roadmap for interpreting ^{13}C metabolite labeling patterns from cells. *Curr. Opin. Biotechnol.* **34**, 189–201.
- EMA. (2019). ICH guideline M10 on bioanalytical method validation. https://www.ema.europa.eu/en/documents/scientific-guideline/draft-ich-guideline-m10-bioanalytical-method-validation-step-2b_en.pdf.
- Hsiao, J.J., Potter, O.G., Chu, T.W., and Yin, H. (2018). Improved LC/MS methods for the analysis of metal-sensitive analytes using medronic acid as a mobile phase Additive. *Anal. Chem.* **90**, 9457–9464.
- Pesek, J.J., Matyska, M.T., and Fischer, S.M. (2011). Improvement of peak shape in aqueous normal phase analysis of anionic metabolites. *J. Sep. Sci.* **34**, 3509–3516.
- Quok, L.E., Liu, M., Joshi, S., and Turner, N. (2016). Fast exchange fluxes around the pyruvate node: a leaky cell model to explain the gain and loss of unlabeled and labeled metabolites in a tracer experiment. *Cancer Metab.* **4**, 13.
- Shlomi, T., Fan, J., Tang, B., Kruger, W.D., and Rabinowitz, J.D. (2014). Quantitation of cellular metabolic fluxes of methionine. *Anal. Chem.* **86**, 1583–1591.

3.2 Manuscript II: “Differential compartmentalisation of myeloid cell phenotypes and responses towards the CNS in Alzheimer’s disease”

Camila Fernández Zapata, Ginevra Giacomello, Eike J. Spruth, Jinte Middeldorp, Gerardina Gallaccio, Adeline Dehlinger, Claudia Dames, Julia K. H. Leman, Roland E. van Dijk, Andreas Meisel, Stephan Schlickeiser, Desiree Kunkel, Elly M. Hol, Friedemann Paul, Maria Kristina Parr, Josef Priller, and Chotima Böttcher

Nature Communications; 13 (2022) 7210

DOI: 10.1038/s41467-022-34719-2

Abstract: Myeloid cells are suggested as an important player in Alzheimer’s disease (AD). However, its continuum of phenotypic and functional changes across different body compartments and their use as a biomarker in AD remains elusive. Here, we perform multiple state-of-the-art analyses to phenotypically and metabolically characterise immune cells between peripheral blood (n=117), cerebrospinal fluid (CSF, n=117), choroid plexus (CP, n=13) and brain parenchyma (n=13). We find that CSF cells increase expression of markers involved in inflammation, phagocytosis, and metabolism. Changes in phenotype of myeloid cells from AD patients are more pronounced in CP and brain parenchyma and upon *in vitro* stimulation, suggesting that AD-myeloid cells are more vulnerable to environmental changes. Our findings underscore the importance of myeloid cells in AD and the detailed characterisation across body compartments may serve as a resource for future studies focusing on the assessment of these cells as biomarkers in AD.



Differential compartmentalization of myeloid cell phenotypes and responses towards the CNS in Alzheimer's disease

Received: 25 February 2022

Accepted: 1 November 2022

Published online: 23 November 2022

Check for updates

Camila Fernández Zapata^{1,2,3}, Ginevra Giacomello⁴, Eike J. Spruth^{3,5}, Jinte Middeldorp^{6,7}, Gerardina Gallaccio^{1,2,3}, Adeline Dehlinger^{1,2,3}, Claudia Dames⁸, Julia K. H. Leman^{3,9}, Roland E. van Dijk⁶, Andreas Meisel^{8,10}, Stephan Schlickeiser¹¹, Desiree Kunkel¹², Elly M. Hol⁶, Friedemann Paul^{1,2,8,10}, Maria Kristina Parr⁴, Josef Priller^{3,5,13,14,15} ✉ & Chotima Böttcher^{1,2,3,15} ✉

Myeloid cells are suggested as an important player in Alzheimer's disease (AD). However, its continuum of phenotypic and functional changes across different body compartments and their use as a biomarker in AD remains elusive. Here, we perform multiple state-of-the-art analyses to phenotypically and metabolically characterize immune cells between peripheral blood ($n=117$), cerebrospinal fluid (CSF, $n=117$), choroid plexus (CP, $n=13$) and brain parenchyma ($n=13$). We find that CSF cells increase expression of markers involved in inflammation, phagocytosis, and metabolism. Changes in phenotype of myeloid cells from AD patients are more pronounced in CP and brain parenchyma and upon *in vitro* stimulation, suggesting that AD-myeloid cells are more vulnerable to environmental changes. Our findings underscore the importance of myeloid cells in AD and the detailed characterization across body compartments may serve as a resource for future studies focusing on the assessment of these cells as biomarkers in AD.

Alzheimer's disease (AD) is the most common neurodegenerative disease that is recognized as one of the top devastating diseases worldwide, due to its high costs caused by patient care and management. The amyloid cascade hypothesis, a widely accepted hypothesis referring to AD pathogenesis, proposes amyloid plaques or the

β -amyloid (A β)-peptides as the direct cause of progressive neurodegeneration. A cascade initiated by A β deposition progressively leads to Tau pathology, synaptic dysfunction, neuronal loss and ultimately dementia¹. However, collective evidence obtained from patients with familial AD have questioned the linearity of the amyloid cascade in AD

¹Experimental and Clinical Research Center, a cooperation between the Max Delbrück Center for Molecular Medicine in the Helmholtz Association and Charité Universitätsmedizin Berlin, Berlin 13125, Germany. ²Max Delbrück Center for Molecular Medicine in the Helmholtz Association (MDC), Berlin 13125, Germany. ³Department of Neuropsychiatry and Laboratory of Molecular Psychiatry, Charité—Universitätsmedizin Berlin, corporate member of Freie Universität Berlin and Humboldt-Universität zu Berlin, Berlin 10117, Germany. ⁴Institute of Pharmacy, Freie Universität Berlin, Berlin 14195, Germany. ⁵DZNE, Berlin 10117, Germany. ⁶Department of Translational Neuroscience, University Medical Center Utrecht Brain Center, Utrecht University, 3584 CX Utrecht, The Netherlands. ⁷Department of Neurobiology and Aging, Biomedical Primate Research Centre, 2288 GJ Rijswijk, The Netherlands. ⁸Department of Neurology and Experimental Neurology, Charité-Universitätsmedizin Berlin, Berlin 10117, Germany. ⁹Institute of Biology, Humboldt-Universität zu Berlin, Berlin 10115, Germany. ¹⁰NeuroCure Clinical Research Center, Charité-Universitätsmedizin Berlin, Berlin 10117, Germany. ¹¹Institute of Medical Immunology, BIH Center for Regenerative Therapies (BCRT), Berlin Institute of Health at Charité - Universitätsmedizin Berlin, Berlin 13353, Germany. ¹²Flow & Mass Cytometry Core Facility, Berlin Institute of Health at Charité - Universitätsmedizin Berlin, Berlin 13353, Germany. ¹³Department of Psychiatry and Psychotherapy, School of Medicine, Technical University Munich, Munich 81675, Germany. ¹⁴UK DRI, University of Edinburgh, Edinburgh EH16 4SB, UK. ¹⁵These authors jointly supervised this work: Josef Priller, Chotima Böttcher. ✉ e-mail: josef.priller@charite.de; chotima.boettcher@charite.de

Article

<https://doi.org/10.1038/s41467-022-34719-2>

pathology, particularly regarding the gradual evolution of the disease in humans^{2,4}. In addition, it is imperative to accommodate the complex compensation mechanisms of multiple cell types in a hypothesis. The empirical observations of (i) microglial activation in the brain^{5,8}, (ii) increased production of inflammatory mediators in the brain, peripheral blood and cerebrospinal fluid (CSF), which are related to the blood-CSF barrier (BCSFB) disruption^{7,9} and (iii) differential myeloid and lymphoid cell responses in the peripheral blood and CSF^{10,11} leads to a hotly debated theory of the two poles of AD, (immune-driven) neuroinflammation and neurodegeneration. According to this theory, neurodegeneration could be promoted by microglia/macrophages that respond to an increased inflammatory environment in the pathological brain^{12–14}, or vice versa neuroinflammation could be initiated by the local neurodegeneration in the brain. Results obtained from studies in mouse models of AD suggest that multiple myeloid cell populations in different body compartments significantly modify the disease outcome via different mechanisms. For example, microglia play a dichotomous role which alternates between protective clearance of β -amyloid and debris, and detrimental neurotoxic effects^{14,15}. The CNS-associated macrophages (CAMs) are key immune cells involved in the regulation of cerebral amyloid angiopathy (CAA) and thus modify the disease burden in AD^{16–18}, whereas the hematogenous myeloid cells^{16,19} do not seem to significantly modify the disease outcome in mouse models of AD. However, studies in humans showed that the CD33 AD-risk allele is linked to higher expression of CD33 on monocytes, and an expression quantitative trait locus (eQTL) study in patients with autoimmune or neurodegenerative diseases revealed that the AD susceptibility alleles are significant eQTLs only in monocytes, suggesting an involvement of this cell type in human AD pathology^{20,21}. Unlike studies in mouse models, technical limitations of studies using human specimens, especially the difficulties in procuring human specimens from different body compartments, have confined the understanding of the continuum of myeloid cell diversity to functional changes towards the CNS and/or AD pathology. Using mass cytometry, we could demonstrate the phenotypic differences between human immune cells in the CSF and those in the peripheral blood, and the unique phenotypic signatures of human microglia, in comparison to the circulating immune cells²². Whether these phenotypic and functional diversities in different body compartments are more pronounced in neurological disorders or associated with any soluble mediators (i.e. biomarker) remain to be investigated.

In this study, we employed a combination of multiple state-of-the-art technologies such as high-dimensional mass cytometry (CyTOF), Seahorse, Luminex and tandem mass spectrometry to comprehensively characterize immune cells (with a particular emphasis on myeloid cells) in different body compartments including the peripheral blood, CSF, brain parenchyma (frontal cortex) and choroid plexus (CP). Specifically, we compared the cellular composition, phenotypes and metabolic responses of myeloid cells from AD patients with control individuals and patients with other neurodegenerative or neuropsychiatric disorders. Our findings showed differences in marker expression and phenotypes of myeloid cells between body compartments, associated with an activation of the immune response including changes in cytokine/chemokine expression and cell metabolism, as well as responses to acute inflammation. In line with the previously published studies^{23,24}, we did not detect gross phenotypic difference between diseases within each compartment but the disease-associated phenotypic differences became more pronounced after *in vitro* environment and stimulation. Some of these differences were found enhanced in AD patients. Results obtained from our studies demonstrate different compositions of myeloid cells between different compartments, and suggest that responses of this cell population in AD might be related to the more compartmentalized inflammation in and/or towards the CNS. Creating such a bird's-eye view of phenotypic and functional changes of myeloid cells and other immune cells in

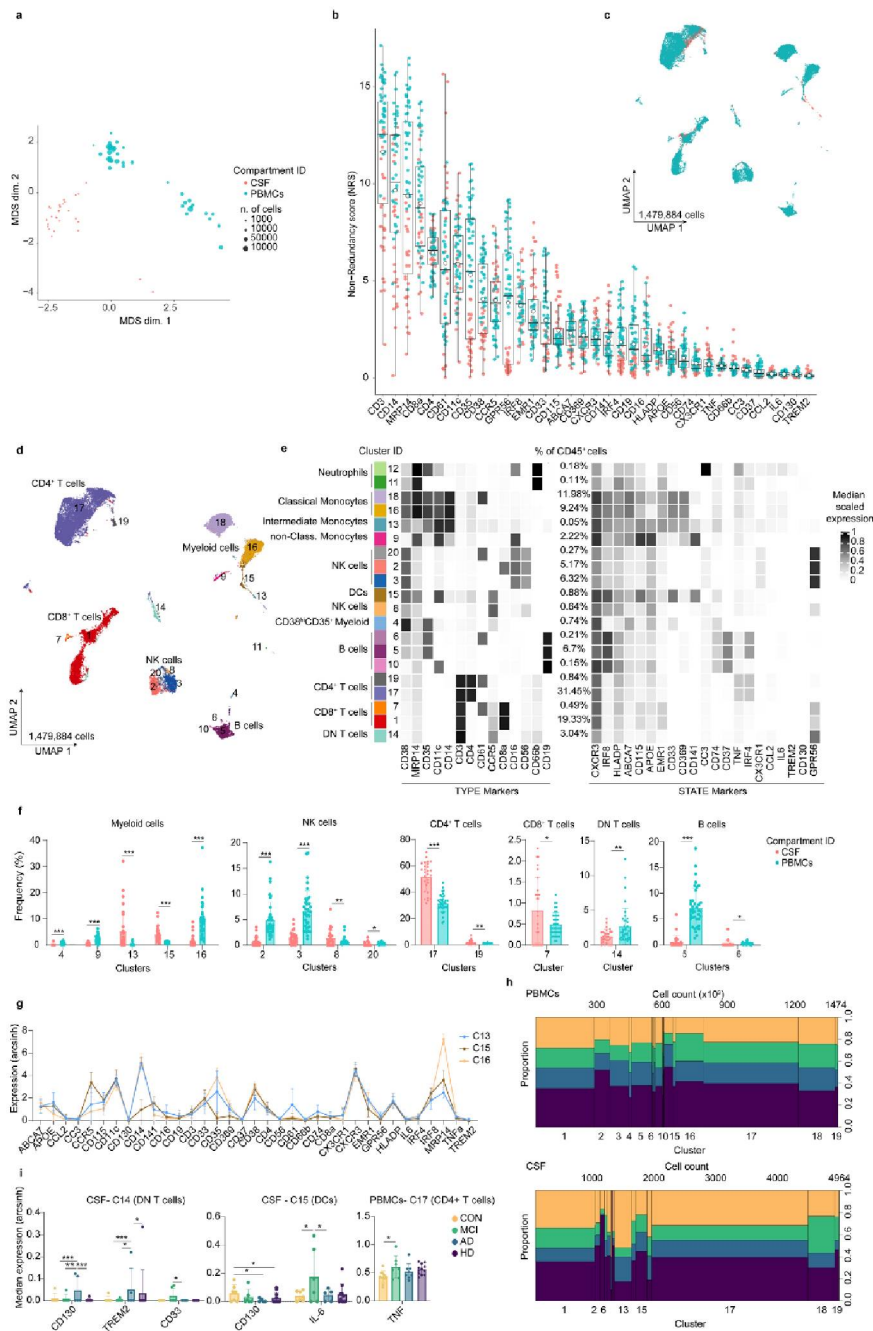
different compartments will aid better understanding of the pathophysiology of AD at the systems-level, and potentially help improve the diagnosis and treatment of the disease.

Results

Differential phenotypes between peripheral blood and CSF myeloid cells

CSF and peripheral blood samples allow a more precise diagnosis as well as follow-up analyses on the same patients to monitor disease progression and/or treatment efficacy. Therefore, general knowledge of immune cell heterogeneity as well as inflammatory mediators detected in these two compartments is important for evaluating disease-associated alterations. To compare the different phenotypes of circulating immune cells in the CSF and peripheral blood, we simultaneously profiled peripheral blood mononuclear cells (PBMCs) and immune cells from the CSF that were isolated from the same donors with no neurological disorders (referred to as a control group, CON) and from patients with neurodegenerative disorders (i.e. AD, mild cognitive impairment (MCI) and Huntington's disease (HD)) (Supplementary Table 1). The immune phenotypes were characterized using our previously validated CyTOF workflow with some optimization (see Methods for more details)²². Briefly, the samples were first stained with an antibody panel (35 antibodies, *Panel 1*; Supplementary Table 2), which was designed to encompass the major circulating immune cell subsets (i.e. T & B cells, myeloid cells (i.e. monocytes, macrophages and dendritic cells), natural killer (NK) cells), activity-related markers, chemokine receptors and cell subset markers. After CyTOF acquisition, the data were pre-processed as previously described, including the steps of de-barcoding, compensation, and quality control (Supplementary Fig. 1a)^{22,25,27}. The multi-dimensional scaling (MDS) plot²⁵ showed overall differential marker expression between CSF cells and PBMCs (Fig. 1a). This phenotypic variance may mainly be explained by differential expression of CD3, CD14, MRP14, CD8a, CD4, CD61, CD11c, CD35, CD38 and CCR5 as shown by the MDS-based non-redundancy score (NRS)²⁵ of each sample (Fig. 1b). Differences in cell compositions between CSF and blood can be illustrated in the UMAP plot (Fig. 1c). To further evaluate the phenotypic differences of immune cells between the two compartments, we performed the clustering analysis using the *FlowSOM*²⁶ and *ConsensusClusterPlus*²⁷ algorithms. To achieve a robust phenotypic differentiation between the single cells, we selected lineage markers and the top ten highest NRS markers (Fig. 1b) as input (i.e. embedding markers) for the clustering analysis. These markers (here referred to as "TYPE" markers) mainly determined phenotypic differences between the cell clusters. The rest of the markers were left as "STATE" markers, which were then used to analyze differential marker expression of each cluster between conditions.

A total of twenty clusters were identified (Fig. 1d, e and Supplementary Fig. 1b, c). Comparing the peripheral blood with the CSF compartment, we detected fifteen differentially abundant clusters between the two compartments, including myeloid cells (Clusters 4, 9, 13, 15 and 16) and NK cells (Clusters 2, 3, 8 and 20) as well as T cells (Clusters 7, 14, 17 and 19) and B cells (Cluster 5 and 6) (Fig. 1f). The CSF-enriched clusters were mainly identified as myeloid cells (Clusters 13 and 15). In addition, the proportion of CD8⁺ and CD4⁺ T cells in the CSF was also found higher than in the peripheral blood (Clusters 7, 17 and 19) (Fig. 1f and Source Data). Compared to classical monocytes (Cluster 16), CSF-enriched myeloid cells (Cluster 13 and 15) showed different expression of markers involved in inflammatory responses, phagocytosis and metabolism such as increased CD16, CCR5, CXCR3, CD115, CD74, GPR56, C3, ApoE and CD61 expression, whereas CD38, IL-6, TNF, CD35, CD369 (Clec7A), CD14, EMR1 and MRP14 were detected at a lower level (Fig. 1g; Supplementary Fig. 1d and Source Data). However, we detected no differences in myeloid cell heterogeneity, when comparing myeloid cells in CSF or peripheral blood between conditions



(i.e. CON, MCI, AD and HD) (Fig. 1h). Small phenotypic differences in CSF myeloid cells (Cluster 15) were detected between conditions (Fig. 1i). In addition, we also observed increased expression of TNF in blood CD4⁺ cells (Cluster 17) of patients with MCI, AD and HD, as well as increased CD130, TREM2 and CD33 expression in CSF double-negative (DN) T cells (Cluster 14) of AD and MCI patients (Fig. 1i).

Increased proportion of P2Y₁₂-expressing myeloid cells within the CSF compartment
 Recently, the studies^{30,31} using single-cell RNA sequencing (scRNA-Seq) reported a rare population of myeloid cells in the CSF with a transcriptomic signature matching microglia. These microglia-like cells were proposed to be found only in the CSF of subjects with

Article

<https://doi.org/10.1038/s41467-022-34719-2>

Fig. 1 | Deep immune profiling of human mononuclear cells from blood (PBMCs) and cerebrospinal fluid (CSF)—Panel 1. Results were from 38 biologically independent PBMCs (control (CON), $n = 11$; Alzheimer's disease (AD), $n = 8$; Mild cognitive Impairment (MCI), $n = 7$ and Huntington's disease (HD), $n = 12$) and 28 biologically independent CSF samples (CON, $n = 7$; AD, $n = 5$; MCI, $n = 6$ and HD, $n = 10$). **a** MDS plot for PBMC (green dots) and CSF (pink dots) samples. **b** The plot shows NRS for each marker. Each dot represents the per-sample NR scores. Boxes extend from the 25th to 75th percentiles. Whisker plots show the min (smallest) and max (largest) values. The line in the box denotes the median. The empty black circles are mean NR scores. **c** UMAP projections of CD45⁺ cells from PBMCs and CSF samples, coloured by compartment ID. Each dot represents one cell. **d** UMAP projection, colouring indicates 1–20 clusters. **e** Heatmap cluster depicting the median expression levels of TYPE and STATE markers. Heat colours of expression levels have been scaled for each marker individually (to the 1st and 5th quintiles)

(black, high expression; white, no expression). **f** Frequency plots of the fifteen differentially abundant clusters (mean \pm SD). An FDR-adjusted p -value < 0.05 was considered statistically significant, determined using the EdgeR test for differential cluster abundance included in the *diffcyt* package for R ($*p < 0.05$; $**p < 0.01$; $***p < 0.001$, adjusted). Each dot represents the value of each sample. Data displayed as mean \pm SD. **g** Line graph of the arcsinh marker expression (mean \pm SD) between CSF-enriched myeloid cell clusters (C13 and C15) and the classical monocytes (C16) (FDR-adjusted Mann–Whitney U -test, two-sided, adjusted, two-sided). **h** Mosaic plots depicting cluster proportion and cell count per cluster. **i** Median expression (with arcsinh transformation) of markers found differentially expressed between conditions using LMM (linear mixed-models) included in the *diffcyt* package for R; $*p < 0.05$; $**p < 0.01$; $***p < 0.001$, adjusted. Data displayed as mean \pm SD. Raw data (for **f**, **g** and **i**) are provided as Source Data.

neuroinflammation. However, due to the limited number of cases and the lack of proper controls, conclusions about this neuroinflammation-restricted microglia-like cells in the CSF cannot readily be drawn from these datasets. To prove the existence of this rare cell population, we performed another CyTOF measurement of CSF cells and PBMCs from the same individuals (as in Fig. 1) using an antibody panel including microglia markers such as the P2Y₁₂ receptor and markers involved in cell activation (Panel 2, 35 antibodies, Supplementary Table 3). Similar to results obtained from the antibody Panel 1 (Fig. 1), CSF cells and PBMCs were phenotypically different, as shown in the UMAP illustration (Fig. 2a) and MDS plot (Supplementary Fig. 2a). The clustering analysis using lineage markers and the top ten NRS markers (Supplementary Fig. 2b) including P2Y₁₂ as embedding parameters revealed twenty clusters (Fig. 2b, c and Supplementary Fig. 2c, d). With this antibody Panel 2, we detected thirteen differentially abundant clusters between the two compartments, including myeloid (Clusters 4, 8, 13, 16, 17, 18 and 20), lymphoid (Clusters 1, 2, 3, 11 and 14) and NK (Cluster 5) cell subsets (Fig. 2d and Source Data). In line with the previous studies with scRNA-Seq^{30,31}, we detected a strong difference in the abundance of CCR2^{low}P2Y₁₂⁺ (Cluster 16) and CCR2⁺P2Y₁₂^{lo} (Cluster 20) myeloid cell subsets, which were enriched in the CSF (Fig. 2d, e). However, these myeloid cell subsets were not restricted to the CSF as has been previously proposed^{30,31}. CCR2^{int}P2Y₁₂⁺ myeloid cells could be found also in the peripheral blood at a lower proportion (Cluster 16; mean \pm sd: CSF, 4.95 \pm 6.08, PBMCs, 0.40 \pm 0.38). Our findings suggest that these cells should be cautiously termed “neuroinflammation-associated microglia-like cells”, as these cells were also present in the CSF of healthy donors. When compared to the CD16⁺CCR2^{int} classical blood monocytes (cluster 15), this CSF-enriched CCR2^{low}P2Y₁₂⁺ cluster (Cluster 16) showed differences in marker expression including higher level of CD91, CD11c, HLA-DR, CD16, CD68, MS4A4A, and AXL but lower level of OPN, CCR2, CD163 and CD64 (Fig. 2f and Source Data). However, when compared with CD16⁺CCR2^{int} non classical (cluster 13) P2Y₁₂^{low} blood monocytes, cluster 16 show higher expression of most of the markers including HLA-DR, CD16, CCR2, CD11b, CD169, CD64, CD91, CD68 and MIP-1 β (Fig. 2f and Source Data). We also observed differential marker expression between the two P2Y₁₂^{low} CSF-enriched myeloid cell subsets (Cluster 16 and 20; Fig. 2g and Source Data), suggesting two different myeloid cell subsets/states.

Similar to the results obtained from Panel 1, we did not detect any major changes in cell composition between diseases and also between CON and disease CSF cells (Fig. 2h). However, some differential marker expressions (mainly within the myeloid cell subsets) could be found between CON and HD PBMCs (Fig. 2i). Of note, although it was not significantly different, similar changes in phenotypes were found in PBMCs from AD and MCI, when compared to CON PBMCs (Fig. 2i).

Changes in glucose metabolism of CSF-treated myeloid cells

Differences in metabolic profiles can link to functional changes of myeloid cells³². We next evaluated changes in cellular bioenergetics of

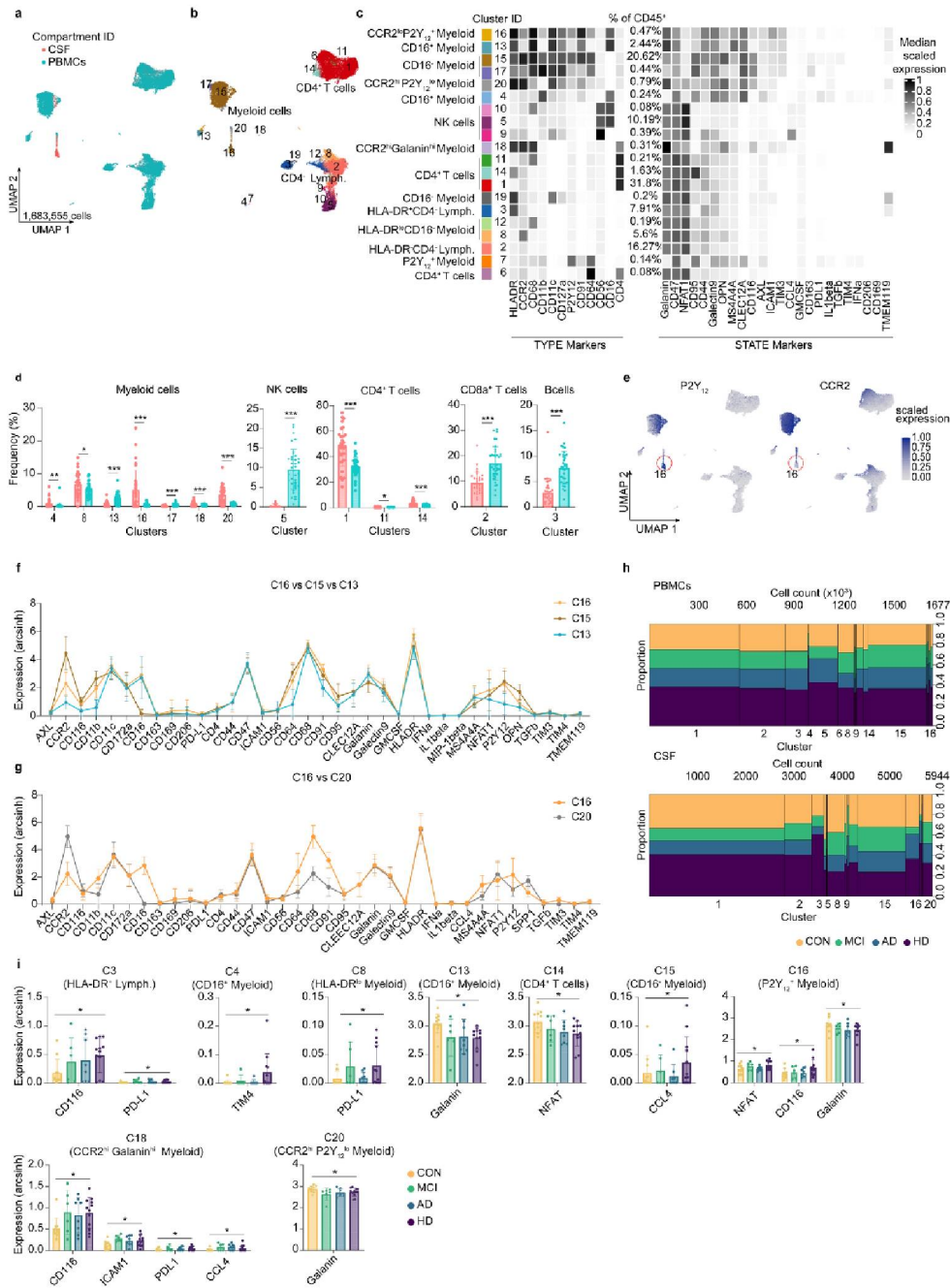
myeloid cells after exposure to CSF. Myeloid cells from a healthy individual were isolated from PBMCs using magnetic activated cell sorting (MACS), and subsequently treated with CSF of CON individuals or of patients with AD or MCI. Bioenergetics was measured by Seahorse. Shortly after exposure to CSF, myeloid cells increased the extracellular acidification rates (ECARs), whereas plasma-treated cells showed comparable ECARs between conditions including the PBS-treated cells. The oxygen consumption rate (OCR) was slowly changed after treatment with CSF (Fig. 3a). Interestingly, myeloid cells treated with CSF of patients with AD showed slightly but significantly higher ECARs when compared with cells treated with PBS or CSF from CON individuals. ECARs were comparable between the treatment with AD-CSF and MCI-CSF. The OCR was found comparable between disease conditions. When the cells were treated with plasma, no significant differences were observed between the groups. These results demonstrate changes in metabolism (possibly in glycolysis) of myeloid cells after exposure to the CSF environment, which was enhanced in AD. Next, to precisely evaluate the alteration of glucose metabolism, we cultured pre-sorted monocytes (from the same healthy individual as in the Seahorse experiment) in the presence of 1,2-¹³C₂ glucose and CSF from CON or AD patients, with or without LPS. ¹³C₂ glucose-derived metabolites were then quantified using HPLC-MS/MS (Fig. 3b). Similar to the findings mentioned above, we observed significantly increased glycolysis in monocytes treated with AD-CSF, determined by an increase of ¹³C₂-pyruvate production (Fig. 3c, d). However, the conversion of ¹³C₂-pyruvate to ¹³C-lactate was significantly decreased in AD-CSF-treated monocytes, whereas no differences were found in CON-CSF in comparison to untreated monocytes (Fig. 3c, e). Furthermore, we also detected decreased conversion of ¹³C₂-glucose to ¹³C₂-serine in AD-CSF-treated monocytes (Fig. 3c, f). These findings suggested an increased glycolysis in myeloid cells after exposure to CSF (compared with no CSF treatments), possibly resulting in an increased level of metabolites downstream of pyruvate metabolism.

Changes in phenotypes and immune responses of myeloid cells after exposure to cerebrospinal fluid

Next, we investigated whether these metabolic changes relate to CSF-enhanced activation phenotypes of myeloid cells. A comparative measurement of pro- and anti-inflammatory mediators in the plasma and CSF from patients with AD, compared with healthy control and patients with other neurological disorders such as MCI, HD, as well as frontotemporal lobar degeneration (FTLD), depression and schizophrenia (SCZ). The Luminex assay targeted 12 proteins including IL-8, IL-6, IL-10, CCL2, TNF, as well as IP-10 (CXCL10) and Macrophage Inflammatory Protein (MIP)- α and - β , the chemokine receptor ligands of CXCR3 and CCR5 respectively. Of note, both CXCR3 and CCR5 were found up-regulated in the CSF myeloid cells (as shown in Fig. 1). The Luminex assay revealed a higher concentration of IL-8, MIP- α , MIP- β , CCL2 (MCP-1), IL-6 and IP-10 in the CSF, whereas the level of the TNF and Rantes (CCL5) were higher in plasma (Fig. 4a).

Article

<https://doi.org/10.1038/s41467-022-34719-2>



Interestingly, a potent chemotactic factor for myeloid cells, IL-8 (or CXCL8) and a CCR5-ligand MIP- α were both detected at a higher level in AD-CSF, compared to the CON- and HD-CSF, which is well correlated with the finding described above (i.e. Fig. 1) of an increased CCR5 expression on CSF-enriched myeloid cells. A previous study has demonstrated that, after exposure to plasma from patients with AD,

the human monocytic cell line THP-1 increased glycolysis and the expression of inflammatory molecules such as IL-8 and TNF³⁵. Of note, IL-8 level in AD-CSF was also slightly higher than that in MCI-CSF, whereas MIP- α levels were comparable between AD- and MCI-CSF (Fig. 4b). The plasma concentration of all mediators was not significantly different between the conditions. Increased IL-8 level in

Article

<https://doi.org/10.1038/s41467-022-34719-2>

Fig. 2 | Deep immune profiling of human mononuclear cells from blood (PBMCs) and CSF – Panel 2. Results shown in a–i were obtained from 38 biologically independent PBMCs (CON, *n* = 11; AD, *n* = 8; MCI, *n* = 7 and HD, *n* = 12) and 28 biologically independent CSF samples (CON, *n* = 7; AD, *n* = 5; MCI, *n* = 6 and HD, *n* = 10). **a** Two-dimensional projections of single-cell data generated by UMAP of PBMCs (green dots) and CSF (pink dots) cells. Each dot represents one cell. **b** UMAP plot of all samples. The colouring indicates 20 clusters representing diverse immune cell phenotypes, defined by the *FlowSOM* algorithm. **c** Phenotypic heatmap of cluster identities depicting the expression levels of 12 TYPE markers used for the cluster analysis and 24 STATE markers. Heat colours of expression levels have been scaled for each marker individually (to the 1st and 5th quintiles) (black, high expression; white, no expression). **d** Frequency plots of the thirteen differentially abundant clusters between the CSF and blood compartments. Data

displayed as mean ± SD. An FDR-adjusted *p*-value < 0.05 was considered statistically significant, determined using the edgeR test for differential cluster abundance (**p* < 0.05; ***p* < 0.01; ****p* < 0.001, adjusted). Each dot represents the value of each sample. **e** Overlay UMAP plots of all samples showing scaled expression of P2Y₁₂ receptor and CCR2. **f, g** Line graph of the arcsinh marker expression (mean ± SD) between CSF-enriched myeloid cell cluster (C16) and the classical monocytes (C15) (**f**) and CCR2^{hi}P2Y₁₂^{lo} (Cluster 20) (**g**) (FDR-adjusted Mann-Whitney *U*-test, two-sided, adjusted, two-sided). **h** Mosaic plots depicting cluster proportion and cell count per cluster for PBMC and CSF cells. **i** Median expression (with arcsinh transformation) of markers found differentially expressed between conditions (CON, MCI, AD and HD) using LMM (linear mixed-models) included in the diffcyt package for R; **p* < 0.05; ***p* < 0.01; ****p* < 0.001, adjusted. Data displayed as mean ± SD. Source data (for **d, f, g** and **i**) are provided as a Source Data file.

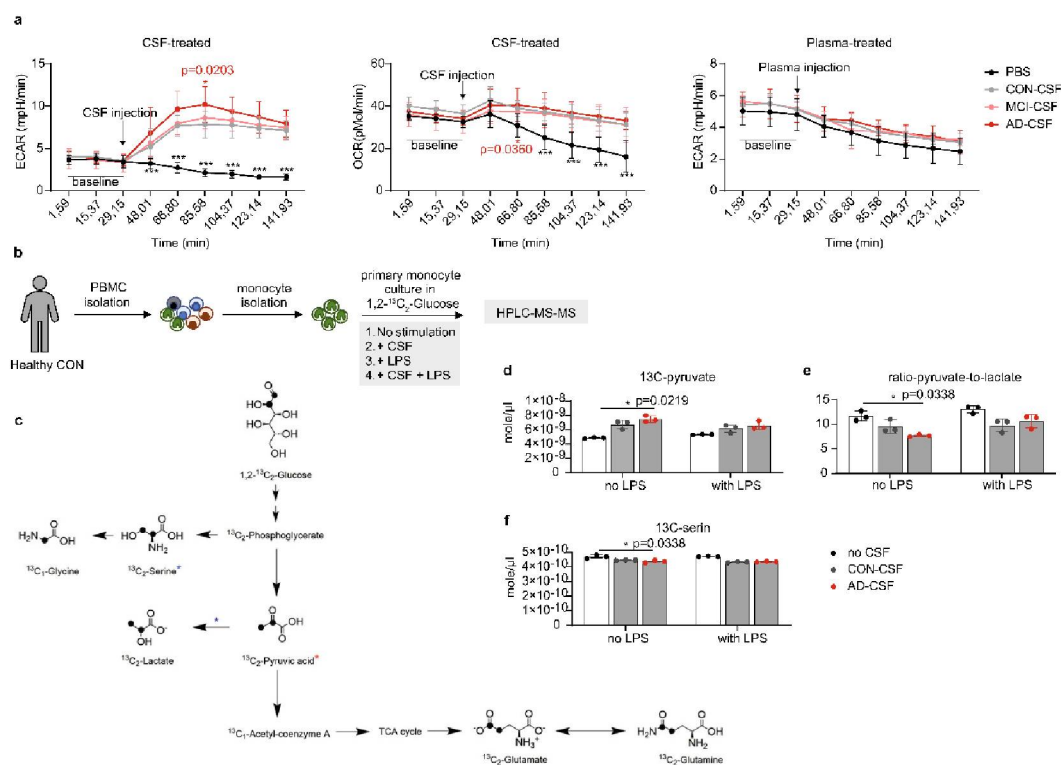


Fig. 3 | Alterations in glucose metabolism after exposure to CSF. **a** Seahorse analysis of extracellular acidification rate (ECAR, right and left plot) and oxygen consumption rate (OCR, middle plot) in monocytes treated with either PBS, CSF or plasma from CON (*n* = 5, biological replication), MCI (*n* = 5, biological replication) or AD (*n* = 5, biological replication). Data displayed as mean ± SD. Two-way ANOVA with Tukey's multiple comparisons; **p* < 0.05, ***p* < 0.01, ****p* < 0.001 and *****p* < 0.0001. The results are from three different experiments. **b** Schematic representation of sample processing, ex vivo experiment and measurement. Reference PBMCs from a healthy donor were isolated, monocytes were pre-sorted using the magnetic activated cell separation (MACS). Cells were then cultured in the

presence of 1,2-¹³C₂-glucose and treated with different conditions. Cells were then harvested and analyzed with HPLC-MS-MS. **(c–f)** The 1,2-¹³C₂-glucose metabolism **(c)** showing metabolites obtained from monocytes treated either with PBS or CSF from CON (*n* = 3, biological replication) or AD (*n* = 3, biological replication) that were quantified using HPLC-MS-MS. Red asterisk indicates significantly increased metabolite, whereas the blue asterisk labels significantly decreased metabolites. The bar graphs show concentration of 1,2-¹³C₂-glucose-derived ¹³C-pyruvate **(d)**, the ¹³C-pyruvate-to-¹³C-lactate conversion **(e)** or ¹³C₂-glucose-derived ¹³C-serine **(f)**. Data displayed as mean ± SD. Kruskal–Wallis test, **p* < 0.05 and ****p* < 0.01. Source data (for **a, d, e** and **f**) are provided as a Source Data file.

AD-CSF was positively correlated with IL-6 and MIP-α (Fig. 4c), suggesting that the CSF-conditions potentially facilitated changes in myeloid cell phenotypes towards the CNS. Of note, the level of the cytokine expression did not correlate with the age in patients with AD and MCI (Fig. 4d). We detected gender-related differences in the CSF IL-8 level in CON (higher level in males) and MCI (higher level in females) samples (Supplementary Fig. 3a). The level of CSF MIP-1α

was comparable between genders in all conditions (Supplementary Fig. 3b).

To determine the impact of IL-8 or MIP-1α on phenotypic changes of blood immune cells, PBMCs isolated from CON donors and patients with AD and MCI were cultured in the presence of either paired CSF (from the same individual) or IL-8 or MIP-α, using our previously validated protocol³⁴. PBS-treated culture served as a control for the

Article

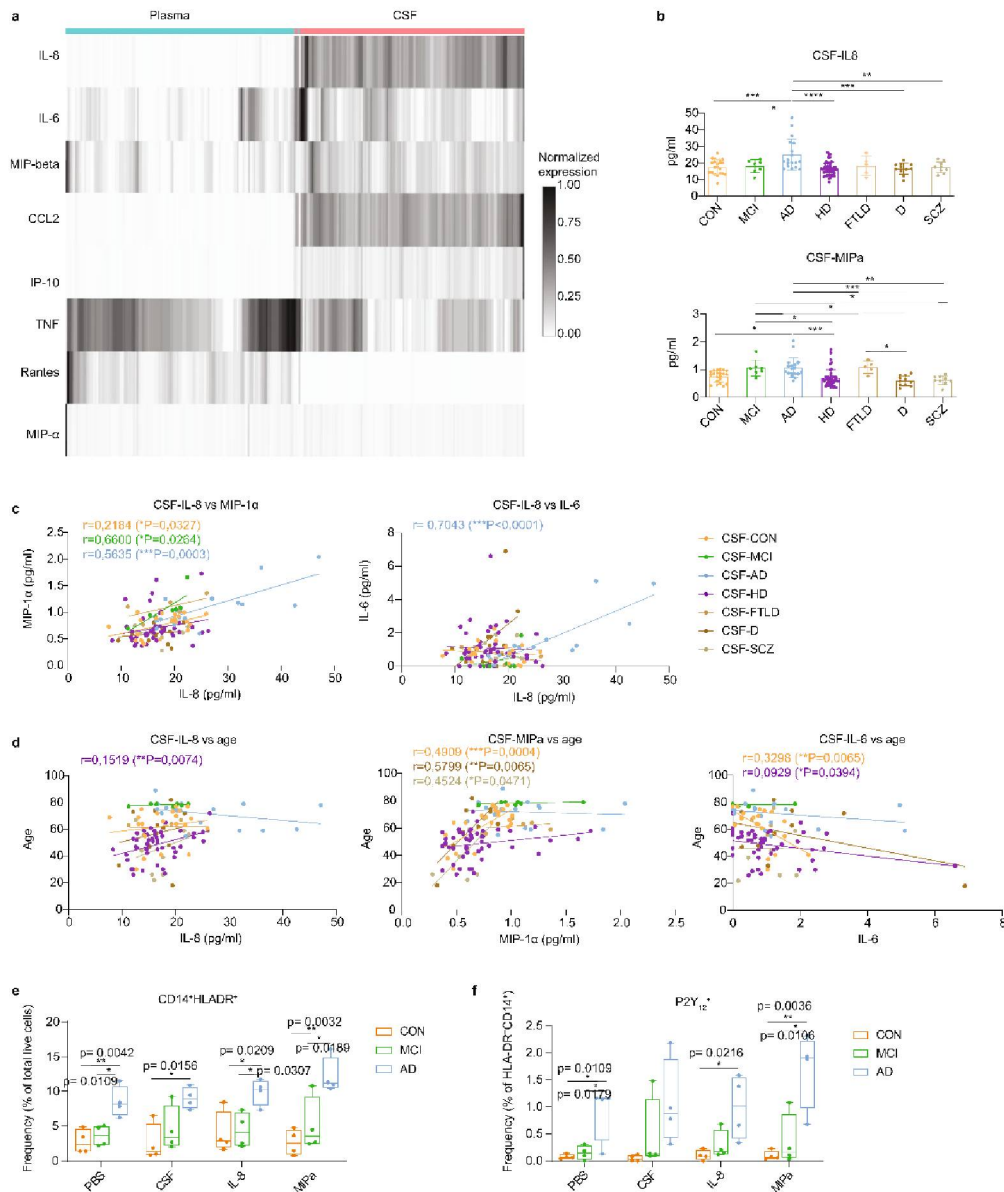
<https://doi.org/10.1038/s41467-022-34719-2>


Fig. 4 | Differential concentration of inflammatory mediators between plasma ($n = 117$, biological replication) and CSF ($n = 117$, biological replication) determined using Luminex protein array. These are CON individuals ($n = 21$) and patients with MCI ($n = 7$), AD ($n = 18$), HD ($n = 46$), depression ($n = 11$), FTLD ($n = 5$) and SCZ ($n = 9$) individuals. **a** Heatmap showed the expression of IL-8, IL-6, MIP- β , CCL2, IP-10, TNF, Rantes (CCL5) and MIP-1a that were quantified in plasma and CSF. **b** Bar graphs show differential concentrations (pg/ml) of IL-8 and MIP- α in the CSF of patients with AD, compared to CON individuals and patients with other diseases. Each dot represents the value of each sample. Data displayed as mean \pm SD. One-way ANOVA with the Tukey's multiple comparisons; $^{*}p < 0.05$, $^{**}p < 0.01$ and $^{***}p < 0.001$. **c** Scatter plots showing correlation between mean CSF-concentration of IL-8 and MIP- α or IL-6 of all groups. $^{*}P < 0.05$, $^{**}P < 0.01$ and $^{***}P < 0.001$, non-parametric Spearman correlation test (r), two-sided. **d** Scatter plots showing

correlation between mean IL-8 and MIP- α or IL-6 concentration and age of all groups. $^{*}P < 0.05$, $^{**}P < 0.01$ and $^{***}P < 0.001$, non-parametric Spearman correlation test (r), two-sided. **e, f** Results obtained from in vitro experiments, in which PBMCs from CON ($n = 4$, biological replications), AD ($n = 4$, biological replication) and MCI ($n = 4$, biological replication) individuals treated with either PBS, CSF, IL-8 or MIP- α . Flow cytometry analysis revealed increased frequency of CD14⁺HLA-DR⁺ cells (% of total live cells, **e**) and P2Y₁₂⁺ cells (% of HLA-DR⁺CD14⁺ cells, **f**) in AD-PBMCs after in vitro incubation (PBS) or after treatments (CSF, IL-8 and MIP- α). Boxes extend from the 25th to 75th percentiles. Whisker plots show the min (smallest) and max (largest) values. The line in the box denotes the median. Each dot represents the value of each sample. Ordinary one-way ANOVA; $^{*}p < 0.05$, $^{**}p < 0.01$, $^{***}p < 0.001$. Source data (for **b, c, d, e** and **f**) are provided as a Source Data file.

Article

<https://doi.org/10.1038/s41467-022-34719-2>

in vitro environment. Flow cytometry analysis (Supplementary Fig. 4) revealed higher proportion of the CD14⁺HLADR⁺ myeloid cell subset in AD-PBMCs in vitro, compared to CON- and MCI-PBMCs. However, this difference was comparable between AD-PBMCs treated with CSF, IL-8, MIP-1 α and PBS (Fig. 4e), suggesting that AD-PBMCs are more vulnerable to environment changes such as transferring cells to an in vitro environment or possibly from the peripheral blood to the CSF. Interestingly, this CD14⁺HLA-DR⁺ cell population in AD showed higher proportion of P2Y₁₂⁺ cells, compared to CON and MCI, but the proportion remained comparable between treatments (Fig. 4f). To in-depth characterize phenotypic and functional changes of myeloid cells after exposure to CSF, we performed another in vitro experiment using PBMCs isolated from CON individuals, and patients with AD and MCI. The PBMCs were treated with either only paired-CSF or both paired CSF and lipopolysaccharide (LPS), and labelled with a CyTOF-antibody panel (see Supplementary Table 4 for the panel of 37 antibodies). The CD3⁺CD19⁻ cell population was first pre-gated and analyzed using the data analysis workflow as described above (Figs. 1, 2 and Supplementary Fig. 1a). The MDS plots showed no completely clear phenotypic differences between conditions (i.e. no stimulation, CSF and CSF + LPS) or between diseases (i.e. CON, MCI and AD) (Fig. 5a, b). Using clustering analysis, 20 clusters were identified (Fig. 5c, d). Similar to results obtained from flow cytometry analysis, we detected increased proportion of CD14⁺HLADR⁺ cells (cluster 1) in AD-PBMCs, compared to the CON-PBMCs, especially in AD-PBMCs treated with CSF and LPS (Fig. 5e). These cells are characterized as CD14⁺HLADR⁺CD16⁺CCR2^{low}CD68^{hi}CD11c⁻CD141⁺CCR6⁺ (Fig. 5d), which have a similar phenotype as the CCR2^{low}CD68^{hi}CD11c⁻HLADR⁺D16⁺ CSF-enriched myeloid cells (cluster 16 in Fig. 2). Interestingly, the expression of P2Y₁₂ receptor, IL-8, MIP-1 β , TNF and CXCR3 in this cluster were found to be increased after exposure to CSF and after treatment with LPS, especially in PBMCs from patients with AD (Fig. 5f). These findings support our results shown in Figs. 1–2 (i.e. increased activation phenotype of myeloid cells after exposure to CSF). The results also strengthen our hypothesis that the P2Y₁₂⁺ myeloid cells detected in CSF may be derived from the peripheral blood myeloid cells (possibly from CD14⁺CD16⁺CCR2^{low} monocytes), which increase P2Y₁₂ expression upon entry to the CSF compartment. Furthermore, our findings demonstrated that AD-PBMCs are more vulnerable than CON- or MCI-PBMCs to inflammatory stimulation. In addition, we also detected an increased abundance of CD56⁺CD11c⁻ NK cells (cluster 4, Fig. 5g and Source Data) in MCI-PBMCs, compared with CON- and AD-PBMCs (Fig. 5h). But the proportion of this population was comparable between treatments (i.e. no stimulation, CSF and CSF + LPS). However, we detected increased expression of CXCR3 of CD56⁺CD11c⁻ cells after exposure to CSF and CSF + LPS (Fig. 5i), suggesting phenotypic changes also in the NK cell population.

Next, we treated PBMCs isolated from a healthy donor with CSF obtained from six control individuals or six patients with AD. In addition to CSF, PBMCs were also stimulated with LPS (similar to the experiment shown in Fig. 5). Cells were analyzed using CyTOF workflow as described above. Twenty clusters were identified (Fig. 6a; Supplementary Table 5 for the panel of 40 antibodies used in Fig. 6). An MDS plot showed small changes in phenotype of myeloid cells after co-incubation with CSF, compared to non-stimulated cells (Fig. 6b). As expected, cells treated with LPS and both CSF and LPS (CSF + LPS) showed distinct overall phenotypes, compared with no stimulation and CSF-treated groups (Fig. 6b). We detected increased proportions of two small clusters with mixed phenotypes (cluster 6 and 15) in CSF and CSF + LPS-treated PBMCs (Fig. 6c, d). Compared with all other cell subsets, these two clusters expressed higher level of CD69, CD49d and IL-10 (Fig. 6e). Similar to CD14⁺CD16⁺CCR2^{low} CSF-enriched myeloid cell subsets described above (Figs. 2 and 5), CD14⁺ cluster 15 showed different phenotypes when compared to the CD14⁺CCR2⁺ monocytes (Cluster 19). These differences include a higher expression level of

P2Y₁₂ and CD16, but a lower CCR2 expression (Fig. 6f, g). In addition, myeloid cell subsets (Cluster 8, 16, 18 and 19) in CSF + LPS-treated samples showed consistently higher expression of inflammatory cytokines such as TNF, MIP-1 β and IL-1 β (Fig. 6h), in comparison to LPS-treated PBMCs. Of note, no differences in phenotypes and responses to LPS were detected between cells treated with AD-CSF and those treated with CON-CSF.

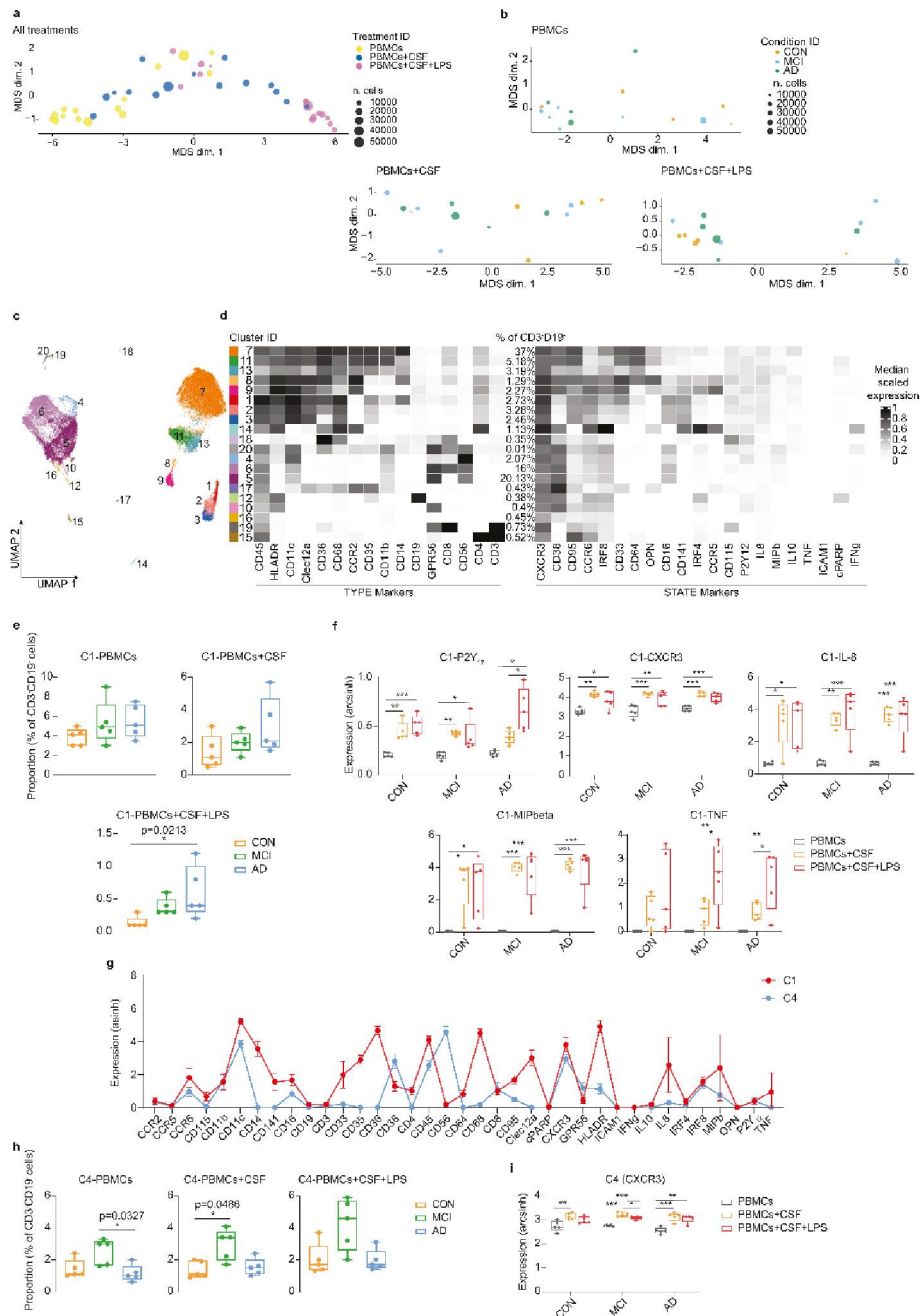
Together, we detected big changes in metabolic profiles of myeloid cells after exposure to CSF in vitro (as shown in Fig. 3), but only small changes in phenotypes and responses to LPS of these cells could be detected after CSF treatment (as shown in Figs. 5 and 6). Incubating myeloid cells from patients with AD in the presence of the paired CSF (with and without LPS) could induce more phenotypic changes than when healthy myeloid cells were treated with CSF (with and without LPS). Our findings suggest that myeloid cells of patients with AD may already be primed in the peripheral blood (possibly without significant changes in phenotypes), and thus are more vulnerable to LPS stimulation.

Differential myeloid cell phenotypes in choroid plexus (CP) and brain parenchyma

Next, we characterized differences in phenotypes and abundant clusters of myeloid cells between the brain barrier (i.e. choroid plexus, CP) and the brain parenchyma (i.e. gyrus frontalis medialis, GFM). Since the brain tissue of AD patients is only available post-mortem, we were not able to perform the investigation in the same individuals as were used for the blood and CSF determination. Furthermore, it should be mentioned that this study is limited to the changes at the late state of the disease (i.e. post-mortem).

We performed CyTOF analyses with pre-sorted CD45⁺ cells isolated from post-mortem CP and GFM of AD and non-neurological donors (Supplementary Table 1 and Supplementary Fig. 5). First, we characterized isolated cells using an antibody panel (Panel A), focusing on known immune cell populations (see Supplementary Table 6 for the list of 35 antibodies used). The UMAP plots of the obtained CyTOF data showed different cellular compositions between CP and GFM compartments (Fig. 7a). The downstream clustering analysis of all data together (i.e. across all cells of all CP and GFM samples) revealed a total of 14 distinct cell clusters (Fig. 7b, c). Higher proportion of macrophages, monocytes and lymphocytes was detected in CP, whereas IRF8^{hi} (Cluster 9, 10 and 12) microglia/macrophages were the majority in GFM (over 80% of total cells, Fig. 7d). Similar to previous study in mouse CNS³⁵, we detected a small population of CP-macrophages (i.e. border-associated, Kolmer's epi-plexus macrophages, CP^{epi}-BAM) whose phenotypic signature reminiscent of microglia, and were clustered together with GFM microglia (Cluster 10: IRF8^{hi}CD11c⁻HLA-DR⁺EMR1⁺GPR56⁺). Compared with the GFM-microglia, CP^{epi}-BAM expressed a higher level of markers involved in phagocytosis and cell activation including CD206, CD64, HLA-DR, CD44, CCR5, CD68, MS4A4A, CD32 and CD14 (Fig. 7e and Source Data). Although we could not detect differences in cellular compositions within the CP compartment between the CON and AD groups, we detected some markers differentially expressed in both myeloid and lymphoid cell populations between the groups. Collectively, we found lower expression of EMR1, IRF8, CD14, CD86 and C3 in myeloid cells from AD donors, whereas ABCA7, CD61 and CCR5 were found increased (Fig. 7f). Analogous to the CP, no differences in cluster abundance were found between AD-GFM and CON-GFM. Also in line with the results from CP analysis, myeloid cell clusters (cluster 1 and 7) in AD-GFM showed higher expression of CCR5 and CD6L. The microglia cluster, cluster 12, of AD-GFM expressed lower level of CXCR3 and CD4. To further characterize myeloid cells in these two compartments, we have utilized the antibody Panel B (Supplementary Table 7, a total of 35 markers) consisting of functional markers such as the thrombospondin 1 receptor CD47 (a "don't eat me" signal), the extracellular ligand of CD172a) and MIP-1 β

Article

<https://doi.org/10.1038/s41467-022-34719-2>

(CCL4, a CC chemokine with specificity for CCR5). Similar to the results shown in Fig. 7, the cellular composition of CP was different from that of GFM, as shown by UMAP plots (Fig. 8a). Among the 14 defined clusters (Fig. 8b, c), we detected a higher proportion of P2Y₁₂^{low}/myeloid cells in CP, compared with GFM, whereas P2Y₁₂^{hi} microglia/macrophages (Cluster 8, 10 and 13) were mainly found in GFM (Fig. 8d).

The results obtained from the antibody *Panel B* confirmed the similarity between GFM microglia and the CP^{hi}-BAM (Cluster 8: P2Y₁₂^{hi}CD11c⁺CD64⁺Glut5⁺, Fig. 8d, e, Source Data). Similar to the *Panel A*, we could not detect differentially abundant clusters between CON and AD in both compartments using the antibody *Panel B*. Comparing AD-CP macrophages with those in CON-CP revealed increased

Article

<https://doi.org/10.1038/s41467-022-34719-2>

Fig. 5 | Assessment of paired-CSF-induced phenotypic changes in the myeloid cells from patients with AD ($n = 5$, biological replications) and MCI ($n = 5$, biological replications), in comparison with CON ($n = 5$, biological replications) cells. a MDS plot for all PBMCs at different conditions. **b** MDS plots for each treatment, colour-coded by condition (CON, MCI or AD). Each dot represents a sample and dot size depicts total number of cells per sample. **c** The overlaid UMAP plot of all samples. The colouring indicates 20 clusters representing diverse immune cell phenotypes, defined by the *FlowSOM* algorithm. **d** Phenotypic heatmap of cluster identities depicting the expression levels of 16 TYPE markers used for the cluster analysis and 21 STATE markers. Heat colours of expression levels have been scaled for each marker individually (to the 1st and 5th quintiles) (black, high expression; white, no expression). **e** Proportion of Cluster 1 (C1) between groups and conditions. Kruskal–Wallis test; * $P < 0.05$, ** $P < 0.01$, *** $P < 0.001$ and

**** $p < 0.0001$. **f** Differences in marker expression of P2Y₁₂, CXCR3, IL-8, MIPβ in cells from Cluster 1 between conditions. Ordinary one-way ANOVA; * $P < 0.05$, ** $P < 0.01$, *** $p < 0.001$ and **** $p < 0.0001$. **g** Line graph of the arcsinh marker expression (mean ± SD) between Cluster 1 and Cluster 4 (FDR-adjusted Mann–Whitney *U*-test, two-sided, adjusted, two-sided). **h** Proportion of C4 (% of CD3⁺CD19⁺ cells) between groups and conditions. Kruskal–Wallis test; * $P < 0.05$, ** $P < 0.01$, *** $p < 0.001$ and **** $p < 0.0001$. **i** Difference in marker expression of CXCR3 in cells from Cluster 4 between conditions. All boxes extend from the 25th to 75th percentiles. Whisker plots show the min (smallest) and max (largest) values. The line in the box denotes the median. Each dot represents the value of each sample. Ordinary one-way ANOVA; * $P < 0.05$, ** $P < 0.01$, *** $p < 0.001$ and **** $p < 0.0001$. Source data (for e, f, g, h and i) are provided as a Source Data file.

expression of CD206, CD163, CD91, CD33, CD172a (SIRPα, the receptor of CD47) and Clec12A, whereas CD64, CD68, CD18 and CD47 were downregulated in AD-CP (Fig. 8f). These changes may reflect an inefficient or even suppressed phagocytosis in macrophages isolated from AD-CP. Both microglia subsets (cluster 10 and 13) from AD-GFM showed a higher level of the inflammatory mediator MIP-1β (CCL4, a CC chemokine with specificity for CCR5), whereas CD64 and CD172a were found downregulated in AD-microglia (Fig. 8f). The macrophage subsets (cluster 4, 6 and 9) of AD-GFM showed higher expression level of CD172a, CD11b, CD18, Clec12A and the thrombospondin 1 receptor, CD47 (Fig. 8f), suggesting increased phagocytic phenotypes of the infiltrating macrophages detected in AD-GFM, whereas microglia at this late stage of disease were rather a source of chemoattractant for monocytes and macrophages.

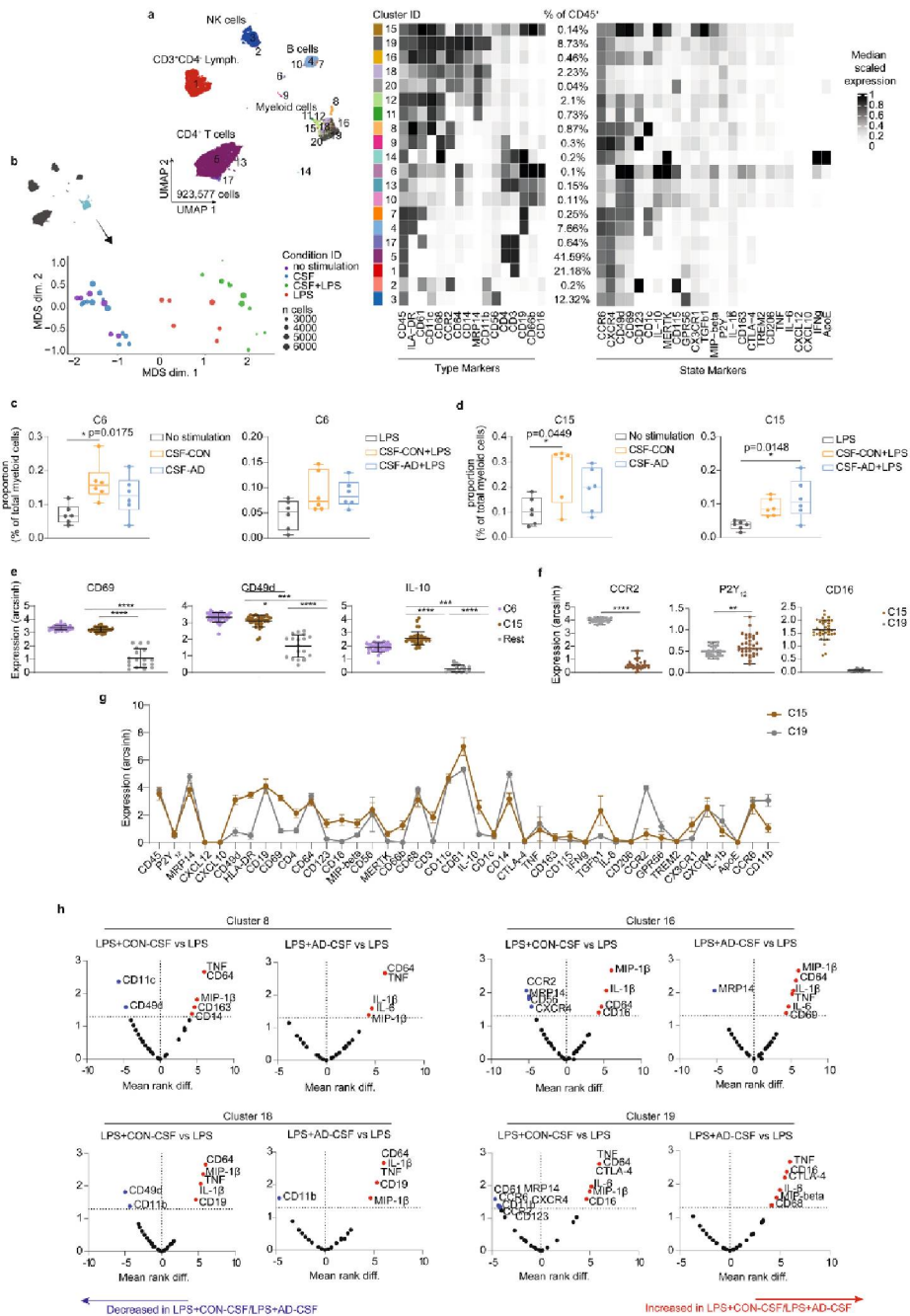
Discussion

Myeloid cells including monocytes, macrophages and microglia have long been suggested as key players in neuroinflammation and neurodegeneration like AD^{3,36}. Numerous findings in rodent models of AD highlight the importance of diverse myeloid cells including microglia, monocytes and monocyte-derived macrophages^{6,16} in the pathology. However, these models only partially replicate the complexity of the rare familial AD, our understanding of how myeloid cells either respond or contribute to the pathogenesis of human AD including sporadic AD is still limited. In this study, we characterized and compared myeloid cells isolated from the peripheral blood, CSF, CP and GFM of either control individuals (i.e. without neurological diseases), or patients with AD, MCI or HD. Using multiple state-of-the-art analytical methods, we identified differences in myeloid cell composition and phenotypes, as well as their bioenergetic pathway across different compartments (i.e. blood and CSF) and diseases. Our findings showed that myeloid cells alter their activation phenotypes and inflammatory responses across different compartments, and this continuum of phenotypic changes and functional responses may be more pronounced in neuropathology such as AD. Overall, we could consistently detect in the CSF an increased proportion of myeloid cells with changes in activated, inflammatory and/or phagocytic phenotypes, which was characterized by increased expression of markers involved in these processes including P2Y₁₂ receptor, CD16, CCR5, ApoE, CD11c, HLA-DR, CD169 (SIGLEC-1), CD91 and MS4A4A. Although differences in phenotypes and responses of myeloid cells between different conditions (i.e. CON vs diseases) were small within the peripheral blood and CSF compartment, we have detected phenotypic and metabolic changes in AD compared to the CON and/or other diseases in the CP and brain parenchyma as well as *in vitro*. These differences were more pronounced in AD-myeloid cells after additional stimulation with LPS, suggesting that myeloid cells from AD patients are more likely vulnerable to environment change. These results are in agreement with previous studies dismissing major phenotypic changes in unstimulated PBMCs from AD donors but that have found significantly changed upon response to stimulation²⁴. On the basis of our findings,

microglia in the GFM showed less phagocytic but more inflammatory phenotypes, in comparison to the infiltrating macrophages at this late stage of the disease (i.e. post-mortem). Nonetheless, due to the limitations of our study (e.g. low cell number in the CSF, high biological variation between individuals and availability of multiple body compartments from the same individuals), the findings should be interpreted with caution.

Upon entry to the CSF compartment, myeloid cells including monocytes increased the expression of markers associated with the inflammatory process including P2Y₁₂ receptor, CCR5, ApoE, CD169 and its co-activator MS4A4A³⁷. Interestingly, CD169 (or Siglec1) was proposed as an indicator of the activity in an inflammatory CNS, due to the results showing that CD169-expressing myeloid cells were abundantly located in an active inflammatory site of the CNS, including in active multiple sclerosis lesions, acute infectious and malignant diseases. Such cells were suggested to support the activation of adaptive immune responses³⁸. Soluble triggering receptor expressed on myeloid cells 2 (sTREM2) in CSF is hypothesized to increase in response to microglial activation due to neurodegenerative processes and is elevated in AD^{39,40}. MS4A4A is a key modulator of sTREM2⁴¹. Targeting MS4A4A at the molecular or protein level was sufficient to significantly reduce sTREM2, thus can potentially be used for AD therapy. We hypothesize that myeloid cells are recruited into the CSF and become inflammatory, which may be a mechanism to regulate the adaptive immune responses in this compartment barrier. Together with an increased expression of IL-8 (a potent chemotactic factor for myeloid cells) in the AD CSF, which is positively correlated with IL-6 and MIP-1α (CCL3, a ligand of CCR5) expression, we propose that, in AD, CCR5-expressing myeloid cells including monocytes are recruited into the CSF, become activated and associated to the activation of adaptive immune cells. In mouse models of AD, it has been shown that Aβ could stimulate the production of IL-8 and MIP-1α from monocytes or microglia. The MIP-1α/CCR5-signalling pathway that was induced by Aβ could result in increased lymphocyte transendothelial migration to the brain⁸. Interestingly, studies in 5xFAD mice have shown that knocking out CD33 and TREM2, both known risk factors for sporadic AD, induce changes in IL-6 and IL-8 expression by microglia, and that downregulation of both signalling molecules is associated with increased neurodegeneration⁴².

In the CNS, the purinergic P2Y₁₂ receptor (an adenosine diphosphate responsive G protein-coupled receptor) is widely recognized as a marker that is selectively expressed on microglia. In the periphery, this receptor can however be detected in multiple cell types including eosinophils⁴³, platelets, osteoclasts, vascular smooth muscle cells, dendritic cells⁴⁴ and macrophages⁴⁵. Moreover, during chronic neuroinflammation, CNS-infiltrating macrophages also acquire P2Y₁₂ receptor⁴⁶, thus caution should be taken in the strict definition of microglia-specific marker and plasticity of myeloid cells in the niche of different body compartments. In our previous study, we have also shown low P2Y₁₂ expression on brain CD206⁺ macrophage²⁷. In the brain, P2Y₁₂-expressing macrophages/microglia were found



significantly reduced in multiple sclerosis and AD^{26,46}. However, its role in neuroinflammation or neurodegeneration remains largely unclear. In contrast to previous studies showing that these P2Y₁₂⁺ cells were microglia-like cells that are solely found in the CSF of patients with neuroinflammation^{30,31}, we identified these cells in both CSF (with much higher abundance) and the peripheral blood of both healthy

donors and patients with neurological disorders. Furthermore, we could also demonstrate that some subsets of blood monocytes increased P2Y₁₂ expression after exposure to the CSF, and thus provide an alternative hypothesis for the origin of P2Y₁₂⁺ cells in the CSF, namely that they may be derived from blood monocytes that respond to (most likely) soluble factors in the new environment. Interestingly,

Article

<https://doi.org/10.1038/s41467-022-34719-2>

Fig. 6 | Phenotypic changes in healthy PBMCs after treatment with CSF from CON ($n = 6$, biological replication) or AD ($n = 6$, biological replication) patients. **a** UMAP plots from all cells coloured by cluster ID for 1–20 clusters determined using the *FlowSOM* algorithm, phenotypic heatmap of median marker expression per cluster. **b** MDS plot for myeloid cells (light blue dots) obtained from all conditions, i.e. no stimulation (purple dots) or CSF (blue dots), CSF + LPS (green dots) and LPS (red dots). **c, d** Proportion (% of CD45⁺ cells) of Cluster 6 (c) or Cluster 15 (d) between treatments. All boxes extend from the 25th to 75th percentiles. Whisker plots show the min (smallest) and max (largest) values. The line in the box denotes the median. Each dot represents the value of each sample. Ordinary one-way ANOVA; * $p < 0.05$. **e** Mean signal intensity levels of CD69, CD49d and IL-10 staining in cluster 6 and 15, compared to the other cells (rest) (black lines show mean \pm SD

values of the datasets). Kruskal–Wallis test, * $p < 0.05$ and **** $p < 0.0001$. **f** Scatter plots show the differential expression of CCR2, P2Y₁₂ and CD16 of Cluster 15, compared to CD14⁺CD16⁺ classical monocytes (Cluster 19). Data displayed as mean \pm SD. Kruskal–Wallis test, ** $p < 0.01$ and **** $p < 0.0001$. **g** Line graph shows different marker expressions (arcsinh) (mean \pm SD) between Cluster 15 and Cluster 19. **h** Volcano plots show differential expression of all markers in myeloid cell clusters (Cluster 8, 16, 18 and 19) after AD-CSF + LPS or CON-CSF + LPS treatment, in comparison to LPS treatment. Red dots indicate markers with significantly increased expression; blue dots the markers with significantly decreased expression, whereas black dots are non-significant markers, determined using Mann–Whitney *U*-Test, two-sided ($p < 0.05$ is statistically significant). Source data (for c, d, e and f) are provided as a Source Data file.

treating PBMCs from AD-patients with the paired CSF in vitro resulted in increased proportion of myeloid cells showing a similar phenotype as CSF-enriched myeloid cells, characterized as P2Y₁₂⁺CD14⁺CD16⁺C2^{low}. This change was more significant when the cells were additionally stimulated with LPS. Furthermore, we showed that this cluster produced more IL-8 and inflammatory MIP-1 β after exposure to CSF and LPS, suggesting a possible source of IL-8-expressing myeloid cells in CSF.

In addition to phenotypic changes in the myeloid cells of the CSF, results obtained from Seahorse and ¹³C-glucose tracing experiment showed that blood monocytes are more glycolytically active after exposure to the CSF, suggesting an inflammatory response rather than anti-inflammatory phenotype, which would more likely increase mitochondrial respiration³³. Upregulation of glycolytic metabolism was proposed to support phagocytotic function via ATP production³².

Besides brain macrophages and microglia, myeloid cells in CP have been also proposed as one of the key players in human AD pathology. CP is a unique organ exposed to peripheral blood and CSF, forming the blood-CSF-barrier (BCSFB), which effectively separates the brain parenchyma from the peripheral blood, and regulates neuronal homeostasis. CP allows efficient exchange of essential gases, nutrients and waste products of metabolism between blood, CSF and interstitial fluid of the brain³⁷. This barrier also efficiently removes cell debris and larger waste products including β -amyloid⁴⁸. The CP inner stroma is richly irrigated by fenestrated capillaries, which facilitate the passage of circulating macromolecules and immune cells into this compartment. However, under healthy conditions this BCSFB restricts immune cell entry into the CSF and the brain parenchyma⁴⁹. Dysfunction of this system may play an aetiological role in neurological disorders including AD, thus the analysis of cellular and molecular composition in CSF and peripheral blood in comparison with the CNS system provides invaluable information to biological and/or disease processes of AD.

At the late stage of AD (post-mortem), we detected increased expressions of markers involved in phagocytosis in the CP macrophages, whereas myeloid cells in the GFM increased the don't eat me signal CD47 and its receptor CD172a (SIRP α). At this stage, microglia served most likely as a source of MIP-1 β (CCL4), a ligand for CCR5 and chemoattractant inducing migration of phagocytic macrophages into the brain. Our findings are in line with the concept of dystrophic microglia in late-onset AD, in which microglia are unable to remove aggregated amyloid, present as an exhausted phenotype and with exacerbated aging-dependent microglia deterioration⁵⁰.

In conclusion, based upon our findings, we propose that myeloid cells in the CSF present activation phenotypes (e.g. changes in bioenergetic pathways, phenotypic changes and increase phagocytic activity) which may help our system to defend against pathologic stimuli and/or to regulate the activation of adaptive immunity. Once this process becomes dysregulated (such as in AD), it could lead to chronic inflammation in different compartments, which could further harm the system, such as dysregulation of T cell activation and colonization⁵¹. At

the late stage of the disease (post-mortem), we detected increased inhibitory signalling on myeloid cells and exhausted microglia with inflammatory phenotypes. However, numerous open questions remain unanswered, including (1) what is the biological function of P2Y₁₂⁺ myeloid cells in the CSF and CP, and whether these cells are recruited from the brain or the peripheral blood? (2) Which soluble factors in CSF and/or CP drive the differentiation of the myeloid cell population? On one hand, these open questions can be hardly answered by using animal models, due to large differences in immune cell regulation and differentiation between species, on the other hand, solving these questions using human systems is ethically and technically challenging. To our opinion, development of a proper ex vivo/in vitro model of human system (such as organoid culture) consisting of circulation would serve as a promising system for studying this complex interaction between the peripheral and the central system.

Methods

This study complies with all relevant ethical regulations and was approved by the Ethics Commission of Charité–Universitätsmedizin Berlin (Ethikkommission der Charité–Universitätsmedizin Berlin; registration number EA1/187/17 and EA1/241/17), Berlin, Germany. All study participants provided informed consent before any study-related procedures were undertaken. All participants received no compensation.

Human blood and CSF samples

Venous blood and lumbar cerebrospinal fluid (CSF) samples ($n = 117$) were obtained from control individuals ($n = 21$) or patients with AD ($n = 18$), MCI ($n = 7$), HD ($n = 46$), depression ($n = 11$), FTLD ($n = 5$) and SCZ ($n = 9$) (Supplementary Table 1). PBMCs were isolated from EDTA-blood (20 ml) within 1 h of the blood draw through Biocoll (Biochrom GmbH, Berlin, Germany) density centrifugation at 1200 \times g for 20 min at room temperature. The blood mononuclear cell fraction was recovered and washed twice in phosphate-buffered saline (PBS; Biochrom GmbH) at 300 \times g for 10 min. For the isolation of CSF cells, CSF was centrifuged once at 300 \times g for 10 min (4 °C). The cell pellet (PBMCs or CSF cells) was then fixed with fixation/stabilization buffer (SmartTube) and frozen at –80 °C until analysis by mass cytometry. PBMCs and CSF cells of a total of eleven CON, eight AD, seven MCI and twelve HD out of those 117 samples were used for CyTOF analysis.

Human brain autopsy

Human brain tissue was obtained through the Netherlands Brain Bank (www.brainbank.nl). The Netherlands Brain Bank received permission to perform autopsies and to use tissue and medical records from the Ethical Committee of the VU University medical center (VUmc, Amsterdam, The Netherlands). All donors have given informed consent for autopsy and use of their brain tissue for research purposes. Generally, the autopsies of frontal lobe (Gyrus frontalis medius, GFM) and choroid plexus were performed within 4–10 h after death (Supplementary Table 1). Brain tissue collected

Article

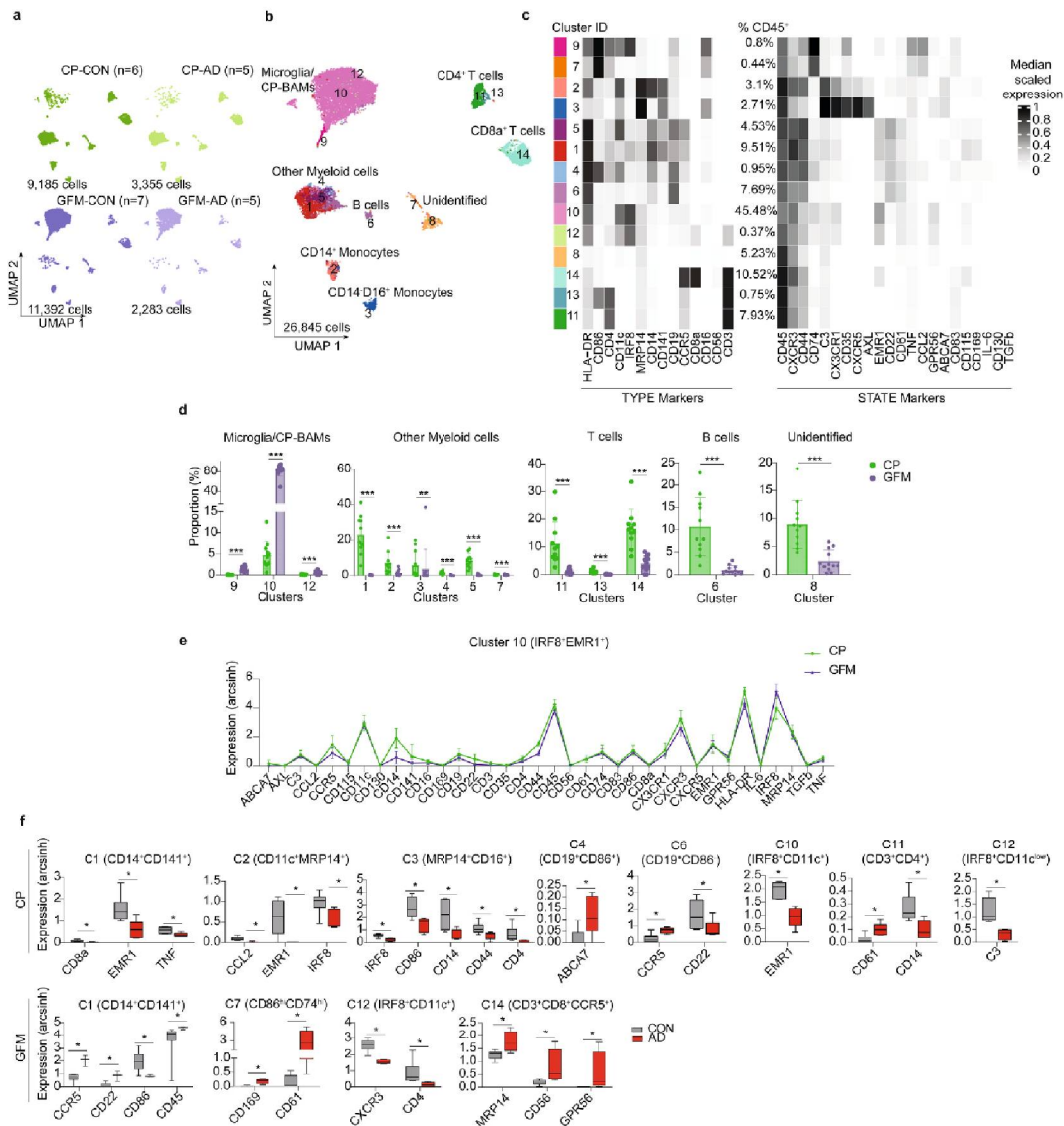
<https://doi.org/10.1038/s41467-022-34719-2>

Fig. 7 | Differential heterogeneity of CD45⁺ immune cells in CP and GFM of AD donors, compared to the CON donors, determined by using Panel A (CP: CON, n = 7; AD, n = 4, GFM: CON, n = 7; AD, n = 5, biological replication). a Overlaid UMAP plots of CP and GFM samples from AD (green dots) and CON (purple dots) donors. **b** UMAP plots of all samples. The colouring indicates 14 clusters representing diverse immune cell phenotypes, defined by the *FlowSOM* algorithm. **c** Phenotypic heatmap of cluster identities depicting the expression levels of 14 TYPE markers used for the cluster analysis and 22 STATE markers. Heat colours of expression levels have been scaled for each marker individually (to the 1st and 5th quintiles) (black, high expression; white, no expression). **d** The bar graphs show differentially abundant clusters between CP and GFM. Data displayed as mean \pm SD.

An FDR-adjusted p -value < 0.05 was considered statistically significant, determined using the edgeR test for differential cluster abundance (* p < 0.05; ** p < 0.01; *** p < 0.001). **e** The graphs showed differential marker expression (mean \pm sd) between the CP^{IR8}-BAM in CP and microglia in GFM (both are defined as cluster 10). FDR adjusted Mann–Whitney U -test, two-sided; * p < 0.05 is considered significant. **f** The Box plots shows differential marker expression of immune cells in CP or in GFM of AD donors, compared with the CON donors, using Mann–Whitney U -Test, two-sided. The p -value < 0.05 (*) is considered statistically significant. Boxes extend from the 25th to 75th percentiles. Whisker plots show the min (smallest) and max (largest) values. The line in the box denotes the median. Each dot represents the value of each sample. Source data (for **d**, **e** and **f**) are provided as a Source Data file.

for this study was from the donors whose post-mortem CSF was between pH 5.9 and 6.9 (Supplementary Table 1). An overview of the donor information and post-mortem variables is summarized in Supplementary Table 1.

Human brain immune cell isolation

The isolation was started within 2–25 h after autopsy. Approximately, 2–10 grams tissue was first mechanically dissociated through a metal sieve in a glucose-potassium-sodium buffer (GKN-BSA; 8 g/l NaCl,

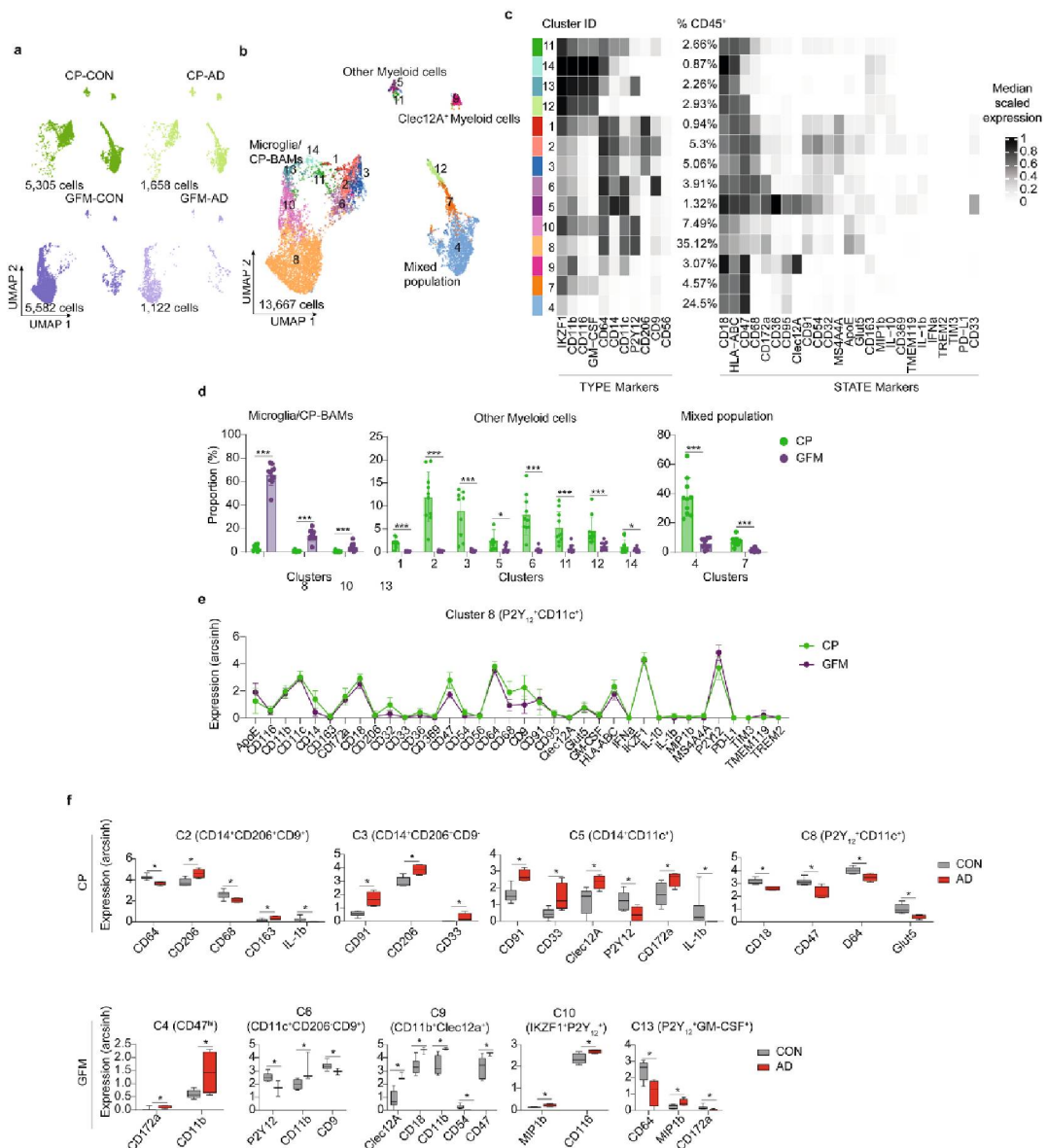


Fig. 8 | Differential heterogeneity of CD45⁺ immune cells in CP and GFM of AD donors, compared to the CON donors, determined by using Panel B (CP: CON, *n* = 7; AD, *n* = 3, GFM: CON, *n* = 7; AD, *n* = 4, biological replication). a Overlaid UMAP plots of CP and GFM samples from AD (green dots) and CON (purple dots) donors. **b** UMAP plots of all samples. The colouring indicates 14 clusters representing diverse immune cell phenotypes, defined by the FlowSOM algorithm. **c** Phenotypic heatmap of cluster identities depicting the expression levels of 10 TYPE markers used for the cluster analysis and 25 STATE markers. Heat colours of expression levels have been scaled for each marker individually (to the 1st and 5th quintiles) (black, high expression; white, no expression). **d** The bar graphs show differentially abundant clusters between CP and GFM. Data displayed as mean ± SD.

An FDR-adjusted *p*-value < 0.05 was considered statistically significant, determined using the edgeR test for differential cluster abundance (**p* < 0.05; ***p* < 0.01; ****p* < 0.001). **e** Line graphs showing differential marker expression (mean ± sd) between the CP^{HL}-BAM in CP and microglia in GFM (both are identified as cluster 8). FDR-adjusted Mann–Whitney *U*-test, two-sided; **p* < 0.05 is considered significant. **f** The Box plots shows differential marker expression of immune cells in CP or in GFM of AD donors, compared with the CON donors, using Mann–Whitney *U*-Test, two-sided. The *p*-value < 0.05 (*) is considered statistically significant. Boxes extend from the 25th to 75th percentiles. Whisker plots show the min (smallest) and max (largest) values. The line in the box denotes the median. Each dot represents the value of each sample. Source data (for **d**, **e** and **f**) are provided as a Source Data file.

Article

<https://doi.org/10.1038/s41467-022-34719-2>

0.4 g/l KCl, 1.77 g/l $\text{Na}_2\text{HPO}_4 \cdot 2\text{H}_2\text{O}$, 0.69 g/l $\text{NaH}_2\text{PO}_4 \cdot \text{H}_2\text{O}$, 2 g/l D-(1)-glucose, 0.3% bovine serum albumin (BSA, Sigma-Aldrich); pH 7.4). The samples were then supplemented with collagenase Type I (3700 units/ml; Worthington, Lakewood, NJ, USA) and DNase I (200 $\mu\text{g}/\text{ml}$; Roche Diagnostics GmbH) for 1 h at 37 °C while shaking. Cell suspension was put over a 100 μm cell strainer and washed with GKN-BSA buffer before the pellet was resuspended in 20 ml GKN-BSA buffer. Next, 10 ml of Percoll (Amersham, GE Healthcare) was added dropwise and tissue was centrifuged at $3220 \times g$ for 30 min (4 °C). Three different layers appeared: upper layer containing myelin, a lower erythrocyte layer and the middle layer containing all cell types including microglia. The middle layer was carefully taken out without disturbing the myelin layer and washed first with GKN-BSA buffer, followed by cell sorting using flow cytometry.

Fluorescence-activated cell sorting

The single-cell suspension was incubated with an FC receptor blocking reagent (Miltenyi Biotec, 5170126102) (1:20) and anti-CD45 (eBioscience, 11-9459) antibodies (1:20) at 4 °C for 15 min. Cells were washed twice and suspended in glucose-potassium-sodium buffer (GKN-BSA; 8 g/L NaCl, 0.4 g/L KCl, 1.77 g/L $\text{Na}_2\text{HPO}_4 \cdot 2\text{H}_2\text{O}$, 0.69 g/L $\text{NaH}_2\text{PO}_4 \cdot \text{H}_2\text{O}$, 6 g/L D-(1)-glucose, pH 7.4) with 0.3% BSA. 7-AAD (BD Biosciences, 5168981E) (1 $\mu\text{g}/\text{mL}$) was added for cell death detection. Cells were filtered over a 70 μm cell strainer before sorting. Cells were sorted/gated that were alive, single, and CD45⁺ with the FACS Aria III. The sorted CD45⁺ fraction (Supplementary Fig. 5) was placed on ice, centrifuged at 300xg for 5 min, supernatant removed, and pellet was fixed with fixation/stabilization buffer (SmartTube) and stored at -80 °C.

Barcoding

Live cell barcoding. Individual CSF samples ($0.5\text{--}1 \times 10^7$ cells) were pelleted and stained with ⁹⁹Y-CD45 (Fluidigm) for 30 min at 4 °C. Cells were then washed and pooled with PBMCs from the same individual.

Intracellular barcoding. After fixation and cryopreservation (at -80 °C), cells were thawed and subsequently stained with premade combinations of six different palladium isotopes: ¹⁰²Pd, ¹⁰⁴Pd, ¹⁰⁶Pd, ¹⁰⁸Pd, ¹⁰⁹Pd & ¹¹⁰Pd (Cell-ID 20-plex Pd Barcoding Kit, Fluidigm). This multiplexing kit applies a 6-choose-3 barcoding scheme that results in 20 different combinations of three Pd isotopes. After 30 min staining (at RT), individual samples were washed twice with cell staining buffer (0.5% bovine serum albumin in PBS, containing 2 mM EDTA). Total of up to 20 samples were pooled together, washed and further stained with antibodies.

Antibodies. Anti-human antibodies (Supplementary Table 2-7) were purchased either pre-conjugated to metal isotopes (Fluidigm) or from commercial suppliers in purified form and conjugated in house using the MaxPar X8 kit (Fluidigm) according to the manufacturer's protocol.

Surface and intracellular staining

After cell barcoding, washing and pelleting, the combined samples were resuspended in 100 μl of antibody cocktail against surface markers (Supplementary Table 2-7) and incubated for 30 min at 4 °C. Then, cells were washed twice with cell staining buffer. For intracellular staining, the stained (non-stimulated) cells were then incubated in fixation/permeabilization buffer (Fix/Perm Buffer, eBioscience) for 60 min at 4 °C. Cells were then washed twice with permeabilization buffer (eBioscience). The samples were then stained with antibody cocktails against intracellular molecules (Supplementary Table 2-7) in permeabilization buffer for 1 h at 4 °C. Cells were subsequently washed once with permeabilization buffer, then were washed again with PBS before overnight incubation in 2% methanol-free formaldehyde

solution (FA). Fixed cells were then washed and resuspended in 1 ml of 500 nM iridium intercalator solution (Fluidigm) for 1 h at RT. Next, the samples were washed twice with cell staining buffer and then twice with ddH₂O (Fluidigm). Cells were pelleted and kept at 4 °C until CyTOF measurement.

Mass cytometry data processing and analysis

As described previously^{22,26,27}, Cytobank (www.cytobank.org) was used for initial manual gating on single cells and boolean gating for debarcoding. Nucleated single intact cells were manually gated according to DNA intercalators ¹⁹¹Ir/¹⁹³Ir signals and event length. For debarcoding, Boolean gating was used to deconvolute individual sample according to the barcode combination. All de-barcoded samples were then exported as individual FCS files for further analysis. Each FCS file was compensated for signal spillover using the R package CATALYST⁵² and transformed with arcsinh transformation (scale factor 5) prior to data analysis. For further analysis we used a previously described scripts and workflows²⁵. Only samples with >50 cells were considered for the downstream data analysis. For a first assessment of the data we obtained multi-dimensional scaling (MDS) plots based on median marker expression from all markers in order to assess overall similarities between samples and/or groups/conditions. We next obtained a marker ranking identified by the PCA-based non-redundancy score (NRS) which can give us an idea of which markers explain most of the variability among samples. For following analysis, we selected the ten highest scoring NRS markers plus other lineage markers not included among this, and defined them as "TYPE" makers, thus the ones which will be used for unsupervised clustering. The rest of the markers were defined as "STATE" markers, which will be used to better describe the different populations and further assess differences in cell activation status between groups. Unsupervised clustering was performed using the FlowSOM²⁵/ConsensusClusterPlus²⁹ algorithms which are included in the CATALYST package. We then selected the number of meta-clusters used for further analysis based on the delta area plots (which assess the "natural" number of clusters that best fits the complexity of the data) together with visual inspection on the phenotypic heatmaps with an aim to select a cluster number with consistent phenotypes that would also allow us to explore small populations. For dimensionality-reduction visualization we generated UMAP representations using all markers as input and down-sampled to a maximum of 1000 cells per sample.

Cell culture and stimulation

PBMCs were resuspended in 1 ml of RPMI1640 (Biochrom GmbH, Berlin, Germany) containing 10% heat-inactivated foetal calf serum (FCS) (Sigma-Aldrich, St. Louis, USA), penicillin (100 U/mL; Biochrom GmbH, Berlin, Germany) and streptomycin (100 $\mu\text{g}/\text{mL}$; Biochrom GmbH, Berlin, Germany). Cell concentration was adjusted to $\sim 2 \times 10^6$ cells/mL. About 2×10^5 cells (per well) were transferred into ultra-low-attachment 96-well plate (Corning, New York, USA). Cells were treated with either PBS, CSF (20% v/v), IL-8 (50 ng/ml), MIP-1 α (10 ng/ml), LPS (100 ng/mL) or both CSF and LPS. To inhibit protein transport from Golgi apparatus to the endoplasmic reticulum, monensin (5 $\mu\text{g}/\text{mL}$; BioLegend, San Diego, USA) was also added. After 4–6 h incubation, cells were harvested, fixed and stored at -80 °C until CyTOF analysis.

Flow cytometry analysis

Cryopreserved and fixed PBMCs (4x CON, 4x MCI and 4x AD) were thawed and washed twice in staining buffer (PBS containing 0.5% BSA and 2 mM EDTA). The cells were incubated in Fc Block for 10 min at 4 °C. Cells were then stained for CD14 (PerCP-Cy5.5, clone HCD14), HLA-DR (APC-Cy7, clone L243), CX3CR1 (FITC, clone 2A9-1) and P2Y₁₂-Biotin for 20 min at 4 °C in staining buffer. Cells were washed once in staining buffer and then incubated in PE-Cy7-Streptavidin for 20 min at 4 °C. For the intracellular staining, the samples were washed once with

Article

<https://doi.org/10.1038/s41467-022-34719-2>

staining buffer, then fixed in 2% FA for 30 min at 4 °C. After incubation, the samples were washed with permeabilization buffer (eBioscience), and subsequently stained with IL-8 (PE, clone E8N1), MIP-1 α (APC, clone CCL3) and TNF (BV421, clone Mab11) for 30 min at 4 °C in permeabilization buffer. Stained cells were subsequently washed once with staining buffer. Cellular fluorescence was assessed with Cantoll (BD FACSDiva Software 6.1.3; BD Biosciences) and data were analyzed with FlowJo software (10.4.2) (TreeStar) and GraphPad Prism 9. Forward- and side-scatter parameters were used for exclusion of doublets from analysis (Supplementary Fig. 4).

Luminex

Cytokine levels in plasma and CSF were measured using cytokine protein multiplex assay (MILLIPEX[®] Multiplex Assays, Merck KGaA) on a Luminex 200 platform and Bio-Plex Manager 6.2 software (Bio-Rad Laboratories GmbH) according to the manufacturer's instructions. Plasma and CSF samples ($n=117$) of control individuals ($n=21$) or patients with AD ($n=18$), MCI ($n=7$), HD ($n=46$), depression ($n=11$), FTLD ($n=5$) and SCZ ($n=9$) were used for Luminex analysis (Supplementary Table 1).

Monocyte isolation and 1,2-¹³C₂-glucose experiment

Frozen human peripheral blood mononuclear cells (PBMCs) were thawed, washed and pooled in MACS buffer (0.5% BSA in PBS containing 2 mM EDTA). Monocytes were isolated using negative selection, pan-monocyte Isolation Kit (Miltenyi Biotec, Bergisch Gladbach, Germany) according to manufacturer's specifications. Briefly, PBMCs were resuspended in MACS buffer. FcR blocking reagent and biotin-antibody cocktail were added, mixed thoroughly and incubated at 4 °C. After 5 min incubation, MACS buffer and anti-biotin micro beads were added and incubated at 4 °C for 10 min. Stained cells were then washed with MACS buffer and pelleted (4 °C, 300 \times g, 8 min). The pellet was then resuspended in MACS buffer and loaded onto the MACS column. The column was then washed twice with MACS buffer. The flow-through and washed fraction containing unlabelled monocytes was collected. Cell number and viability were determined by 0.2% trypan blue staining. Monocytes were cultured and stimulated in the presence of 1,2-¹³C₂-glucose using the protocol described above. Cells were then harvested, pelleted and shock-frozen in liquid nitrogen. A 100 μ l of a mixture of acetonitrile and water (H₂O:ACN (1:1)) was then added to the frozen pellet and incubated on ice for 5 min. Cell lysate was then centrifuged at 15,000 \times g for 10 min (4 °C). A 75 μ l of supernatant was stored at -80 °C until HPLC-MS/MS analysis.

HPLC-MS/MS

Cell lysate in H₂O:ACN (1:1, as described above) was thawed and measured by HPLC-MS/MS. To reduce the chelating interactions between citrate or phosphates, and a broadening of the chromatographic peaks, which is caused by the metallic part of the instrument, the passivation of the system was performed prior to the analysis of targeted metabolites with HPLC-MS/MS. To do so, the whole system was washed with 0.5% H₃PO₄ in ACN:H₂O (9:1) overnight, followed by 1 hr of H₂O and 2 hr of column conditioning with the chosen mobile phases (*mobile phase A*: 10 mM CH₃COONH₄, pH 9 in H₂O with 5 μ M Agilent InfinityLab deactivator additive; *mobile phase B*: 10 mM CH₃COONH₄ (aq.) pH 9 in ACN with 5 μ M Agilent InfinityLab deactivator additive). Both mobile phases were filtered before use with a 0.2 μ m filter.

The analysis was conducted with an Agilent 1290 Infinity II HPLC system, coupled with an Agilent 6495 QqQ mass spectrometer, with an Agilent jet stream source with electrospray ionization (AJS-ESI). *Method*: dynamic multiple reaction monitoring (dMRM). *Ionization mode*: positive and negative. *Sheath gas flow*: 12 L/min for both, positive

and negative modes. *Sheath gas temperature*: 350 °C for both, positive and negative modes. *Capillary*: 4500 V for positive mode and 3500 V for negative. *Nozzle voltage*: 750 V for positive mode and 0 V for negative. *Drying gas temperature*: 210 °C for both, positive and negative modes. *Drying gas flow*: 20 L/min for both, positive and negative modes. *Nebulizer* 30 psi for both, positive and negative modes. *Funnel*: High P RF 190 and Low P RF 40 for positive mode and High P RF 110 and Low P RF 60 for negative. *Acquisition software*: MassHunter 10 Acquisition software G3335 (Agilent Technology, Waldbronn, Germany).

The chromatographic separation was performed with an Agilent Poroshell 120 HILIC-Z peek-lined column, at 30 °C, and with a gradient starting from 90% B to 60% B in 10 min and a total run time of 21 min. The autosampler was kept at 4 °C to preserve the samples and the injection volume was 1 μ L. The MS parameters and the targeted transitions were optimized and analysed with the Agilent MassHunter Optimizer software (MassHunter 10 Acquisition software G3335, Agilent Technology), and the chosen acquisition mode was dMRM to increase the sensitivity. An external calibration curve of standards in H₂O:ACN (1:1) with at least 8 levels was injected before the analysis of the samples as well as QCs every 10–15 injections to evaluate the stability of the system during the analysis. The method was validated based on the ICH guideline M10 on bioanalytical method validation. The quantitation was performed by external calibration of standards in H₂O:ACN (1:1), as mentioned above. We evaluated the specificity and the selectivity, the matrix effect and the recovery in peripheral blood mononuclear cells (PBMCs), the accuracy and the precision, the carry-over, and the short- and long-term stability. The detailed procedure of ¹³C₂-glucose tracing experiment and HPLC-MS/MS quantification was recently published and freely available³³.

Statistics and reproducibility

No randomization and blinding strategies were applied in this study. However, data processing and analysis, as well as statistical testing were carried out in an unsupervised manner. Quantitative data are shown as independent data points with median or Box-Whisker-Plot. Differential analysis of cell population abundance between groups were performed using EdgeR³⁴ available through the R package diffcyt³⁵ (with default parameters, and filtering parameters set to minimum number of cells = 3 in at least minimum number of samples = number of samples in each group) and false discovery rate (FDR) adjustment (at 5% using Benjamini-Hochberg procedure) for multiple hypothesis testing. Unless otherwise stated, significant differences in marker expression between clusters or between groups were calculated using Mann-Whitney *U*-test (5% FDR) in GraphPad Prism (version 9).

Reporting summary

Further information on research design is available in the Nature Portfolio Reporting Summary linked to this article.

Data availability

The CyTOF data generated in this study have been deposited in the FlowRepository database under accession code FR-FCM-Z5XD. The HPLC-MS/MS data generated in this study have been deposited in the refubium database (<https://refubium.fu-berlin.de>) under accession link <https://doi.org/10.17169/refubium-36351>. Source data are provided with this paper as Source Data file. Source data are provided with this paper.

Code availability

Codes used for CyTOF data analysis in this study are previously published by Crowell H et al. 2022 and available on <https://github.com/https://github.com/HelenaLC/CATALYST>.

Article

<https://doi.org/10.1038/s41467-022-34719-2>

References

- Hardy, J. & Selkoe, D. J. The amyloid hypothesis of Alzheimer's disease: progress and problems on the road to therapeutics. *Science* **297**, 353–356 (2002).
- Benilova, I., Karran, E. & De Strooper, B. The toxic A β oligomer and Alzheimer's disease: an emperor in need of clothes. *Nat. Neurosci.* **15**, 349–357 (2012).
- Carrillo, M. C. et al. Revisiting the framework of the National Institute on Aging-Alzheimer's Association diagnostic criteria. *Alzheimers Dement* **9**, 594–601 (2013).
- Dubois, B. et al. Advancing research diagnostic criteria for Alzheimer's disease: the IWG-2 criteria. *Lancet Neurol.* **13**, 614–629 (2014).
- Graeber, M. B. Neuroinflammation: no rose by any other name. *Brain Pathol.* **24**, 620–622 (2014).
- Prinz, M., Jung, S. & Priller, J. Microglia biology: one century of evolving concepts. *Cell* **179**, 292–311 (2019).
- Angel, A., Volkman, R., Royal, T. G. & Offen, D. Caspase-6 knockout in the 5xFAD model of Alzheimer's disease reveals favorable outcome on memory and neurological hallmarks. *Int. J. Mol. Sci.* **21**, 1144 (2020).
- Azizi, G., Khannazer, N. & Mirshafiey, A. The potential role of chemokines in Alzheimer's disease pathogenesis. *Am. J. Alzheimer's Dis. Other Dement.* **29**, 415–425 (2014).
- Ott, B. R. et al. Blood-cerebrospinal fluid barrier gradients in mild cognitive impairment and Alzheimer's disease: relationship to inflammatory cytokines and chemokines. *Front. Aging Neurosci.* **10**, 245 (2018).
- Heneka, M. T. et al. Neuroinflammation in Alzheimer's disease. *Lancet Neurol.* **14**, 388–405 (2015).
- Gate, D. et al. Clonally expanded CD8 T cells patrol the cerebrospinal fluid in Alzheimer's disease. *Nature* **577**, 399–404 (2020).
- Sudduth, T. L., Schmitt, F. A., Nelson, P. T. & Wilcock, D. M. Neuroinflammation phenotype in early Alzheimer's disease. *Neurobiol. Aging* **34**, 1051–1059 (2013).
- Zhang, B. et al. Integrated systems approach identifies genetic nodes and networks in late-onset Alzheimer's disease. *Cell* **153**, 707–720 (2013).
- Ising, C. et al. NLRP3 inflammasome activation drives tau pathology. *Nature* **575**, 669–673 (2019).
- Gold, M. & El Khoury, J. β -amyloid, microglia, and the inflammasome in Alzheimer's disease. *Semin Immunopathol.* **37**, 607–611 (2015).
- Mildner, A. et al. Distinct and non-redundant roles of microglia and myeloid subsets in mouse models of Alzheimer's disease. *J. Neurosci.* **31**, 11159–11171 (2011).
- Hawkes, C. A. & McLaurin, J. Selective targeting of perivascular macrophages for clearance of beta-amyloid in cerebral amyloid angiopathy. *Proc. Natl Acad. Sci. USA* **106**, 1261–1266 (2009).
- Zaghi, J. et al. Alzheimer disease macrophages shuttle amyloid-beta from neurons to vessels, contributing to amyloid angiopathy. *Acta Neuropathol.* **117**, 111–124 (2009).
- Wang, Y. et al. TREM2-mediated early microglial response limits diffusion and toxicity of amyloid plaques. *J. Exp. Med.* **213**, 667–675 (2016).
- Bradshaw, E. M. et al. CD33 Alzheimer's disease locus: altered monocyte function and amyloid biology. *Nat. Neurosci.* **16**, 848–850 (2013).
- Raj, T. et al. Polarization of the effects of autoimmune and neurodegenerative risk alleles in leukocytes. *Science* **344**, 519–523 (2014).
- Böttcher, C. et al. Human microglia regional heterogeneity and phenotypes determined by multiplexed single-cell mass cytometry. *Nat. Neurosci.* **22**, 78–90 (2019).
- Gosselin, D. et al. An environment-dependent transcriptional network specifies human microglia identity. *Science* **356**, eaal3222 (2017).
- Phongprecha, T. et al. Single-cell peripheral immunoprofiling of Alzheimer's and Parkinson's diseases. *Sci. Adv.* **6**, eabd5575 (2020).
- Nowicka, M. et al. CyTOF workflow: differential discovery in high-throughput high-dimensional cytometry datasets [version 4; peer review: 2 approved]. *F1000Research*. **6**, 748 (2019).
- Böttcher, C. et al. Single-cell mass cytometry reveals complex myeloid cell composition in active lesions of progressive multiple sclerosis. *Acta Neuropathol. Commun.* **8**, 136 (2020).
- Böttcher, C. et al. Multi-parameter immune profiling of peripheral blood mononuclear cells by multiplexed single-cell mass cytometry in patients with early multiple sclerosis. *Sci. Rep.* **9**, 19471 (2019).
- Van Gassen, S. et al. FlowSOM: Using self-organizing maps for visualization and interpretation of cytometry data. *Cytom. Part A* **87**, 636–645 (2015).
- Wilkerson, D. M. & Hayes, N. D. ConsensusClusterPlus: a class discovery tool with confidence assessments and item tracking. *Bioinformatics* **26**, 1572–1573 (2010).
- Farhadian, S. F. et al. Single-cell RNA sequencing reveals microglia-like cells in cerebrospinal fluid during virologically suppressed HIV. *Jci. Insight* **3**, e121718 (2018).
- Esaulova, E. et al. Single-cell RNA-seq analysis of human CSF microglia and myeloid cells in neuroinflammation. *Neuro. Neuroimmunol. Neuroinflamm.* **7**, e732 (2020).
- Russell, D. G. et al. Immunometabolism at the interface between macrophages and pathogens. *Nat. Rev. Immunol.* **19**, 291–304 (2019).
- Wolfe, H. et al. Monocytes exposed to plasma from patients with Alzheimer's disease undergo metabolic reprogramming. *Neurosci. Res.* **148**, 54–60 (2019).
- Khonrit, P. et al. Immune modulatory effect of a novel 4,5-dihydroxy-3,3',4'-trimethoxybibenzyl from *Dendrobium lindleyi*. *Plos One*. **15**, e0238509 (2020).
- Van Hove, H. et al. A single-cell atlas of mouse brain macrophages reveals unique transcriptional identities shaped by ontogeny and tissue environment. *Nat. Neurosci.* **22**, 1021–1035 (2019).
- Prinz, M. & Priller, J. Microglia and brain macrophages in the molecular age: from origin to neuropsychiatric disease. *Nat. Rev. Neurosci.* **15**, 300–312 (2014).
- Mattiola, I. et al. The macrophage tetraspan MS4A4A enhances dectin-1-dependent NK cell-mediated resistance to metastasis. *Nat. Immunol.* **20**, 1012–1022 (2019).
- Ostendorf, L. et al. SIGLEC1 (CD169): a marker of active neuroinflammation in the brain but not in the blood of multiple sclerosis patients. *Sci. Rep.* **11**, 10299 (2021).
- Piccio, L. et al. Cerebrospinal fluid soluble TREM2 is higher in Alzheimer disease and associated with mutation status. *Acta Neuropathol.* **131**, 925–933 (2016).
- Piccio, L. et al. Identification of soluble TREM-2 in the cerebrospinal fluid and its association with multiple sclerosis and CNS inflammation. *Brain* **131**, 3081–3091 (2008).
- Deming, Y. et al. The MS4A gene cluster is a key modulator of soluble TREM2 and Alzheimer disease risk. *Sci. Trans. Med.* **11**, 505 (2019).
- Griciuc, A. et al. TREM2 acts downstream of CD33 in modulating microglial pathology in Alzheimer's disease. *Neuron*. **103**, 820–835.e7 (2019).
- Muniz, V. S. et al. Purinergic P2Y12 receptor activation in eosinophils and the schistosomal host response. *Plos One* **10**, e0139805 (2015).
- Cattaneo, M. P2Y₁₂ receptors: structure and function. *J. Thromb. Haemost.* **13**, S10–S16 (2015).

Article

<https://doi.org/10.1038/s41467-022-34719-2>

45. Grassivaro, F. et al. Convergence between microglia and peripheral macrophages phenotype during development and neuroinflammation. *J. Neurosci.* **40**, 784–795 (2020).
46. Mildner, A. et al. P2Y₁₂ receptor is expressed on human microglia under physiological conditions throughout development and is sensitive to neuroinflammatory diseases. *Glia* **65**, 375–387 (2017).
47. Abbott, N. J. et al. The role of brain barriers in fluid movement in the CNS: is there a “glymphatic” system? *Acta Neuropathol.* **135**, 387–407 (2018).
48. Louveau, A. et al. Revisiting the mechanisms of CNS immune privilege. *Trends Immunol.* **36**, 569–577 (2015).
49. Baruch, K. & Schwartz, M. CNS-specific T cells shape brain function via the choroid plexus. *Brain Behav. Immun.* **34**, 11–16 (2013).
50. Streit, W. J. et al. Dystrophic microglia in late-onset Alzheimer’s disease. *Glia* **68**, 845–854 (2020).
51. Gate, D. et al. Clonally expanded CD8 T cells patrol the cerebrospinal fluid in Alzheimer’s disease. *Nature* **577**, 399–404 (2020).
52. Chevrier, S. et al. Compensation of signal spillover in suspension and imaging mass cytometry. *Cell Syst.* **6**, 612–620.e5 (2018).
53. Giacomello, G., Böttcher, C. & Parr, M. Isotopic tracing of glucose metabolites in human monocytes to access changes in inflammatory conditions. *STAR Protoc.* **3**, 101715 (2022).
54. Robinson, M. D., McCarthy, D. J. & Smyth, G. K. edgeR: a Bioconductor package for differential expression analysis of digital gene expression data. *Bioinformatics* **26**, 139–140 (2010).
55. Weber, L. M., Nowicka, M., Soneson, C. & Robinson, M. D. diffcyt: Differential discovery in high-dimensional cytometry via high-resolution clustering. *Commun. Biol.* **2**, 183 (2019).

Acknowledgements

We thank Jasmin Jamal El-Din and Christian Böttcher for excellent technical assistance with sample collection and ex vivo experiments. We would also like to acknowledge the assistance of the Flow & Mass Cytometry Core Facility (BIH at Charité—Universitätsmedizin Berlin, Germany) and the Netherlands Brain Bank (Amsterdam, The Netherlands). G.Gi. was funded by the Elsa-Neumann scholarship of the State of Berlin. G.Gi. and G.Ga. received the PhD scholarship from the NeuroMac School (DFG, the German Research Foundation—Project-ID 259373024—CRC/TRR 167 (B05)). A.M. and C.D. were funded by the Deutsche Forschungsgemeinschaft (DFG, the German Research Foundation—Project-ID 259373024—CRC/TRR 167 (B12)), and the Leducq Foundation (19CVD01). R.E.v.D., J.M. and E.M.H. were funded by ZonMW 733050107. C.B. and J.P. were funded by the Deutsche Forschungsgemeinschaft (DFG, the German Research Foundation—Project-ID 259373024—CRC/TRR 167 (B05 and B07)).

Author contributions

C.B. and J.P. conceived and designed the project. C.B., C.F.Z. and D.K. designed the antibody panels for mass cytometry. G.Gi. and M.K.P. performed the metabolomic tracing experiments using ¹³C-labelled

glucose. E.J.S. and J.P. recruited the patients and provided peripheral blood and cerebrospinal fluid samples, as well as the patients’ clinical data. J.M., R.E.v.D. and E.M.H. performed single-cell isolation, sorting and cryopreservation of the immune cells from post-mortem brain tissues. C.B., C.F.Z., G.Ga., J.K.H.L. and S.S. analyzed and interpreted the data. A.D. and G.Gi. performed the ex vivo experiment. A.D., C.D. and A.M. were responsible for Luminex analysis. C.B., C.F.Z., S.S., F.P. and J.P. wrote the manuscript.

Funding

Open Access funding enabled and organized by Projekt DEAL.

Competing interests

The authors declare no competing interests.

Additional information

Supplementary information The online version contains supplementary material available at <https://doi.org/10.1038/s41467-022-34719-2>.

Correspondence and requests for materials should be addressed to Josef Priller or Chotima Böttcher.

Peer review information *Nature Communications* thanks Ben Korin, Priyanka Baloni and the other, anonymous, reviewer(s) for their contribution to the peer review of this work. Peer reviewer reports are available.

Reprints and permissions information is available at <http://www.nature.com/reprints>

Publisher’s note Springer Nature remains neutral with regard to jurisdictional claims in published maps and institutional affiliations.

Open Access This article is licensed under a Creative Commons Attribution 4.0 International License, which permits use, sharing, adaptation, distribution and reproduction in any medium or format, as long as you give appropriate credit to the original author(s) and the source, provide a link to the Creative Commons license, and indicate if changes were made. The images or other third party material in this article are included in the article’s Creative Commons license, unless indicated otherwise in a credit line to the material. If material is not included in the article’s Creative Commons license and your intended use is not permitted by statutory regulation or exceeds the permitted use, you will need to obtain permission directly from the copyright holder. To view a copy of this license, visit <http://creativecommons.org/licenses/by/4.0/>.

© The Author(s) 2022

3.3 Manuscript III: “1,2-¹³C₂-Glucose Tracing Approach to Assess Metabolic Alterations of Human Monocytes under Neuroinflammatory Conditions”

Ginevra Giacomello, Carolin Otto, Josef Priller, Klemens Ruprecht, Chotima Böttcher, and Maria Kristina Parr

Current Issues in Molecular Biology; 45 (2023) 765–781

DOI: 10.3390/cimb45010051

Abstract: Neuroinflammation is one of the common features in most neurological diseases including multiple sclerosis (MScl) and neurodegenerative diseases such as Alzheimer’s disease (AD). It is associated with local brain inflammation, microglial activation, and infiltration of peripheral immune cells into cerebrospinal fluid (CSF) and the central nervous system (CNS). It has been shown that the diversity of phenotypic changes in monocytes in CSF relates to neuroinflammation. It remains to be investigated whether these phenotypic changes are associated with functional or metabolic alteration, which may give a hint to their function or changes in cell states, e.g., cell activation. In this article, we investigate whether major metabolic pathways of blood monocytes alter after exposure to CSF of healthy individuals or patients with AD or MScl. Our findings show a significant alteration of the metabolism of monocytes treated with CSF from patients and healthy donors, including higher production of citric acid and glutamine, suggesting a more active glycolysis and tricarboxylic acid (TCA) cycle and reduced production of glycine and serine. These alterations suggest metabolic reprogramming of monocytes, possibly related to the change of compartment (from blood to CSF)

and/or disease-related. Moreover, the levels of serine differ between AD and MScl, suggesting different phenotypic alterations between diseases.



Article

1,2-¹³C₂-Glucose Tracing Approach to Assess Metabolic Alterations of Human Monocytes under Neuroinflammatory Conditions

Ginevra Giacomello ^{1,*} , Carolin Otto ², Josef Priller ^{3,4,5,6}, Klemens Ruprecht ², Chotima Böttcher ^{3,7,8,†} and Maria Kristina Parr ^{1,*}

- ¹ Institute of Pharmacy, Freie Universität Berlin, Königin-Luise-Str. 2 + 4, 14195 Berlin, Germany
 - ² Department of Neurology, Charité—Universitätsmedizin Berlin, Corporate Member of Freie Universität Berlin and Humboldt-Universität zu Berlin, 10117 Berlin, Germany
 - ³ Department of Neuropsychiatry and Laboratory of Molecular Psychiatry, Charité—Universitätsmedizin Berlin, Corporate Member of Freie Universität Berlin and Humboldt-Universität zu Berlin, 10117 Berlin, Germany
 - ⁴ German Center for Neurodegenerative Diseases (DZNE), 10117 Berlin, Germany
 - ⁵ Department of Psychiatry and Psychotherapy, School of Medicine, Technical University Munich, 81675 Munich, Germany
 - ⁶ UK Dementia Research Institute (UK DRI), University of Edinburgh, Edinburgh EH16 4SB, UK
 - ⁷ Experimental and Clinical Research Center, a Cooperation between the Max Delbrück Center for Molecular Medicine in the Helmholtz Association and Charité—Universitätsmedizin Berlin, 13125 Berlin, Germany
 - ⁸ Max Delbrück Center for Molecular Medicine in the Helmholtz Association (MDC), 13125 Berlin, Germany
- * Correspondence: ginevra@zedat.fu-berlin.de (G.G.); maria.parr@fu-berlin.de (M.K.P.);
Tel.: +49-30-838-57686 (M.K.P.)
- † These authors contributed equally to this work.



Citation: Giacomello, G.; Otto, C.; Priller, J.; Ruprecht, K.; Böttcher, C.; Parr, M.K. 1,2-¹³C₂-Glucose Tracing Approach to Assess Metabolic Alterations of Human Monocytes under Neuroinflammatory Conditions. *Curr. Issues Mol. Biol.* **2023**, *45*, 765–781. <https://doi.org/10.3390/cimb45010051>

Academic Editors: Aij Lie Kwan and Hung-Pei Tsai

Received: 8 December 2022

Revised: 5 January 2023

Accepted: 8 January 2023

Published: 16 January 2023



Copyright: © 2023 by the authors. Licensee MDPI, Basel, Switzerland. This article is an open access article distributed under the terms and conditions of the Creative Commons Attribution (CC BY) license (<https://creativecommons.org/licenses/by/4.0/>).

Abstract: Neuroinflammation is one of the common features in most neurological diseases including multiple sclerosis (MS) and neurodegenerative diseases such as Alzheimer’s disease (AD). It is associated with local brain inflammation, microglial activation, and infiltration of peripheral immune cells into cerebrospinal fluid (CSF) and the central nervous system (CNS). It has been shown that the diversity of phenotypic changes in monocytes in CSF relates to neuroinflammation. It remains to be investigated whether these phenotypic changes are associated with functional or metabolic alteration, which may give a hint to their function or changes in cell states, e.g., cell activation. In this article, we investigate whether major metabolic pathways of blood monocytes alter after exposure to CSF of healthy individuals or patients with AD or MS. Our findings show a significant alteration of the metabolism of monocytes treated with CSF from patients and healthy donors, including higher production of citric acid and glutamine, suggesting a more active glycolysis and tricarboxylic acid (TCA) cycle and reduced production of glycine and serine. These alterations suggest metabolic reprogramming of monocytes, possibly related to the change of compartment (from blood to CSF) and/or disease-related. Moreover, the levels of serine differ between AD and MS, suggesting different phenotypic alterations between diseases.

Keywords: monocytes; metabolism; cerebrospinal fluid; glycolysis; tricarboxylic acid cycle; multiple sclerosis; Alzheimer; metabolites; neuroinflammation

1. Introduction

Neurodegenerative and inflammatory diseases such as Alzheimer’s disease (AD) and multiple sclerosis (MS) are continuously gaining focus from the scientific and public audience due to the high incidence and devastating consequences in terms of life quality and care-need of patients. Although the course, symptoms, causes, and characteristics of these neurological diseases are highly heterogeneous, some aspects are in common, i.e., the presence of neuroinflammatory features. Both diseases are characterized by microglial

activation [1–4], increased production of pro- and anti-inflammatory cytokines [5–8], and infiltration of peripheral immune cells from the bloodstream into the cerebrospinal fluid (CSF) due to the impairment of the blood–CSF barrier [9–12]. However, it remains largely unknown to what extent changing the compartment environment (e.g., from blood to CSF) influences the phenotypes and functions of this myeloid cell population. Previous studies demonstrated the phenotypic diversity of CSF infiltrating monocytes [13–17], but little is known about related changes in functions and/or changes in the metabolism of these cells compared to their counterparts in the peripheral blood. Changes in metabolism, e.g., glucose metabolism, can give a hint on cell activation and/or responses to pathology [18–20].

One of the hypotheses is that once the monocytes enter the CSF through the choroid plexus (CP), they undergo phenotypic changes and take part in the inflammatory response to eventually help the resolution of the innate inflammation [21,22]. The first reaction is to contribute to neuroinflammation to regulate adaptive immunity. Why, in chronic neuroinflammation such as AD or MScl, the resolution of the inflammation does not happen and causes neuronal damage needs to be further investigated. Similarly, whether this is caused by the aggravated impairment of the barrier between CSF and blood, by the disease, or is caused by both, needs additional investigation. Varvel et al. proposed as beneficial the inhibition of the entrance of monocytes into the brain to mitigate the inflammation occurring after seizures in status epilepticus [23], but since the function of myeloid cells, in normal conditions, is also to remove waste products (β -amyloid included), a pathologic environment may also play a role in it. Many studies have focused lately on recruited myeloid cells to better understand their role in acute or chronic neuroinflammation, and to evaluate the changes that they undergo once they change the compartment.

To have a more complete overview of the changes that CSF-infiltrating monocytes undergo, it is necessary to also consider immunometabolism and its alterations. Lately, it has been pointed out as fundamental in the regulation between pro- and anti-inflammatory profiles [24]. The metabolism of cells is reported to regulate energetic production, intracellular signaling, the well-being of the cells, and the synthesis of amino acids and other metabolites. Furthermore, glycolysis is an essential metabolic pathway for the differentiation of macrophages [25] and the activation of immune cells during inflammation [24]. To study phenotypic and metabolic changes in circulating immune cells under different conditions including experimental settings, several state-of-the-art technologies can be used such as mass cytometry (CyTOF) [26–29], cell bioenergetic analysis (Seahorse) [30–33], multiplex immunoassay (Luminex) [28,34,35], nuclear magnetic resonance (NMR) [36–38], high-performance liquid chromatography (HPLC), or gas chromatography (GC) hyphenated with mass spectrometry (MS) or tandem mass spectrometry (MS/MS) [39–42]. In-depth characterization of the metabolic pathway is achieved using HPLC- or GC-MS(/MS). The use of stable isotopic tracing methods (e.g., ^{13}C -glucose tracing) increases confidence in identifying the metabolites affected by the study conditions or experimental manipulations.

In our previous study [21], we characterized the phenotypic alterations of infiltrating myeloid cells in the CSF of healthy individuals and patients with neurological disorders such as AD, mild cognitive impairment (MCI), and Huntington's disease. Our findings suggested activation and inflammatory response of myeloid cells as well as metabolic changes after exposure to CSF, with a slightly increased phenotypic alteration in the case of AD-CSF [21]. Using Seahorse assays, we evaluated the extracellular acidification rate (ECAR), a value linked to glycolysis, and the oxygen consumption rate (OCR), connected to cell respiration, of myeloid cells in different conditions: without stimulation or with the stimulation of CSF of healthy donors or patients with AD or MCI. The results showed an increased ECAR when the cells were incubated in the presence of CSF [21,43]. It is tempting to speculate that, with higher intensity of neuroinflammatory conditions such as in MScl, strong changes in phenotypes and metabolism will be detectable, which can possibly be a drawback to functional changes in these cells in CSF.

We also showed, using the previously validated $1,2\text{-}^{13}\text{C}_2$ -glucose tracing experiment [44], how the presence of CSF of AD patients in the incubation of monocytes could cause

a decrease in the conversion of ^{13}C pyruvate to ^{13}C lactate and a reduced production of serine [21].

In this study, we aim to comparably evaluate the overall metabolism of monocytes in CON and AD individuals in comparison to MScl with more pronounced neuroinflammation. We performed a $1,2\text{-}^{13}\text{C}_2$ glucose tracing experiment on monocytes targeting key-role metabolites of the major metabolic pathways of the cell (glycolysis, pentose-5-phosphate pathway, serine and glycine production, tricarboxylic acid (TCA) cycle, lactate production from pyruvate, and glutamine/glutamic acid metabolism). Intracellular and secreted unlabeled and ^{13}C glucose-derived metabolites were identified and quantified using HPLC-MS/MS. In this study, we identified the rewiring of the glucose metabolism of monocytes after CSF treatment, and the differential metabolic alterations in neuroinflammatory conditions such as MScl (MScl-CSF treatment) in comparison with neurodegeneration conditions such as AD (AD-CSF treatment).

2. Materials and Methods

This study was registered and approved by the Ethics Commission of Charité—Universitätsmedizin Berlin (Ethikkommission der Charité—Universitätsmedizin Berlin; registration number EA1/187/17), Berlin, Germany.

2.1. Primary Human Monocyte Isolation and Incubation

PBMCs were obtained from the German Red Cross and stored at $-80\text{ }^\circ\text{C}$ until incubation. Monocytes were then isolated from PBMCs with MACS (Pan Monocyte Isolation Kit (human), Miltenyi Biotec, Bergisch Gladbach, Germany).

After isolation, monocytes were incubated in a 24-well/plate in four different conditions with three biological replicates for each group: medium only without stimulation ($3 \times \text{NS}$), with the addition of 30% in volume of CSF of healthy individuals ($3 \times \text{CON}$), with the addition of 30% in volume of CSF from AD patients ($3 \times \text{AD}$), and with the addition of 30% in volume of CSF of MScl patients ($3 \times \text{MScl}$). Before use, pH values of all CSF samples were measured. Only CSF with a pH of about 7 was used in this study.

The monocytes were incubated for 5 h at $37\text{ }^\circ\text{C}$, with 5% CO_2 , in a medium without glucose, pyruvate, glutamine, and phenol red (DMEM, Thermo Fisher Scientific, Inc., Waltham, MA, USA) added with labeled glucose (D-1,2- $^{13}\text{C}_2$ glucose, Sigma Aldrich, Taufkirchen, Germany) to a final concentration of 4.5 g/L, and with 10% FBS (heat-inactivated, Gibco™, NY, USA). As the incubation of monocytes in a medium without pyruvate, glutamine, and phenol red may be challenging, the well-being of the cells needs to be monitored with a microscope at regular time intervals.

Details of isolation and culture of monocytes are described elsewhere [44].

2.2. Metabolite Extraction and Sample Preparation

2.2.1. Culture Medium

After the incubation, the cell suspension was transferred to Eppendorf tubes and centrifuged for 10 min at $4\text{ }^\circ\text{C}$ at $300 \times g$. Then, the supernatant (cell-free culture medium, representing the secreted level of metabolites) was separated from the cell pellet and centrifuged at $15,000 \times g$, for 10 min at $4\text{ }^\circ\text{C}$ before the analysis with HPLC-MS/MS.

2.2.2. Cell Extract

After shock-freezing of the cell pellets using liquid nitrogen 100 μL of H_2O : acetonitrile (ACN) (1:1, *v:v*) were added for the extraction. After thorough vortexing and incubation on ice for 5 min, the samples were centrifuged at $15,000 \times g$ for 10 min at $4\text{ }^\circ\text{C}$. Aliquots of 75 μL of the supernatant without disturbing the cell remainder were used to obtain the cell extract (representing an intracellular level of metabolites). Samples were stored at $-80\text{ }^\circ\text{C}$ until the HPLC-MS/MS analysis.

Details of monocyte extraction and sample preparation are previously described in detail [44].

2.3. HPLC-MS/MS Setup and Analysis

The chromatographic conditions, the MS/MS parameters, and the dynamic multiple reaction monitoring (dMRM) method were optimized and validated. Details of the analytical method are reported previously [44].

Standard solutions for calibration levels and quality controls (QCs) were prepared in serial dilution from stock solution (1 mg/mL) in Milli-Q H₂O:ACN (1:1).

Analyses of samples, QC, and calibration levels were conducted with an Agilent 1290 Infinity II HPLC system coupled with an Agilent 6495 QqQ mass spectrometer (MS/MS) with an Agilent jet stream source with electrospray ionization (AJS-ESI), both controlled by MassHunter 10 Data Acquisition software (Agilent Technologies, Waldbronn, Germany). For the separation of the metabolites, an Agilent InfinityLab Poroshell 120 HILIC-Z column (PEEK-lined, 2.1 mm × 100 mm, 2.7 μm) was used. To optimize the chromatographic peak shape of citric acid and phosphates, passivation of the system was needed with an overnight wash of the system with 0.5% H₃PO₄ in ACN:H₂O (9:1). Mobile phase A was 10 mM CH₃COONH₄ in H₂O with the addition of InfinityLab deactivator additive (Agilent Technologies, Waldbronn, Germany). Mobile phase B was 10 mM CH₃COONH₄ in ACN with the addition of InfinityLab deactivator additive (Agilent Technologies). We added 1 mL of additive for 1 L of mobile phase. HPLC separation was achieved by running a linear gradient from 10% to 40% to 10% mobile phase A in 20 min. The optimized dynamic multiple reaction monitoring (dMRM) was conducted by applying both positive and negative ionization mode.

For further specifications on HPLC conditions, MS parameters, and mobile phase preparation, refer to Giacomello et al. [44].

2.4. Data Analysis

Chromatographic and spectrometric results were evaluated with MassHunter 10 Quantitative Analysis program G3336 (Agilent Technologies, Waldbronn, Germany). For graphical summaries, Prism 7 (GraphPad) was used.

For the statistical analysis, OriginPro 2021b (OriginLab) was used. Normal distribution and equality of variances were evaluated with Shapiro–Wilk test and Levene’s test, respectively. For the evaluation of the significant variation between groups, a one-way ANOVA was conducted for normally distributed groups and Kruskal–Wallis for those not normally distributed. To determine which group was significantly different, a Tukey’s test or a Dunn’s test (non-parametric) was conducted.

3. Results

Using our validated method [44], unlabeled pyruvate, lactate, glycine, glutamine, serine, glutamic acid, and citric acid, as well as 2,3-¹³C₂ pyruvate, 1,2-¹³C₂ lactate, 2-¹³C glycine, and 1,2-¹³C₂ glutamine produced by human primary monocytes, incubated in vitro without stimulation or with the addition of CSF of healthy donors or patients with AD or MScl, were successfully quantified. Of note, the concentrations of 2,3-¹³C₂ serine and 1,2-¹³C₂ citric acid were lower than the limit of quantitation (LOQ), and thus they were considered detectable but not quantified metabolites. This confirmed the integration and conversion of the supplemented 1,2-¹³C₂ glucose into the glucose metabolism of the primary monocytes. ATP, AMP, acetyl coenzyme A (AcCoA), fructose-6-phosphate, glyceraldehyde-3-phosphate, phosphoglyceric acid, and ribose-5-phosphate concentrations were below the limit of detection (LOD) under our in vitro experimental conditions. These results are summarized in Figure 1.

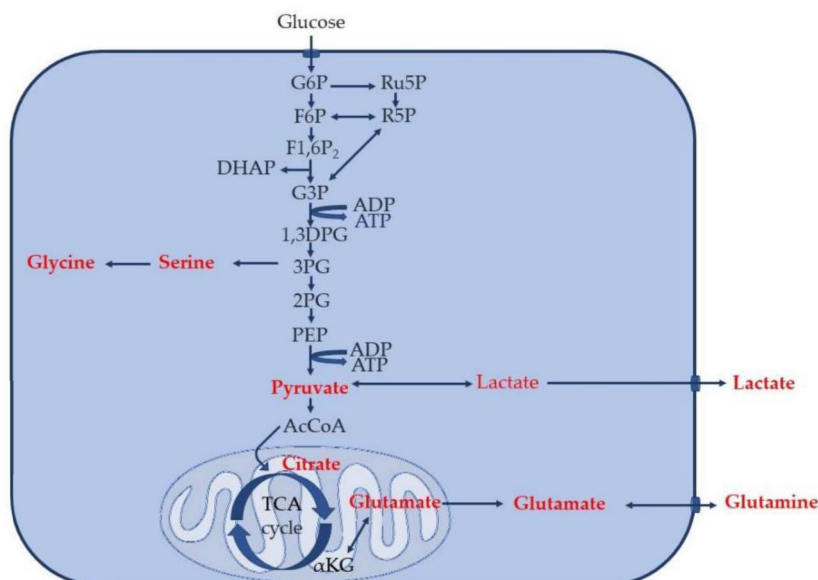


Figure 1. A common glucose metabolism in the cells. Metabolites that are detectable and quantifiable in this study are labeled in red (i.e., whose concentrations are at or higher than LOD and LOQ).

As common in HILIC separation [45–47] and as already reported previously [44], it is not possible to chromatographically separate and, therefore, unambiguously distinguish between citric and isocitric acid under our measurement conditions. Thus, hereafter citric acid refers to a mixture of the two isomers. The individual concentrations of all the analytes (labeled and unlabeled) that have been quantified in cell lysate and medium are summarized in Supplementary Table S1.

3.1. Increased Glucose Conversion in Monocytes after Exposure to CSF

As shown in Figure 2, increased intracellular concentrations of citric acid ($p = 0.0073$), glutamine ($p = 0.0004$), and pyruvate ($p = 0.0387$) were detected in monocytes after treatment with CSF (i.e., CON-, AD-, and MScI-CSF) in comparison to non-stimulated (NS) monocytes. In contrast, serine ($p = 0.0356$) and glycine ($p = 0.0166$) were quantified at a lower concentration compared to the NS group. These observations were partly confirmed with post hoc tests (Tukey's test for normally distributed and Dunn's test for non-normally distributed data), i.e., the concentrations of intracellular citric acid and glutamine were significantly increased in monocytes after exposure to CON-CSF, AD-CSF, and MScI-CSF in comparison with the NS group, whereas pyruvate concentration was significantly increased only in the CON-CSF-treated group compared with NS. Intracellular serine and glycine concentrations were finally significantly different only between AD-CSF-treated and MScI-CSF-treated monocytes, each compared to the NS group.

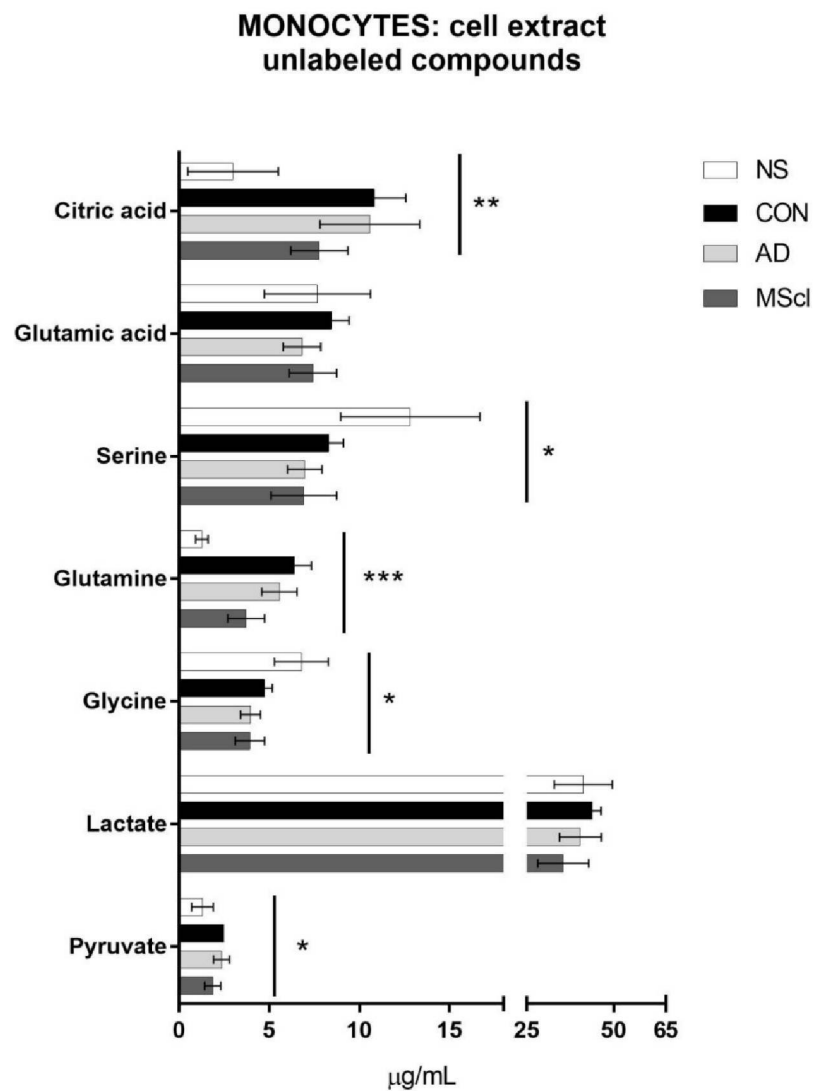


Figure 2. Concentrations of unlabeled analytes detected and quantified in the cell extract (intracellular amounts) of 8×10^5 monocytes/well, incubated for 5 h in four different conditions: non-stimulation (NS, 1), treatment with CSF from healthy donors (CON, 2), patients with AD (3), or MScl (4). The figure shows the p -values of all four groups obtained with one-way ANOVA for data normally distributed or Kruskal–Wallis test for data non-normally distributed (* $p \leq 0.05$; ** $p \leq 0.01$; *** $p \leq 0.001$). Tukey’s test or Dunn’s test (non-parametric) were performed as post hoc tests.

Similar to the unlabeled endogenous glucose metabolites, the majority of $1,2\text{-}^{13}\text{C}_2$ glucose-derived compounds were $2,3\text{-}^{13}\text{C}_2$ pyruvate and $1,2\text{-}^{13}\text{C}_2$ lactate. A small amount of ^{13}C -glutamine was quantified in CSF-treated monocytes ($>\text{LOQ}$), while its concentration was below LOQ in untreated monocytes (Figure 3).

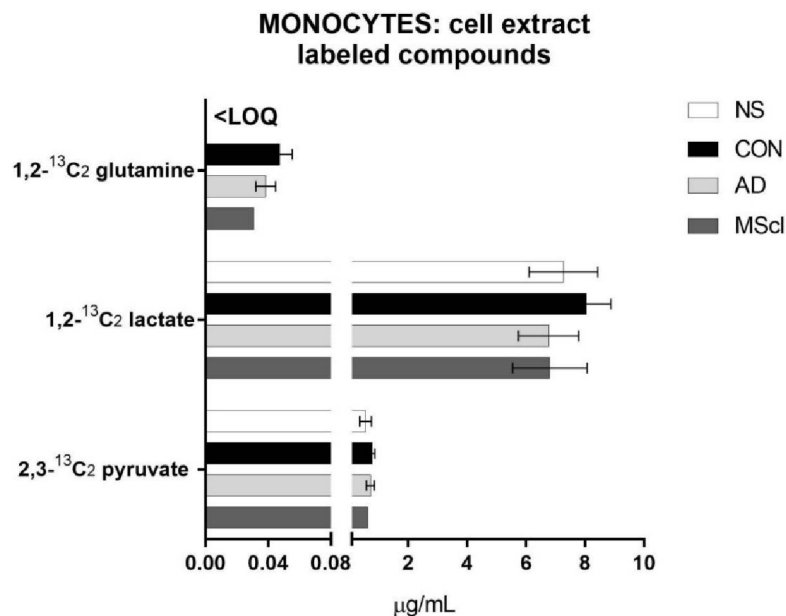


Figure 3. Incorporation of ¹³C starting from 1,2-¹³C₂ glucose into glucose-metabolites in the analytes quantified from the cell extract after 5 h of incubation of 8×10^5 monocytes/well. In this case, no significant differences were found between the treatment groups (one-way ANOVA for data normally distributed or Kruskal–Wallis test for data non-normally distributed), with an exception made for labeled glutamine that was not quantifiable in NS. <LOQ: the concentration of the analyte was less than the limit of quantitation.

3.2. Differential Concentration of Secreted Glucose-Derived Metabolites

Next, the same analysis was performed with the cultured medium to quantify glucose-derived metabolites that were secreted into the culture medium. This information gave an overview of the overall conversion of glucose as well as ¹³C-glucose into its metabolites under the applied experimental conditions. The concentrations of unlabeled and ¹³C-labeled metabolites are shown in Figures 4 and 5, respectively.

Similar to the results obtained from cellular fraction (i.e., intracellular metabolites), significant differences in the level of citric acid ($p = 3.2 \times 10^{-6}$), glutamine ($p = 9.0 \times 10^{-7}$), pyruvate ($p = 6.9 \times 10^{-5}$), serine ($p = 1.5 \times 10^{-10}$), and glycine ($p = 1.3 \times 10^{-6}$) were detected between the NS and the CSF-treatment groups (Table 1). Glutamic acid ($p = 4.6 \times 10^{-5}$) shows significant variations in concentrations only between NS and CSF of patients (AD and MScl). There are also some significant differences between CSF-treated groups. Lactate ($p = 0.0125$), serine, and glutamic acid displayed a significant variation between CON and AD, whereas lactate, glutamine, and glutamic acid differed between CON and MScl and glutamine, and serine between AD and MScl (Figure 4).

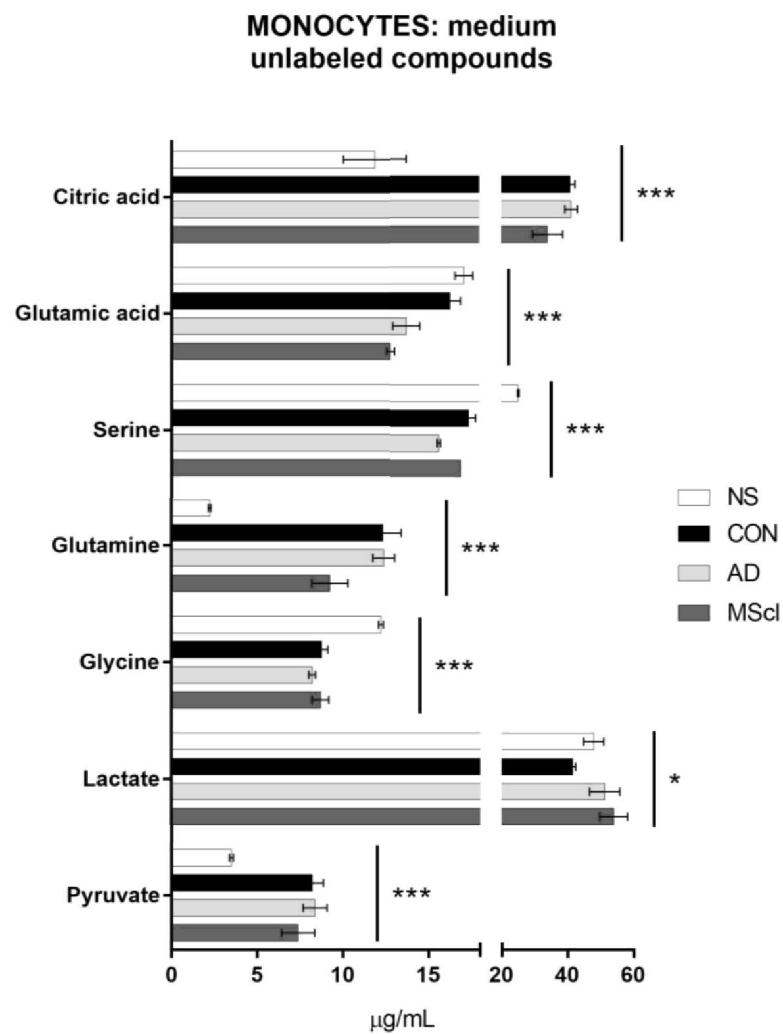


Figure 4. Concentrations of analytes detected and quantified in the culture medium (extracellular amounts) of 8×10^5 monocytes/well. The figure shows the p -values for all four groups obtained with one-way ANOVA for data normally distributed or Kruskal–Wallis test for data non-normally distributed ($* p \leq 0.05$; $*** p \leq 0.001$). Tukey's test or Dunn's test (non-parametric) were performed as post hoc tests.

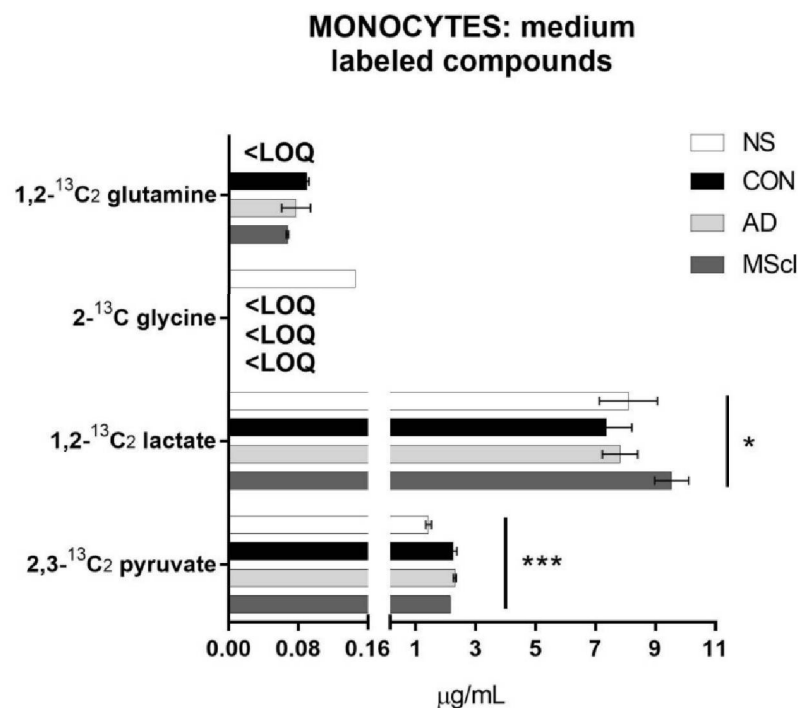


Figure 5. Incorporation of ¹³C starting from 1,2-¹³C₂ glucose into glucose-metabolites in the analytes quantified in the cell incubation medium after 5 h of incubation of 8×10^5 monocytes/well. In the figures are shown the *p*-values obtained with one-way ANOVA for data normally distributed or Kruskal–Wallis test for data non-normally distributed (* *p* ≤ 0.05; *** *p* ≤ 0.001). Tukey's test or Dunn's test (non-parametric) were performed as post hoc tests. <LOQ: the concentrations of the analytes were less than the limit of quantitation.

Determination of the incorporation of ¹³C from 1,2-¹³C₂ glucose revealed the majority was converted to pyruvate (2,3-¹³C₂ pyruvate) and lactate (1,2-¹³C₂ lactate), and only in small amounts to glutamine (1,2-¹³C₂ glutamine) and glycine (2-¹³C glycine), as shown in Figure 5. 2,3-¹³C₂ serine and 1,2-¹³C₂ citric acid were detected in all samples, but the concentrations were lower than LOQ, and thus they are not shown in Figure 5. Furthermore, 1,2-¹³C₂ glutamine could only be quantified in the monocytes treated with CSF and 2-¹³C glycine only in the NS group. Differential abundances of 2,3-¹³C₂ pyruvate and 1,2-¹³C₂ lactate were significantly increased in CSF-treated monocytes (*p*-values of 7.9×10^{-5} and 0.0318, respectively).

To summarize the significant differences between all groups, Table 1 reports the *p*-values obtained with the one-way ANOVA (for normally distributed) or the Kruskal–Wallis test (non-parametric) and the results of the Tukey's or Dunn's tests to establish the differences between each group.

Table 1. Significant differences between groups. The *p*-values were obtained with the one-way ANOVA test for normally distributed data or with the Kruskal–Wallis test for non-normally distributed data. The asterisks show which group was significantly different from the other. Results were obtained with post hoc tests (Tukey’s test for normally distributed and Dunn’s test for non-parametric).

Analyte	Cell Lysate						Incubation Medium							
	<i>p</i> -value	NS vs. CON	NS vs. AD	NS vs. MScl	CON vs. AD	CON vs. MScl	AD vs. MScl	<i>p</i> -value	NS vs. CON	NS vs. AD	NS vs. MScl	CON vs. AD	CON vs. MScl	AD vs. MScl
Pyruvate	0.0387	#						6.9×10^{-5}	#	#	#			
2,3- ¹³ C ₂ pyruvate	0.3611							7.9×10^{-5}	#	#	#			
Lactate	0.4955							0.0125				#	#	
1,2- ¹³ C ₂ lactate	0.3963							0.0318					#	
Glycine	0.0166		*	*				1.3×10^{-6}	*	*	*			
1,2- ¹³ C ₂ glutamine	0.2199							0.0665						
Glutamine	0.0004	#	#	#		*		9.0×10^{-7}	#	#	#		*	*
Serine	0.0356		*	*				1.5×10^{-10}	*	*	*	*		#
Glutamic acid	0.7333							4.6×10^{-5}		*	*	*	*	
Citric acid	0.0073	#	#					3.2×10^{-6}	#	#	#			

Significantly different with the post hoc tests. The first term of comparison is lower than the second. * Significantly different with the post hoc tests. The first term of comparison is higher than the second.

3.3. Endogenous Glucose-Derived Metabolites in CSF

We took into consideration that there are some naturally abundant metabolites in CSF, e.g., lactate, pyruvate, and glutamine. These compounds were also detected and quantified. In Figure 6, we compare these CSF-metabolites to the metabolites detected in monocytes and the medium after incubation. Here, we considered only glutamine, citric acid, lactate, and pyruvate, the metabolites that were significantly different between the groups as shown above. The total amounts of intracellular and secreted metabolites are much higher than those naturally present in CSF, confirming the metabolic activity of monocytes and the further production of these compounds (i.e., both unlabeled and ^{13}C -labeled) during the incubation. The concentration of glucose in CSF of healthy individuals or patients with AD or MScl is reported to be similar [48–51]. Moreover, the total concentrations of glucose (labeled and not labeled) during the incubation are quite similar between groups (i.e., NS, CON, AD, and MScl).

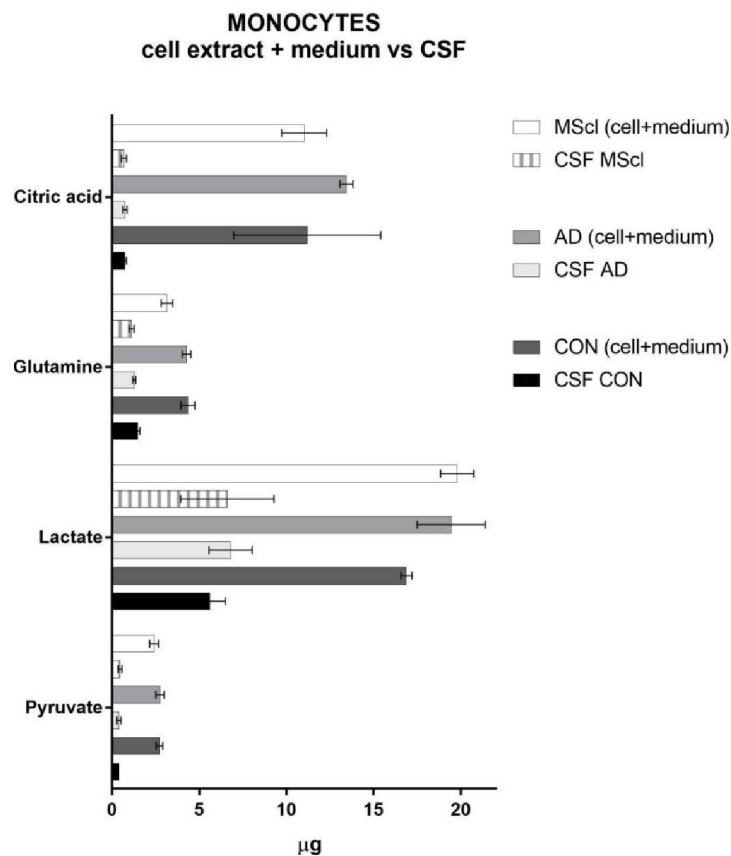


Figure 6. Comparison of the amounts of the endogenous metabolites detected in CSF with the sum of intra- and extracellular. CSF MScl: μg of analytes quantified in the CSF of MScl patients; MScl (cell + medium): sum of the μg of analytes quantified in the cell lysate and medium of monocytes incubated with MScl-CSF; CSF AD: μg of analytes quantified in the CSF of AD patients; AD (cell + medium): sum of the μg of analytes quantified in the cell lysate and medium of monocytes incubated with AD-CSF; CSF CON: μg of analytes quantified in the CSF of healthy donors. CON (cell + medium): sum of the μg of analytes quantified in the cell lysate and medium of monocytes incubated with CON-CSF. The values are the mean of three biological replicates \pm SD.

4. Discussion

The incorporation of ^{13}C from labeled glucose into its metabolites allows insights into the metabolic pathway that was preferentially taken during *in vitro* stimulation. Further to small amounts of the remaining endogenous glucose present in the monocytes or the CSF, the only source of glucose was 1,2- $^{13}\text{C}_2$ -glucose added to the glucose-free medium. Primary human monocytes isolated from the peripheral blood of healthy individuals were used in this study. The main limitation of our study was the number of monocytes obtained from a limited volume of the peripheral blood, which in turn resulted in low amounts of detected metabolites. However, the feasibility to apply this method to study changes in cellular metabolism (i.e., glucose) in a small sample of human primary cells was demonstrated. Although not all glucose-derived metabolites could be detected due to the limitation mentioned above, an increased level of both unlabeled and/or labeled citric acid, glutamine, and pyruvate in CSF-treated monocytes and in the culture medium was consistently detected, whereas serine and glycine were consistently reduced after treatment with CSF. Our findings suggest the rewiring of the glucose metabolic pathway in monocytes after treatment with CSF, possibly due to an increased cellular activation. Commonly, activation of human innate immunity requires alteration of cellular metabolic pathways largely to favor glucose metabolism [52–56].

The significant increase in the citric acid concentration, once monocytes came into contact with CSF no matter from which group, follows the increase in pyruvate mentioned above, suggesting a more active tricarboxylic acid (TCA) cycle as well. Due to the limited amount of labeled pyruvate, and the preferential pathway towards the formation of lactate, it is not a surprise that other labeled compounds of the TCA cycle were not quantifiable. Moreover, rate-limiting in the TCA cycle is the citrate synthase catalyzed step [44]. As labeled citric acid could be detected but not quantified ($>\text{LOD}$ but $<\text{LOQ}$), the analysis of other labeled metabolites of the TCA cycle is difficult. Furthermore, it must be considered that the TCA cycle will undergo multiple cycles within 5 h of incubation. Thus, it is reasonable to expect a fast interconversion and consumption of the other metabolic intermediates and a production of a variety of labeled metabolites. Since the aim of this study was to gain an overview of the metabolic trends, only the analysis of the first labeled product is considered. The results of the 1,2- $^{13}\text{C}_2$ citric acid are displayed in neither Figure 3 nor Figure 4 since they were $<\text{LOQ}$. Comparing the chromatographic peak areas, though, a similar trend as for the unlabeled citric acid was observed.

As highlighted in the introduction, monocytes undergo phenotypic changes and contribute to the progress of inflammation. As this requires more energy, metabolic reprogramming is observed. The results shown in this study corroborate this hypothesis. In line with another study by Ren et al. [57], monocytes and macrophages increase their glycolysis during their phenotypic conversion, e.g., from homeostatic to inflammatory state [58–60]. The role of citric acid in CSF, though, is multifaceted. It is a good chelating agent (therefore, a challenging analyte for LC analysis) and many studies correlated its concentrations in CSF to calcium, magnesium, or zinc cations [61,62]. Infantino et al. showed that citrate and the mitochondrial citrate carrier play a significant role in inflammation [63,64]. However, at present, it is not possible to discriminate between potential reasons for increased concentrations of citric acid in CSF-treated groups. Even if it is safe to hypothesize that there is increased glycolytic activity to support cell activation and phenotypic changes, it is not excluded that its role may be more complex and correlated to the new compartment.

Increased glucose-derived glutamine (both unlabeled and ^{13}C -labeled) in monocytes treated with CSF confirms an enhancement of the TCA cycle in CSF-treated monocytes. However, this amino acid is also present in CSF. Thus, it serves as an extra source of glutamine that is not present in the NS group, which was incubated in a glutamine-free medium. However, there is a clear increase in glutamine amounts in cell extract and medium compared with CSF only (Figure 6). Moreover, the MScI group presents significant differences also with CON in the cell extract (Figure 2), and with CON and AD in the medium (Figure 4), suggesting different activation phenotypes in monocytes from patients

with neuroinflammatory conditions such as MScl to those with neurodegeneration such as AD.

As shown above, the level of glutamic acid was significantly decreased in monocytes treated with CSF from patients with AD and MScl, whereas treatment with CON-CSF resulted in a similar level of glutamic acid. This supports the finding that, in the presence of CSF, monocytes show more likely reactive phenotypes, indicated by an increased glucose conversion via pyruvate and citric acid towards glutamine (possibly through the TCA cycle), especially for healthy individuals and, to a slightly lesser extent, for patients with lower neuroinflammatory conditions (AD). This also implies the need for energy (e.g., via ATP production) during phenotypic alteration and a differentiation in the metabolism rewiring between AD and MScl neuroinflammatory conditions. Figure 7 summarizes these changes; in red are highlighted the metabolites that present a decrease in concentration after the stimulation with CSF, and in blue are those that show an increase.

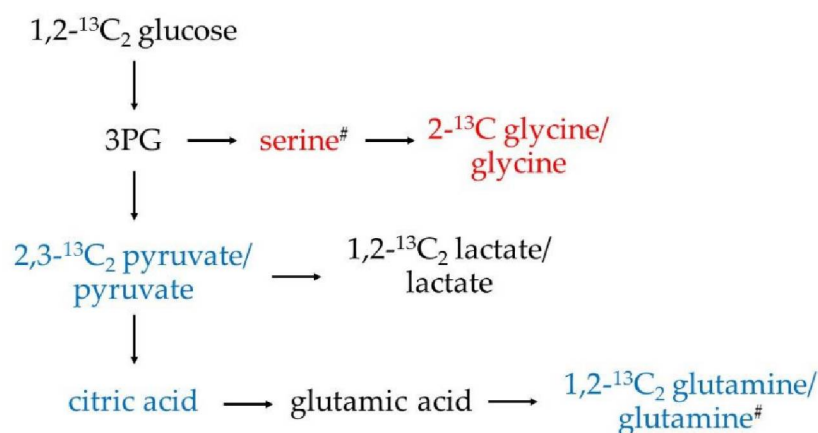


Figure 7. Alteration of metabolic pathways of the cell. In red are highlighted the metabolites that presented a significant decrease in the concentration when treated with CSF, and in blue, those that presented a significant increase. ^{13}C citric acid and ^{13}C glutamic acid were detectable but not quantifiable because of their fast interconversion towards ^{13}C glutamine, and therefore, are not displayed. The metabolites highlighted with “#” are significantly different between diseases (ADvsMScl), suggesting different activation phenotypes between AD and MScl.

Furthermore, glutamate is neurotoxic at certain concentrations in CSF, although it is essential for the homeostasis of the body. Conversion of glutamate to glutamine is one of the mechanisms to eliminate the excess of glutamate to maintain system homeostasis. Of note, MScl patients usually show elevated levels of glutamate in the brain, leading to excitotoxicity [65–67]. However, as shown in this study, this is not the case for monocytes in the CSF environment. Moreover, low levels of glutamate in the parietal and cingulate regions and right hippocampus were correlated to loss of memory and cognitive impairment [68]. Moreover, glutamine/glutamate levels are connected to nitric oxide production. They may also contribute to the formation of glutathione and play a role in antioxidant defenses [69].

The CSF-stimulated groups exhibited lower concentrations of glycine and serine in comparison with NS. The pathway towards the production of these amino acids passes through 3-phosphoglyceric acid (3PG). Thus, monocytes, when stimulated with CSF, diverge the metabolism of 3PG towards the production of pyruvate instead of glycine and serine. Under LPS-stimulation, glycine shows modulatory effects on cytokine production of monocytes, that is, a reduction in TNF- α and IL-1 β expression [70]. These results show that, under the applied experimental conditions (with CSF treatment), monocytes adapted their reactive phenotypes by increasing glycolysis via pyruvate conversion to glutamine

and reducing other metabolic pathways such as serine and glycine conversion. The levels of serine also differ between AD and MScl groups, suggesting again different phenotypic alterations between the considered diseases.

5. Conclusions

In summary, we report a significant alteration in the metabolism of monocytes when incubated with CSF. Overall, the metabolism showed a preference towards the TCA cycle and production of glutamine for the cells incubated with CSF, especially those from patients with AD and MScl. Other metabolic pathways such as serine and glycine production were down-regulated. These changes in glycolysis imply the alteration of monocyte phenotypes towards a reactive state. However, our study has some limitations, including: (1) it presents a limited number of biological replicates due to the rarity of the specimen CSF considered; (2) it uses an *in vitro* experimental model that may not completely explain the *in vivo* situation, and; (3) due to low cell numbers, some concentrations of the metabolites were lower than the limit of detection and/or limit of quantitation. Therefore, optimization and further development of the analytical methods are required, including the use of labeled glutamine for the parallel characterization of TCA cycle metabolites [71,72] and the use of a completely bioinert LC-MS/MS system.

Understanding how blood monocytes respond to the local environment (e.g., changing compartment from blood to CSF) at both phenotypic and functional/metabolic states will provide further insights on how to better regulate these cells, especially in neurological diseases, in which these cells play an important role [73,74].

Supplementary Materials: The following supporting information can be downloaded at: <https://www.mdpi.com/article/10.3390/cimb45010051/s1>, Table S1: Concentrations of the targeted analytes in cell lysate and culture medium. The reported concentrations are mean (\pm SD) values of three biological replicates.

Author Contributions: Conceptualization, G.G., M.K.P. and C.B.; methodology, G.G.; formal analysis, G.G.; investigation, G.G.; resources, C.B. and M.K.P.; writing—original draft preparation, G.G.; writing—review and editing, C.B. and M.K.P.; visualization, G.G.; supervision, M.K.P. and C.B.; project administration, C.B., M.K.P. and G.G.; funding acquisition, C.B., M.K.P. and G.G.; recruitment of the patients and access to biomaterials (CSF), J.P., K.R. and C.O. All authors have read and agreed to the published version of the manuscript.

Funding: G.G. and C.B. were funded by the German Research Foundation (DFG)—Project-ID 259373024—CRC/TRR 167 (B05). G.G. was additionally funded by the State of Berlin, Germany, with the Elsa Neumann Ph.D. scholarship (Antrags Nr.: 069032). Article processing charges (APC) are covered by the Open Access Publication Initiative of Freie Universität Berlin. K.R. received research support from Novartis Pharma, Merck Serono, German Ministry of Education and Research, European Union (821283-2), Stiftung Charité (BIH Clinical Fellow Program), and Arthur Arnstein Foundation, and received speaker honoraria from Bayer and travel grants from Guthy Jackson Charitable Foundation.

Institutional Review Board Statement: The study was approved by the Ethics Committee of Charité—Universitätsmedizin Berlin (Ethikkommission der Charité—Universitätsmedizin Berlin); registration number EA1/187/17).

Informed Consent Statement: Informed consent was obtained from all subjects involved in the study.

Data Availability Statement: Not applicable.

Acknowledgments: We would like to acknowledge the assistance of the Core Facility BioSupraMol supported by the DFG. The authors thank Bernhard Wüst, Agilent Technologies Inc., for his helpful support in mass spectrometry, and Adeline Dehlinger and Christian Böttcher for the sample collection of CSF and PBMCs. We acknowledge support by the Open Access Publication Fund of Freie Universität Berlin.

Conflicts of Interest: The authors declare no conflict of interest. The funders had no role in the design of the study; in the collection, analyses, or interpretation of data; in the writing of the manuscript, or in the decision to publish the results.

References

1. Prinz, M.; Jung, S.; Priller, J. Microglia Biology: One Century of Evolving Concepts. *Cell* **2019**, *179*, 292–311. [[CrossRef](#)] [[PubMed](#)]
2. Graeber, M.B. Neuroinflammation: No rose by any other name. *Brain Pathol.* **2014**, *24*, 620–622. [[CrossRef](#)] [[PubMed](#)]
3. Woodburn, S.C.; Bollinger, J.L.; Wohleb, E.S. The semantics of microglia activation: Neuroinflammation, homeostasis, and stress. *J. Neuroinflamm.* **2021**, *18*, 258. [[CrossRef](#)] [[PubMed](#)]
4. Zrzavy, T.; Hametner, S.; Wimmer, I.; Butovsky, O.; Weiner, H.L.; Lassmann, H. Loss of ‘homeostatic’ microglia and patterns of their activation in active multiple sclerosis. *Brain* **2017**, *140*, 1900–1913. [[CrossRef](#)] [[PubMed](#)]
5. Patel, H.C.; Boutin, H.; Allan, S.M. Interleukin-1 in the brain: Mechanisms of action in acute neurodegeneration. *Ann. N. Y. Acad. Sci.* **2003**, *992*, 39–47. [[CrossRef](#)]
6. Griffin, W.S.; Stanley, L.C.; Ling, C.; White, L.; MacLeod, V.; Perrot, L.J.; White, C.L., 3rd; Araoz, C. Brain interleukin 1 and S-100 immunoreactivity are elevated in Down syndrome and Alzheimer disease. *Proc. Natl. Acad. Sci. USA* **1989**, *86*, 7611–7615. [[CrossRef](#)]
7. Zhao, M.; Cribbs, D.H.; Anderson, A.J.; Cummings, B.J.; Su, J.H.; Wasserman, A.J.; Cotman, C.W. The induction of the TNF α death domain signaling pathway in Alzheimer’s disease brain. *Neurochem. Res.* **2003**, *28*, 307–318. [[CrossRef](#)]
8. Kouwenhoven, M.; Teleshova, N.; Ozenci, V.; Press, R.; Link, H. Monocytes in multiple sclerosis: Phenotype and cytokine profile. *J. Neuroimmunol.* **2001**, *112*, 197–205. [[CrossRef](#)]
9. Prinz, M.; Priller, J. The role of peripheral immune cells in the CNS in steady state and disease. *Nat. Neurosci.* **2017**, *20*, 136–144. [[CrossRef](#)]
10. Takata, F.; Nakagawa, S.; Matsumoto, J.; Dohgu, S. Blood-Brain Barrier Dysfunction Amplifies the Development of Neuroinflammation: Understanding of Cellular Events in Brain Microvascular Endothelial Cells for Prevention and Treatment of BBB Dysfunction. *Front. Cell Neurosci.* **2021**, *15*, 661838. [[CrossRef](#)]
11. Stolp, H.B.; Dziegielewska, K.M. Review: Role of developmental inflammation and blood-brain barrier dysfunction in neurodevelopmental and neurodegenerative diseases. *Neuropathol. Appl. Neurobiol.* **2009**, *35*, 132–146. [[CrossRef](#)]
12. De Vries, H.E.; Kooij, G.; Frenkel, D.; Georgopoulos, S.; Monsonogo, A.; Janigro, D. Inflammatory events at blood-brain barrier in neuroinflammatory and neurodegenerative disorders: Implications for clinical disease. *Epilepsia* **2012**, *53* (Suppl. 6), 45–52. [[CrossRef](#)]
13. Paterka, M.; Siffrin, V.; Voss, J.O.; Werr, J.; Hoppmann, N.; Gollan, R.; Belikan, P.; Bruttger, J.; Birkenstock, J.; Jung, S.; et al. Gatekeeper role of brain antigen-presenting CD11c⁺ cells in neuroinflammation. *EMBO J.* **2016**, *35*, 89–101. [[CrossRef](#)]
14. Siffrin, V.; Brandt, A.U.; Herz, J.; Zipp, F. New Insights into Adaptive Immunity in Chronic Neuroinflammation. *Adv. Immunol.* **2007**, *96*, 1–40.
15. Jolivel, V.; Luessi, F.; Masri, J.; Kraus, S.H.P.; Hubo, M.; Poisa-Beiro, L.; Klebow, S.; Paterka, M.; Yogev, N.; Tumani, H.; et al. Modulation of dendritic cell properties by laquinimod as a mechanism for modulating multiple sclerosis. *Brain* **2013**, *136*, 1048–1066. [[CrossRef](#)]
16. Luessi, F.; Siffrin, V.; Zipp, F. Neurodegeneration in multiple sclerosis: Novel treatment strategies. *Expert Rev. Neurother.* **2012**, *12*, 1061–1077. [[CrossRef](#)]
17. Siffrin, V.; Vogt, J.; Radbruch, H.; Nitsch, R.; Zipp, F. Multiple sclerosis-candidate mechanisms underlying CNS atrophy. *Trends Neurosci.* **2010**, *33*, 202–210. [[CrossRef](#)]
18. Palmer, C.S.; Cherry, C.L.; Sada-Ovalle, L.; Singh, A.; Crowe, S.M. Glucose Metabolism in T Cells and Monocytes: New Perspectives in HIV Pathogenesis. *EBioMedicine* **2016**, *6*, 31–41. [[CrossRef](#)]
19. Torretta, S.; Scagliola, A.; Ricci, L.; Mainini, E.; Di Marco, S.; Cuccovillo, I.; Kajaste-Rudnitski, A.; Sumpton, D.; Ryan, K.M.; Cardaci, S. D-mannose suppresses macrophage IL-1 β production. *Nat. Commun.* **2020**, *11*, 6343. [[CrossRef](#)]
20. Cheng, S.C.; Quintin, J.; Cramer, R.A.; Shepardson, K.M.; Saeed, S.; Kumar, V.; Giamarellos-Bourboulis, E.J.; Martens, J.H.; Rao, N.A.; Aghajani-rehah, A.; et al. mTOR- and HIF-1 α -mediated aerobic glycolysis as metabolic basis for trained immunity. *Science* **2014**, *345*, 1250684. [[CrossRef](#)]
21. Fernandez Zapata, C.; Giacomello, G.; Spruth, E.J.; Middeldorp, J.; Gallaccio, G.; Dehlinger, A.; Dames, C.; Leman, J.K.H.; van Dijk, R.E.; Meisel, A.; et al. Differential compartmentalization of myeloid cell phenotypes and responses towards the CNS in Alzheimer’s disease. *Nat. Commun.* **2022**, *13*, 7210. [[CrossRef](#)] [[PubMed](#)]
22. Schwartz, M.; Baruch, K. The resolution of neuroinflammation in neurodegeneration: Leukocyte recruitment via the choroid plexus. *EMBO J.* **2014**, *33*, 7–22. [[CrossRef](#)] [[PubMed](#)]
23. Varvel, N.H.; Neher, J.J.; Bosch, A.; Wang, W.; Ransohoff, R.M.; Miller, R.J.; Dingledine, R. Infiltrating monocytes promote brain inflammation and exacerbate neuronal damage after status epilepticus. *Proc. Natl. Acad. Sci. USA* **2016**, *113*, E5665–E5674. [[CrossRef](#)] [[PubMed](#)]
24. Soto-Herederó, G.; Gomez de Las Heras, M.M.; Gabande-Rodríguez, E.; Oller, J.; Mittelbrunn, M. Glycolysis—A key player in the inflammatory response. *FEBS J.* **2020**, *287*, 3350–3369. [[CrossRef](#)] [[PubMed](#)]
25. Suzuki, H.; Hisamatsu, T.; Chiba, S.; Mori, K.; Kitazume, M.T.; Shimamura, K.; Nakamoto, N.; Matsuoka, K.; Ebinuma, H.; Naganuma, M.; et al. Glycolytic pathway affects differentiation of human monocytes to regulatory macrophages. *Immunol. Lett.* **2016**, *176*, 18–27. [[CrossRef](#)]

26. Bottcher, C.; Schlickeiser, S.; Sneeboer, M.A.M.; Kunkel, D.; Knop, A.; Paza, E.; Fidzinski, P.; Kraus, L.; Sniijders, G.J.L.; Kahn, R.S.; et al. Human microglia regional heterogeneity and phenotypes determined by multiplexed single-cell mass cytometry. *Nat. Neurosci.* **2019**, *22*, 78–90. [CrossRef]
27. Zia, S.; Rawji, K.S.; Michaels, N.J.; Burr, M.; Kerr, B.J.; Healy, L.M.; Plemel, J.R. Microglia Diversity in Health and Multiple Sclerosis. *Front. Immunol.* **2020**, *11*, 588021. [CrossRef]
28. Mathias, A.; Perriard, G.; Canales, M.; Soneson, C.; Delorenzi, M.; Schlupe, M.; Du Pasquier, R.A. Increased ex vivo antigen presentation profile of B cells in multiple sclerosis. *Mult. Scler.* **2017**, *23*, 802–809. [CrossRef]
29. Schulz, D.; Severin, Y.; Zanotelli, V.R.T.; Bodenmiller, B. In-Depth Characterization of Monocyte-Derived Macrophages using a Mass Cytometry-Based Phagocytosis Assay. *Sci. Rep.* **2019**, *9*, 1925. [CrossRef]
30. Dreschers, S.; Ohl, K.; Lehrke, M.; Mollmann, J.; Denecke, B.; Costa, I.; Vogl, T.; Viemann, D.; Roth, J.; Orlikowsky, T.; et al. Impaired cellular energy metabolism in cord blood macrophages contributes to abortive response toward inflammatory threats. *Nat. Commun.* **2019**, *10*, 1685. [CrossRef]
31. Sohrabi, Y.; Sonntag, G.V.H.; Braun, L.C.; Lagache, S.M.M.; Liebmann, M.; Klotz, L.; Godfrey, R.; Kahles, F.; Waltenberger, J.; Findeisen, H.M. LXR Activation Induces a Proinflammatory Trained Innate Immunity-Phenotype in Human Monocytes. *Front. Immunol.* **2020**, *11*, 353. [CrossRef]
32. Pence, B.D.; Yarbro, J.R. Aging impairs mitochondrial respiratory capacity in classical monocytes. *Exp. Gerontol.* **2018**, *108*, 112–117. [CrossRef]
33. McGarry, T.; Hanlon, M.M.; Marzaioli, V.; Cunningham, C.C.; Krishna, V.; Murray, K.; Hurson, C.; Gallagher, P.; Nagpal, S.; Veale, D.J.; et al. Rheumatoid arthritis CD14(+) monocytes display metabolic and inflammatory dysfunction, a phenotype that precedes clinical manifestation of disease. *Clin. Transl. Immunol.* **2021**, *10*, e1237. [CrossRef]
34. Ong, S.M.; Hadadi, E.; Dang, T.M.; Yeap, W.H.; Tan, C.T.; Ng, T.P.; Larbi, A.; Wong, S.C. The pro-inflammatory phenotype of the human non-classical monocyte subset is attributed to senescence. *Cell Death Dis.* **2018**, *9*, 266. [CrossRef]
35. Michlmayr, D.; Kim, E.Y.; Rahman, A.H.; Raghunathan, R.; Kim-Schulze, S.; Che, Y.; Kalayci, S.; Gumus, Z.H.; Kuan, G.; Balmaseda, A.; et al. Comprehensive Immunoprofiling of Pediatric Zika Reveals Key Role for Monocytes in the Acute Phase and No Effect of Prior Dengue Virus Infection. *Cell Rep.* **2020**, *31*, 107569. [CrossRef]
36. Mason, G.F.; Gruetter, R.; Rothman, D.L.; Behar, K.L.; Shulman, R.G.; Novotny, E.J. Simultaneous determination of the rates of the TCA cycle, glucose utilization, alpha-ketoglutarate/glutamate exchange, and glutamine synthesis in human brain by NMR. *J. Cereb. Blood Flow Metab.* **1995**, *15*, 12–25. [CrossRef]
37. Mason, G.F.; Falk Petersen, K.; de Graaf, R.A.; Kanamatsu, T.; Otsuki, T.; Shulman, G.I.; Rothman, D.L. A comparison of (13)C NMR measurements of the rates of glutamine synthesis and the tricarboxylic acid cycle during oral and intravenous administration of [1-(13)C]glucose. *Brain Res. Brain Res. Protoc.* **2003**, *10*, 181–190. [CrossRef]
38. Fuchs, A.L.; Schiller, S.M.; Keegan, W.J.; Ammons, M.C.B.; Eilers, B.; Tripet, B.; Copie, V. Quantitative (1)H NMR Metabolomics Reveal Distinct Metabolic Adaptations in Human Macrophages Following Differential Activation. *Metabolites* **2019**, *9*, 248. [CrossRef]
39. Noga, M.J.; Dane, A.; Shi, S.; Attali, A.; van Aken, H.; Suidgeest, E.; Tuinstra, T.; Muilwijk, B.; Coulier, L.; Luider, T.; et al. Metabolomics of cerebrospinal fluid reveals changes in the central nervous system metabolism in a rat model of multiple sclerosis. *Metabolomics* **2012**, *8*, 253–263. [CrossRef]
40. Ahn, W.S.; Antoniewicz, M.R. Parallel labeling experiments with [1,2-(13)C]glucose and [U-(13)C]glutamine provide new insights into CHO cell metabolism. *Metab. Eng.* **2013**, *15*, 34–47. [CrossRef]
41. Al Kadhi, O.; Melchini, A.; Mithen, R.; Saha, S. Development of a LC-MS/MS Method for the Simultaneous Detection of Tricarboxylic Acid Cycle Intermediates in a Range of Biological Matrices. *J. Anal. Methods Chem.* **2017**, *2017*, 5391832. [CrossRef] [PubMed]
42. Zhu, X.; Meyers, A.; Long, D.; Ingram, B.; Liu, T.; Yoza, B.K.; Vachharajani, V.; McCall, C.E. Frontline Science: Monocytes sequentially rewire metabolism and bioenergetics during an acute inflammatory response. *J. Leukoc. Biol.* **2019**, *105*, 215–228. [CrossRef]
43. Agilent Technologies. How Agilent Seahorse XF Analyzers Work. Available online: <https://www.agilent.com/en/products/cell-analysis/how-seahorse-xf-analyzers-work> (accessed on 8 January 2022).
44. Giacomello, G.; Boettcher, C.; Parr, M.K. Isotopic tracing of glucose-metabolites in human monocytes to assess changes in inflammatory conditions. *STAR Protoc.* **2022**, *3*, 101715. [CrossRef] [PubMed]
45. Spalding, J.L.; Naser, F.J.; Mahieu, N.C.; Johnson, S.L.; Patti, G.J. Trace Phosphate Improves ZIC-pHILIC Peak Shape, Sensitivity, and Coverage for Untargeted Metabolomics. *J. Proteome Res.* **2018**, *17*, 3537–3546. [CrossRef] [PubMed]
46. Yang, S.; Sadilek, M.; Lidstrom, M.E. Streamlined pentafluorophenylpropyl column liquid chromatography–tandem quadrupole mass spectrometry and global 13C-labeled internal standards improve performance for quantitative metabolomics in bacteria. *J. Chromatogr. A* **2010**, *1217*, 7401–7410. [CrossRef]
47. Hsiao, J.J.; Van de Bittner, G.C.; Kennedy, A.P.; Wei, T.C. The Use of HILIC Zwitterionic Phase Superficially Porous Particles for Metabolomics Analysis. *Lc Gc N. Am.* **2018**, *36*, 30–35.
48. Regenold, W.T.; Phatak, P.; Makley, M.J.; Stone, R.D.; Kling, M.A. Cerebrospinal fluid evidence of increased extra-mitochondrial glucose metabolism implicates mitochondrial dysfunction in multiple sclerosis disease progression. *J. Neurol. Sci.* **2008**, *275*, 106–112. [CrossRef]
49. Omerhoca, S.; Akkas, S.Y.; Icen, N.K. Multiple Sclerosis: Diagnosis and Differential Diagnosis. *Noro Psikiyatr Ars* **2018**, *55*, S1–S9. [CrossRef]

50. Dumurgier, J.; Paquet, C.; Peoc'h, K.; Lapalus, P.; Mouton-Liger, F.; Benisty, S.; Chasseigneaux, S.; Chabriat, H.; Hugon, J. CSF Abeta(1-)(-)(4)(2) levels and glucose metabolism in Alzheimer's disease. *J. Alzheimers Dis.* **2011**, *27*, 845–851. [[CrossRef](#)]
51. Redjems-Bennani, N.; Jeandel, C.; Lefebvre, E.; Blain, H.; Vidailhet, M.; Gueant, J.L. Abnormal substrate levels that depend upon mitochondrial function in cerebrospinal fluid from Alzheimer patients. *Gerontology* **1998**, *44*, 300–304. [[CrossRef](#)]
52. Diskin, C.; Palsson-McDermott, E.M. Metabolic Modulation in Macrophage Effector Function. *Front. Immunol.* **2018**, *9*, 270. [[CrossRef](#)]
53. Izquierdo, E.; Cuevas, V.D.; Fernandez-Arroyo, S.; Riera-Borrull, M.; Orta-Zavalza, E.; Joven, J.; Rial, E.; Corbi, A.L.; Escribese, M.M. Reshaping of Human Macrophage Polarization through Modulation of Glucose Catabolic Pathways. *J. Immunol.* **2015**, *195*, 2442–2451. [[CrossRef](#)]
54. Raulien, N.; Friedrich, K.; Strobel, S.; Rubner, S.; Baumann, S.; von Bergen, M.; Korner, A.; Krueger, M.; Rossol, M.; Wagner, U. Fatty Acid Oxidation Compensates for Lipopolysaccharide-Induced Warburg Effect in Glucose-Deprived Monocytes. *Front. Immunol.* **2017**, *8*, 609. [[CrossRef](#)]
55. Lee, M.K.S.; Al-Sharea, A.; Shihata, W.A.; Bertuzzo Veiga, C.; Cooney, O.D.; Fleetwood, A.J.; Flynn, M.C.; Claeson, E.; Palmer, C.S.; Lancaster, G.I.; et al. Glycolysis Is Required for LPS-Induced Activation and Adhesion of Human CD14(+)CD16(-) Monocytes. *Front. Immunol.* **2019**, *10*, 2054. [[CrossRef](#)]
56. Dominguez-Andres, J.; Arts, R.J.W.; Ter Horst, R.; Gresnigt, M.S.; Smeekens, S.P.; Ratter, J.M.; Lachmandas, E.; Boutens, L.; van de Veerdonk, F.L.; Joosten, L.A.B.; et al. Rewiring monocyte glucose metabolism via C-type lectin signaling protects against disseminated candidiasis. *PLoS Pathog.* **2017**, *13*, e1006632. [[CrossRef](#)]
57. Ren, W.; Xia, Y.; Chen, S.; Wu, G.; Bazer, F.W.; Zhou, B.; Tan, B.; Zhu, G.; Deng, J.; Yin, Y. Glutamine Metabolism in Macrophages: A Novel Target for Obesity/Type 2 Diabetes. *Adv. Nutr.* **2019**, *10*, 321–330. [[CrossRef](#)]
58. Spiljar, M.; Kuchroo, V.K. Metabolic regulation and function of T helper cells in neuroinflammation. *Semin. Immunopathol.* **2022**, *44*, 581–598. [[CrossRef](#)]
59. Stienstra, R.; Netea-Maier, R.T.; Riksen, N.P.; Joosten, L.A.B.; Netea, M.G. Specific and Complex Reprogramming of Cellular Metabolism in Myeloid Cells during Innate Immune Responses. *Cell Metab.* **2017**, *26*, 142–156. [[CrossRef](#)]
60. Nishizawa, T.; Kanter, J.E.; Kramer, F.; Barnhart, S.; Shen, X.; Vivekanandan-Giri, A.; Wall, V.Z.; Kowitz, J.; Devaraj, S.; O'Brien, K.D.; et al. Testing the role of myeloid cell glucose flux in inflammation and atherosclerosis. *Cell Rep.* **2014**, *7*, 356–365. [[CrossRef](#)]
61. Westergaard, N.; Waagepetersen, H.S.; Belhage, B.; Schousboe, A. Citrate, a Ubiquitous Key Metabolite with Regulatory Function in the CNS. *Neurochem. Res.* **2017**, *42*, 1583–1588. [[CrossRef](#)]
62. Mellerup, E.T.; Rafaelsen, O.J. Depression and cerebrospinal fluid citrate. *Acta Psychiatr. Scand.* **1981**, *63*, 57–60. [[CrossRef](#)] [[PubMed](#)]
63. Infantino, V.; Convertini, P.; Cucci, L.; Panaro, M.A.; Di Noia, M.A.; Calvello, R.; Palmieri, F.; Iacobazzi, V. The mitochondrial citrate carrier: A new player in inflammation. *Biochem. J.* **2011**, *438*, 433–436. [[CrossRef](#)] [[PubMed](#)]
64. O'Neill, L.A. A critical role for citrate metabolism in LPS signalling. *Biochem. J.* **2011**, *438*, e5–e6. [[CrossRef](#)] [[PubMed](#)]
65. Haroon, E.; Miller, A.H.; Sanacora, G. Inflammation, Glutamate, and Glia: A Trio of Trouble in Mood Disorders. *Neuropsychopharmacology* **2017**, *42*, 193–215. [[CrossRef](#)] [[PubMed](#)]
66. Levite, M. Glutamate, T cells and multiple sclerosis. *J. Neural Transm.* **2017**, *124*, 775–798. [[CrossRef](#)]
67. Kuzmina, U.S.; Zainullina, L.F.; Vakhitov, V.A.; Bakhtiyarova, K.Z.; Vakhitova, Y.V. The Role of Glutamate in the Pathogenesis of Multiple Sclerosis. *Neurosci. Behav. Physiol.* **2020**, *50*, 669–675. [[CrossRef](#)]
68. Muhlert, N.; Atzori, M.; De Vita, E.; Thomas, D.L.; Samson, R.S.; Wheeler-Kingshott, C.A.; Gcurts, J.J.; Miller, D.H.; Thompson, A.J.; Ciccarelli, O. Memory in multiple sclerosis is linked to glutamate concentration in grey matter regions. *J. Neurol. Neurosurg. Psychiatry* **2014**, *85*, 833–839. [[CrossRef](#)]
69. Newsholme, P.; Lima, M.M.; Procopio, J.; Pithon-Curi, T.C.; Doi, S.Q.; Bazotte, R.B.; Curi, R. Glutamine and glutamate as vital metabolites. *Braz. J. Med. Biol. Res.* **2003**, *36*, 153–163. [[CrossRef](#)]
70. Spittler, A.; Reissner, C.M.; Oehler, R.; Gornikiewicz, A.; Gruenberger, T.; Manhart, N.; Brodowicz, T.; Mittlboeck, M.; Boltz-Nitulescu, G.; Roth, E. Immunomodulatory effects of glycine on LPS-treated monocytes: Reduced TNF-alpha production and accelerated IL-10 expression. *EASEB J.* **1999**, *13*, 563–571. [[CrossRef](#)]
71. Zhang, J.; Ahn, W.S.; Gameiro, P.A.; Keibler, M.A.; Zhang, Z.; Stephanopoulos, G. ¹³C isotope-assisted methods for quantifying glutamine metabolism in cancer cells. *Methods Enzymol.* **2014**, *542*, 369–389. [[CrossRef](#)]
72. Antoniewicz, M.R. A guide to (¹³C) metabolic flux analysis for the cancer biologist. *Exp. Mol. Med.* **2018**, *50*, 1–13. [[CrossRef](#)]
73. Russell, D.G.; Huang, L.; VanderVen, B.C. Immunometabolism at the interface between macrophages and pathogens. *Nat. Rev. Immunol.* **2019**, *19*, 291–304. [[CrossRef](#)]
74. Wolfe, H.; Mela, V.; Minogue, A.M.; Miller, A.M.; McGuigan, C.; Williams, L.; Lohan, D.; Lawlor, B.A.; Lynch, M.A. Monocytes exposed to plasma from patients with Alzheimer's disease undergo metabolic reprogramming. *Neurosci. Res.* **2019**, *148*, 54–60. [[CrossRef](#)]

Disclaimer/Publisher's Note: The statements, opinions and data contained in all publications are solely those of the individual author(s) and contributor(s) and not of MDPI and/or the editor(s). MDPI and/or the editor(s) disclaim responsibility for any injury to people or property resulting from any ideas, methods, instructions or products referred to in the content.

Supplementary materials

Table S1. Concentrations of the targeted analytes in cell lysate and culture medium. The reported concentrations are mean (\pm SD) values of three biological replicates.

	Cell lysate				Incubation medium			
	NS	CON	AD	MScI	NS	CON	AD	MScI
	$\mu\text{g/mL}\pm\text{SD}\mu\text{g/mL}\pm\text{SD}\mu\text{g/mL}\pm\text{SD}\mu\text{g/mL}\pm\text{SD}\mu\text{g/mL}\pm\text{SD}\mu\text{g/mL}\pm\text{SD}\mu\text{g/mL}\pm\text{SD}$							
Pyruvate	1.30 \pm 0.60	2.48 \pm 0.09	2.35 \pm 0.44	1.87 \pm 0.45	3.49 \pm 0.12	8.21 \pm 0.65	8.38 \pm 0.70	7.39 \pm 0.98
2,3- ¹³ C ₂ pyruvate	0.55 \pm 0.19	0.78 \pm 0.08	0.710 \pm 0.14	0.623 \pm 0.19	1.43 \pm 0.09	2.25 \pm 0.13	2.32 \pm 0.05	2.16 \pm 0.19
Lactate	41.20 \pm 8.32	43.79 \pm 2.57	40.40 \pm 6.05	35.48 \pm 7.35	48.00 \pm 3.04	41.65 \pm 0.95	51.36 \pm 4.63	54.12 \pm 4.23
1,2- ¹³ C ₂ lactate	7.26 \pm 1.16	8.04 \pm 0.84	6.76 \pm 1.02	6.80 \pm 1.26	8.09 \pm 0.96	7.36 \pm 0.85	7.82 \pm 0.59	9.53 \pm 0.56
2- ¹³ C glycine	n.q.	n.q.	n.q.	n.q.	0.15*	n.q.	n.q.	n.q.
Glycine	6.68 \pm 1.63	4.73 \pm 0.45	3.96 \pm 0.55	3.93 \pm 0.82	12.22 \pm 0.14	8.75 \pm 0.35	8.22 \pm 0.19	8.96 \pm 0.49
1,2- ¹³ C ₂ glutamine	n.q.	0.05 \pm 0.01	0.04 \pm 0.01	0.031*	n.q.	0.09 \pm 0.01	0.09 \pm 0.004	0.06 \pm 0.01
Glutamine	1.27 \pm 0.35	6.40 \pm 0.94	5.56 \pm 0.98	3.71 \pm 1.02	2.24 \pm 0.07	12.35 \pm 1.04	12.39 \pm 0.64	9.24 \pm 1.04
Serine	12.51 \pm 3.80	8.30 \pm 0.82	6.97 \pm 0.96	6.91 \pm 1.82	25.24 \pm 0.20	17.41 \pm 0.39	15.65 \pm 0.09	16.95 \pm 0.19
Glutamic acid	7.67 \pm 2.94	8.44 \pm 0.98	6.81 \pm 1.05	7.43 \pm 1.32	17.12 \pm 0.51	16.32 \pm 0.62	13.77 \pm 0.79	12.83 \pm 0.25
Citric acid	2.99 \pm 2.51	10.81 \pm 1.24	10.58 \pm 2.76	7.78 \pm 1.59	11.90 \pm 1.87	40.90 \pm 1.44	41.27 \pm 1.91	34.12 \pm 4.58

* Only one sample over the three biological replicates presented the analyte; n.q. denotes "not quantifiable".

4 Declaration of Own Contribution

In the following are disclosed the contribution of the author to the individual publications included in this cumulative work:

Manuscript I

- Conceptualisation together with co-authors
- HPLC-MS/MS method development, optimisation, and validation
- Incubation and cell extraction together with co-author
- Data analysis and evaluation of the results in cooperation with co-authors
- Preparation of the manuscript and revision with co-authors

Manuscript II

- Conceptualisation together with co-authors
- Incubation and cell extraction together with co-authors
- *In vitro* experiments with co-authors
- Metabolomic tracing experiments
- HPLC-MS/MS analysis, data evaluation, and elaboration of the results with co-authors
- Revision of the manuscript in cooperation with co-authors

Manuscript III

- Conceptualisation in cooperation with co-authors
- *In vitro* experiments together with co-authors
- HPLC-MS/MS analysis, data evaluation, and elaboration of the results
- Preparation of the manuscript and revision in cooperation with co-authors

5 Discussion and Outlook

This study provides an in-depth characterisation of the metabolic changes of blood monocytes exposed to the CSF of healthy individuals or patients with AD or MScl using the optimised and validated HPLC-MS/MS workflow described in Manuscript I. It provides an insight into the metabolic rewiring of myeloid cells in case of a compartment change due to an impaired BSCFB. This knowledge may assist the research investigating the characteristics and evolution of neuroinflammatory (MScl) or neurodegenerative (AD) diseases. Moreover, the developed analytical method can be applied to investigate the metabolic alterations *in vitro* of other primary cells (e.g. circulating immune cells like T and B cells or resident cells such as microglia, astrocytes, macrophages) or cell lines under various disease conditions as well as different experimental stimulations (e.g. lipopolysaccharide (LPS), CSF of patients with other neurological diseases, or interferon- γ (IFN- γ)). It may also have potential in investigating drug exposure and the resulting alteration in cell metabolism. Therefore, results obtained from this study will be of interest in a wide range of scientific areas, including but not limited to neuroscience, physiology, biochemistry, and analytical chemistry.

Central carbon metabolism (CCM), previously described in Chapter 1.2, has a prominent role in evaluating the well-being of a cell [77-79]. Therefore, the availability of a suitable HPLC-MS/MS method for analysing metabolites of CCM, possibly in one analytical run, is essential. However, as highlighted in Chapter 2.3, the analysis of CCM metabolites is particularly challenging [80]. The results obtained in this project address these challenges and take a step forward toward a more comprehensive understanding of the interactions at the interface between blood and CNS.

Manuscript I describes a method for incubating primary cells and the optimisation and validation for the simultaneous analysis of key-role metabolites of glucose (Table 1) with HPLC coupled by electrospray ionisation to QQQ mass spectrometry (HPLC-ESI-QQQ-MS). Method development started from the HPLC method suggested by Hsiao *et al.* [60], which included the passivation of the system and the addition of medronic acid to the mobile phases. The protocol has been optimised for the targeted analytes and combined with the newly developed method for MS/MS with dynamic multiple reaction monitoring (dMRM). In Manuscript I, the whole procedure, its validation, and its successful application for quantifying the metabolites of the *in vitro* cultures of PBMCs (cell lysate) and monocytes (cell lysate and incubation medium) are detailed. In addition, as mentioned in Chapter 2.2, isotopically labelled tracers are a powerful tool for elucidating metabolic rewiring and studies of metabolomics [81-83]. The corresponding isotopologues of the targeted metabolites generated by the incubation with [1,2-¹³C₂]glucose were also quantified in the same analytical run. The presented protocol may be of relevance for future investigations on the metabolism of PBMCs, including monocytes with or without [1,2-¹³C₂]glucose as isotopic tracers. It provides, in fact, a method that can simultaneously analyse and quantify metabolites that are very different from each other for polarity, masses, and physicochemical properties. Moreover, the presented protocol overcomes the chromatographic challenges of phosphate and other chelating compounds. It can be easily applied to metabolic investigations on other cells and, hence, in several biochemical studies on CCM. One last aspect remains to be solved: the separation of the two isomers, citrate and isocitrate. So far, the method cannot fully separate the two peaks.

Once the homeostasis of myeloid cells is altered, whether because of a change of compartment or/and due to the increased presence of inflammatory mediators in the surrounding microenvironment, the CCM may get affected as

well [84-87]. Indeed, these metabolic alterations can help to better understand cell activation or responses to neuroinflammation or diseases [88-90].

Manuscript II describes the effects that a change in environment and the presence of an activator, such as LPS, may have on the metabolism of monocytes *in vitro*. Monocytes isolated from PBMCs with magnetic-activated cell separation (MACS) were incubated with [1,2-¹³C₂]glucose under different conditions to obtain six parallel *in vitro* models: three to simulate the change of compartment from the bloodstream into CSF of either healthy or diseased individuals (monocytes without stimulation, with the addition of CSF of healthy donors, and with CSF of AD patients), and three in the same conditions but with LPS as extra activation factor. The CSF-stimulated monocytes showed a significantly increased glycolysis and ¹³C₂-pyruvate production, especially with CSF of AD patients (AD-CSF). Moreover, the conversion of [1,2-¹³C₂]glucose into [¹³C₂]serine is significantly reduced in cells incubated with CSF. Lastly, the addition of LPS produced a slightly bigger variation in the metabolism of AD-CSF, suggesting an increased vulnerability of the monocytes of AD patients towards microenvironment changes.

Different studies have already highlighted the importance of monocytes in neuroinflammation and neurodegeneration [91, 92]. This thesis aims to give a clearer picture of their fate with an impaired BCSFB. In fact, the results presented in Manuscript II and Manuscript III demonstrate how the blood-derived monocytes rewire their bioenergetic pathways when in contact with CSF, activating the glycolytic pathway detrimental to serine production. These original findings provide further insight into how monocytes are regulated in different environments and conditions. Therefore, they are of interest to studies on neurological diseases, especially AD and MScl.

Manuscript III takes a more comprehensive step further in describing the changes in the metabolism of infiltrating monocytes, considering not only AD but also a typically neuroinflammatory disease such as MScl. Chapter 1.1 gives

a more in-depth description of the commonalities and differences between the two conditions reported so far. The relevant common aspects are briefly summarised to ease the discussion. Both diseases present, sooner or later, neuroinflammatory features such as microglial activation [93-96], increased production of pro- and anti-inflammatory mediators [97-100], and impaired BCSFB with consequent infiltration of monocytes [26-29]. In the study presented in this manuscript, the overall [1,2-¹³C₂]glucose metabolism of monocytes has been evaluated for four different conditions: without stimulation, with the stimulation of CSF of healthy donors (CON-CSF), with AD-CSF, and with CSF of MScl patients (MScl-CSF). Both cell lysate and incubation medium have been analysed with the HPLC-ESI-QQQ method detailed in Manuscript I.

The results show a more active glycolytic pathway and TCA cycle for monocytes incubated with CSF (CON-, AD-, MScl-CSF) with higher citrate, pyruvate, and glutamine concentrations in both cell extract and medium. The presence of labelled glutamine only in the CSF-treated groups confirms the more active and preferential pathway. Also in this case, as highlighted in Manuscript II, the production of serine and glycine is reduced. In addition, the only group that presented labelled glycine was the one without stimulation. To explain this metabolic rewiring, it was hypothesised in Manuscript III that it is necessary to support the phenotypic changes and activation that occur to monocytes in the shift of compartment. Several studies on the activation of human immune cells [101-105] and phenotypic conversion of monocytes and macrophages sustain this hypothesis [106-109]. There are also some differences between CSF groups, especially between CON-CSF and AD-, MScl-CSF (e.g. amounts of glutamic acid and lactate in the medium) or between AD-CSF and MScl-CSF (e.g. glutamine and serine) suggesting differences in the phenotypic activation profiles of monocytes between diseases. These results are

of interest to neurological and immunological studies that focus on bioenergetic alterations.

In conclusion, this thesis provides a clear path in investigating the metabolic rewiring of immunological primary cells, such as PBMC-derived monocytes. First, it supplies an optimised and validated HPLC-ESI-QQQ-MS method for detecting and quantifying challenging, very polar analytes, such as the metabolites and intermediates of the CCM. Second, this method is applied to unwind the metabolic fate of infiltrating monocytes from the bloodstream into the CSF. The changes in metabolism are clearly highlighted thanks to stable isotopic tracing. Third, this work compares the immunometabolic alterations between healthy individuals and patients with AD or MScl. The presented results, therefore, provide an appropriate tool for bioenergetic studies in different neurological and immunological areas and a more in-depth insight into immunometabolism alterations related to neurological diseases, giving further knowledge to understand and possibly address the dramatic progression of AD and MScl.

The studies of this thesis provide the basis for a future, broader investigation of the impact of neuroinflammatory or neurodegenerative diseases on immunometabolism. This approach is suitable for multiple cell metabolism studies, not only for immune cells and related to CNS pathologies. Moreover, it provides a tool to research the effects of potential drugs and treatments on the adaptive metabolism of the cells. The focus of the research can be shifted to other metabolic pathways by using different stable isotopic tracers (as highlighted in Figure 3), and a comprehensive overview of the metabolic alterations over time may be obtained with a multiple time points approach. Lastly, the list of phosphorylated or highly polar compounds can be extended, including other challenging analytes such as, *inter alia*, phosphopeptides, nucleotides, fatty acyl-coenzyme A (FA-CoA), and organophosphate pesticides.

6 Summary

This thesis focuses on the study of the reprogramming of the immunometabolism of infiltrating monocytes during neuroinflammation. Three main results have been achieved.

First, the development and validation of a method for analysing changes in the major metabolic pathways of cells. To do so, the analytical challenges presented by the high polarity of the targeted metabolites and the chelating properties of citrate and phosphates have been addressed and overcome. The developed method allows the simultaneous analysis of key-role metabolites with HPLC-ESI-QQQ-MS. It is a suitable tool for future studies to quickly, reliably, and reproducibly investigate the metabolism of cells in different conditions or under various stimulations. The proof of concept of this method is shown by the results of the following two points.

Second, *in vitro* elucidation of monocyte metabolic alterations when infiltrating into the CSF from the bloodstream. These results provide an insight on the immunometabolism rewiring from the production of amino acids (serine and glycine) in normal conditions towards a more active TCA cycle and production of glutamine when stimulated with CSF. This knowledge gives a valuable overview of the effects caused by the compartment change of monocytes and provides the basis for understanding the metabolic adaptation of infiltrating immune cells under different conditions.

Third, the display of the significant variations in the metabolism reprogramming of infiltrating monocytes in three study cases: in healthy individuals, in patients with AD and with MScl. These outcomes elucidate how a healthy donor CSF affects monocytes compared to that of patients. Moreover, it distinguishes the alterations caused by a disease more correlated to

neurodegeneration, such as AD, from those caused by a disease primarily neuroinflammatory like MScl.

The results presented in this thesis are of relevance for a more in-depth understanding of the metabolic fate of monocytes in CSF and to build solid bases for further studies of their role in neuroinflammation. It is one step forward in elucidating the complexity of alterations that occur in our CNS in the case of neurodegenerative or neuroinflammatory diseases.

7 Zusammenfassung

Diese Arbeit konzentriert sich auf die Untersuchung der Umprogrammierung des Immunstoffwechsels von infiltrierenden Monozyten während einer Neuroinflammation. Es wurden drei Hauptergebnisse erzielt.

Erstens, die Entwicklung und Validierung einer Methode zur Untersuchung von Veränderungen in den wichtigsten Stoffwechselwegen von Zellen. Zu diesem Zweck wurden die analytischen Herausforderungen, die sich aus der hohen Polarität der Zielmetaboliten und den chelatbildenden Eigenschaften von Citrat und Phosphaten ergeben, angegangen und überwunden. Die entwickelte Methode ermöglicht die gleichzeitige Analyse von essentiellen Metaboliten mittels HPLC-ESI-QQQ-MS. Diese ist ein geeignetes Werkzeug für zukünftige Studien, um schnell, zuverlässig und reproduzierbar den Stoffwechsel von Zellen unter verschiedenen Bedingungen oder Stimuli zu untersuchen. Der Beweis für die Wirksamkeit dieser Methode wird durch die Ergebnisse der folgenden zwei Punkte erbracht.

Zweitens, *in-vitro*-Aufklärung der metabolischen Veränderungen von Monozyten, die aus dem Blutkreislauf in den Liquor eindringen. Die Ergebnisse geben einen Einblick in die Umstellung des Immunstoffwechsels von der Produktion von Aminosäuren (Serin und Glycin) unter normalen Bedingungen auf einen aktivierten Tricarbonsäurezyklus und die Produktion von Glutamin, wenn die Zellen mit Liquor stimuliert werden. Diese Erkenntnisse geben einen wertvollen Überblick über die Auswirkungen des Übergang der Monozyten in ein anderes Kompartiment und bilden die Grundlage für das Verständnis der metabolischen Anpassung von infiltrierenden Immunzellen unter verschiedenen Bedingungen.

Drittens, die Darstellung der signifikanten Unterschiede in der Reprogrammierung des Stoffwechsels der infiltrierenden Monozyten in drei

Studienfällen: bei gesunden Personen, bei Patienten mit Alzheimer und mit Multiple Sklerose. Diese Ergebnisse geben Aufschluss darüber, wie sich der Liquor eines gesunden Spenders auf die Monozyten auswirkt, im Vergleich zu demjenigen von Patienten. Darüber hinaus wird zwischen den Veränderungen unterschieden, die durch eine Krankheit verursacht werden, die eher mit Neurodegeneration korreliert, wie z.B. Alzheimer, und denen, die durch eine primär neuroinflammatorische Krankheit wie MScl verursacht werden.

Die in dieser Arbeit vorgestellten Ergebnisse sind für ein tieferes Verständnis des metabolischen Schicksals der Monozyten im Liquor von Bedeutung und bilden eine solide Grundlage für weitere Studien über ihre Rolle bei Neuroinflammationen. Somit sind diese Erkenntnisse ein weiterer Schritt zur Aufklärung der komplexen Veränderungen, die in unserem zentralen Nervensystem bei neurodegenerativen oder neuroinflammatorischen Erkrankungen auftreten.

8 References

- [1] Alzheimer's Disease International (ADI): Dementia statistics (2019) Available at: <https://www.alzint.org/about/dementia-facts-figures/dementia-statistics/>. Accessed on: 24.02.2023
- [2] National Multiple Sclerosis Society: News (2020) Available at: <https://www.nationalmssociety.org/About-the-Society/News/Updated-Atlas-of-MS-Shows-Over-2-8-million-People>. Accessed on: 24.02.2023
- [3] Mucke L. Neuroscience: Alzheimer's disease. *Nature* 461 (2009) 895-897
- [4] Lane CA, Hardy J, Schott JM. Alzheimer's disease. *Eur J Neurol* 25 (2018) 59-70
- [5] Cummings JL. Alzheimer's disease. *N Engl J Med* 351 (2004) 56-67
- [6] Ballard C, Gauthier S, Corbett A, Brayne C, Aarsland D, Jones E. Alzheimer's disease. *Lancet* 377 (2011) 1019-1031
- [7] Soria Lopez JA, González HM, Léger GC. Chapter 13 - Alzheimer's disease. In: Dekosky ST, Asthana S (Eds.) *Handbook of Clinical Neurology*, Elsevier, (2019) 231-255
- [8] Masters CL, Bateman R, Blennow K, Rowe CC, Sperling RA, Cummings JL. Alzheimer's disease. *Nat Rev Dis Primers* 1 (2015) 15056
- [9] Heneka MT, Carson MJ, El Khoury J, Landreth GE, Brosseron F, Feinstein DL, Jacobs AH, Wyss-Coray T, Vitorica J, Ransohoff RM, Herrup K, Frautschy SA, Finsen B, Brown GC, Verkhratsky A, Yamanaka K, Koistinaho J, Latz E, Halle A, Petzold GC, Town T, Morgan D, Shinohara ML, Perry VH, Holmes C, Bazan NG, Brooks DJ, Hunot S, Joseph B, Deigendesch N, Garaschuk O, Boddeke E, Dinarello CA, Breitner JC, Cole GM, Golenbock DT, Kummer MP. Neuroinflammation in Alzheimer's disease. *Lancet Neurol* 14 (2015) 388-405
- [10] Calsolaro V, Edison P. Neuroinflammation in Alzheimer's disease: Current evidence and future directions. *Alzheimers Dement* 12 (2016) 719-732
- [11] Ghasemi N, Razavi S, Nikzad E. Multiple Sclerosis: Pathogenesis, Symptoms, Diagnoses and Cell-Based Therapy. *Cell J* 19 (2017) 1-10
- [12] Mcginley MP, Goldschmidt CH, Rae-Grant AD. Diagnosis and Treatment of Multiple Sclerosis: A Review. *JAMA* 325 (2021) 765-779
- [13] Smith KJ, Mcdonald WI. The pathophysiology of multiple sclerosis: the mechanisms underlying the production of symptoms and the natural

- history of the disease. *Philos Trans R Soc Lond B Biol Sci* 354 (1999) 1649-1673
- [14] Dobson R, Giovannoni G. Multiple sclerosis - a review. *Eur J Neurol* 26 (2019) 27-40
- [15] Hayes CE, Cantorna MT, Deluca HF. Vitamin D and multiple sclerosis. *Proc Soc Exp Biol Med* 216 (1997) 21-27
- [16] Ebers GC, Sadovnick AD. The role of genetic factors in multiple sclerosis susceptibility. *J Neuroimmunol* 54 (1994) 1-17
- [17] Lassmann H. Multiple Sclerosis Pathology. *Cold Spring Harb Perspect Med* 8 (2018) a028936
- [18] Mahad D, Ziabreva I, Lassmann H, Turnbull D. Mitochondrial defects in acute multiple sclerosis lesions. *Brain* 131 (2008) 1722-1735
- [19] Perry VH, Holmes C. Microglial priming in neurodegenerative disease. *Nat Rev Neurol* 10 (2014) 217-224
- [20] Brkic M, Balusu S, Van Wonterghem E, Gorle N, Benilova I, Kremer A, Van Hove I, Moons L, De Strooper B, Kanazir S, Libert C, Vandebroucke RE. Amyloid beta Oligomers Disrupt Blood-CSF Barrier Integrity by Activating Matrix Metalloproteinases. *J Neurosci* 35 (2015) 12766-12778
- [21] Johanson C, Stopa E, Daiello L, De La Monte S, Keane M, Ott B. Disrupted blood-CSF barrier to urea and creatinine in mild cognitive impairment and Alzheimer's disease. *J Alzheimers Dis Parkinsonism* 8 (2018) 435
- [22] Hampel H, Hardy J, Blennow K, Chen C, Perry G, Kim SH, Villemagne VL, Aisen P, Vendruscolo M, Iwatsubo T, Masters CL, Cho M, Lannfelt L, Cummings JL, Vergallo A. The Amyloid-beta Pathway in Alzheimer's Disease. *Mol Psychiatry* 26 (2021) 5481-5503
- [23] Silverberg GD, Mayo M, Saul T, Rubenstein E, Mcguire D. Alzheimer's disease, normal-pressure hydrocephalus, and senescent changes in CSF circulatory physiology: a hypothesis. *Lancet Neurol* 2 (2003) 506-511
- [24] Amann L, Masuda T, Prinz M. Mechanisms of myeloid cell entry to the healthy and diseased central nervous system. *Nat Immunol* 24 (2023) 393-407
- [25] Ortiz GG, Pacheco-Moises FP, Macias-Islas MA, Flores-Alvarado LJ, Mireles-Ramirez MA, Gonzalez-Renovato ED, Hernandez-Navarro VE, Sanchez-Lopez AL, Alatorre-Jimenez MA. Role of the blood-brain barrier in multiple sclerosis. *Arch Med Res* 45 (2014) 687-697

- [26] Prinz M, Priller J. The role of peripheral immune cells in the CNS in steady state and disease. *Nat Neurosci* 20 (2017) 136-144
- [27] Takata F, Nakagawa S, Matsumoto J, Dohgu S. Blood-Brain Barrier Dysfunction Amplifies the Development of Neuroinflammation: Understanding of Cellular Events in Brain Microvascular Endothelial Cells for Prevention and Treatment of BBB Dysfunction. *Front Cell Neurosci* 15 (2021) 661838
- [28] Stolp HB, Dziegielewska KM. Review: Role of developmental inflammation and blood-brain barrier dysfunction in neurodevelopmental and neurodegenerative diseases. *Neuropathol Appl Neurobiol* 35 (2009) 132-146
- [29] De Vries HE, Kooij G, Frenkel D, Georgopoulos S, Monsonego A, Janigro D. Inflammatory events at blood-brain barrier in neuroinflammatory and neurodegenerative disorders: implications for clinical disease. *Epilepsia* 53 Suppl 6 (2012) 45-52
- [30] Wang A, Luan HH, Medzhitov R. An evolutionary perspective on immunometabolism. *Science* 363 (2019) eaar3932
- [31] Kaur G, Dufour JM. Cell lines: Valuable tools or useless artifacts. *Spermatogenesis* 2 (2012) 1-5
- [32] Reid YA. Characterization and Authentication of Cancer Cell Lines: An Overview. In: Cree IA (Ed.) *Cancer Cell Culture: Methods and Protocols*, Humana Press, Totowa, NJ (2011) 35-43
- [33] Esquenet M, Swinnen JV, Heyns W, Verhoeven G. LNCaP prostatic adenocarcinoma cells derived from low and high passage numbers display divergent responses not only to androgens but also to retinoids. *J Steroid Biochem Mol Biol* 62 (1997) 391-399
- [34] Gomez-Lechon M, Donato M, Castell J, Jover R. Human hepatocytes as a tool for studying toxicity and drug metabolism. *Current drug metabolism* 4 (2003) 292-312
- [35] Macdonald C. Development of new cell lines for animal cell biotechnology. *Crit Rev Biotechnol* 10 (1990) 155-178
- [36] Schurr MJ, Foster KN, Centanni JM, Comer AR, Wicks A, Gibson AL, Thomas-Virnig CL, Schlosser SJ, Faucher LD, Lokuta MA, Allen-Hoffmann BL. Phase I/II clinical evaluation of StrataGraft: a consistent, pathogen-free human skin substitute. *J Trauma* 66 (2009) 866-873; discussion 873-864

- [37] Bosshart H, Heinzelmann M. THP-1 cells as a model for human monocytes. *Ann Transl Med* 4 (2016) 438
- [38] Primary Cells. Essential tools to advance your life science research and drug discovery. Available at: <https://www.atcc.org/cell-products/primary-cells#t=productTab&numberOfResults=24>. Accessed on: 2023.06.02
- [39] Lee WN, Boros LG, Puigjaner J, Bassilian S, Lim S, Cascante M. Mass isotopomer study of the nonoxidative pathways of the pentose cycle with [1,2-¹³C₂]glucose. *Am J Physiol* 274 (1998) E843-851
- [40] Boros LG, Lerner MR, Morgan DL, Taylor SL, Smith BJ, Postier RG, Brackett DJ. [1,2-¹³C₂]-D-glucose profiles of the serum, liver, pancreas, and DMBA-induced pancreatic tumors of rats. *Pancreas* 31 (2005) 337-343
- [41] Micheli A, Tomassini A, Puccetti C, Valerio M, Peluso G, Tuccillo F, Calvani M, Manetti C, Conti F. Metabolic profiling by ¹³C-NMR spectroscopy: [1,2-¹³C₂]glucose reveals a heterogeneous metabolism in human leukemia T cells. *Biochimie* 88 (2006) 437-448
- [42] Jalloh I, Carpenter KL, Grice P, Howe DJ, Mason A, Gallagher CN, Helmy A, Murphy MP, Menon DK, Carpenter TA, Pickard JD, Hutchinson PJ. Glycolysis and the pentose phosphate pathway after human traumatic brain injury: microdialysis studies using 1,2-(¹³C)₂ glucose. *J Cereb Blood Flow Metab* 35 (2015) 111-120
- [43] Marin-Valencia I, Cho SK, Rakheja D, Hatanpaa KJ, Kapur P, Mashimo T, Jindal A, Vemireddy V, Good LB, Raisanen J, Sun X, Mickey B, Choi C, Takahashi M, Togao O, Pascual JM, Deberardinis RJ, Maher EA, Malloy CR, Bachoo RM. Glucose metabolism via the pentose phosphate pathway, glycolysis and Krebs cycle in an orthotopic mouse model of human brain tumors. *NMR Biomed* 25 (2012) 1177-1186
- [44] Ahn WS, Antoniewicz MR. Parallel labeling experiments with [1,2-(¹³C)]glucose and [U-(¹³C)]glutamine provide new insights into CHO cell metabolism. *Metab Eng* 15 (2013) 34-47
- [45] Ahn WS, Antoniewicz MR. Towards dynamic metabolic flux analysis in CHO cell cultures. *Biotechnol J* 7 (2012) 61-74
- [46] Zhang J, Ahn WS, Gameiro PA, Keibler MA, Zhang Z, Stephanopoulos G. ¹³C isotope-assisted methods for quantifying glutamine metabolism in cancer cells. *Methods Enzymol* 542 (2014) 369-389

- [47] Shree M, Masakapalli SK. Intracellular Fate of Universally Labelled (13)C Isotopic Tracers of Glucose and Xylose in Central Metabolic Pathways of *Xanthomonas oryzae*. *Metabolites* 8 (2018) 66
- [48] Wasylenko TM, Stephanopoulos G. Metabolomic and (13)C-metabolic flux analysis of a xylose-consuming *Saccharomyces cerevisiae* strain expressing xylose isomerase. *Biotechnol Bioeng* 112 (2015) 470-483
- [49] Van Gastel N, Spinelli JB, Sharda A, Schajnovitz A, Baryawno N, Rhee C, Oki T, Grace E, Soled HJ, Milosevic J, Sykes DB, Hsu PP, Vander Heiden MG, Vidoudez C, Trauger SA, Haigis MC, Scadden DT. Induction of a Timed Metabolic Collapse to Overcome Cancer Chemoresistance. *Cell Metab* 32 (2020) 391-403 e6
- [50] Zhang A, Sun H, Wang P, Han Y, Wang X. Modern analytical techniques in metabolomics analysis. *Analyst* 137 (2012) 293-300
- [51] Begou O, Gika HG, Wilson ID, Theodoridis G. Hyphenated MS-based targeted approaches in metabolomics. *Analyst* 142 (2017) 3079-3100
- [52] Klupczynska A, Plewa S, Derezinski P, Garrett TJ, Rubio VY, Kokot ZJ, Matysiak J. Identification and quantification of honeybee venom constituents by multiplatform metabolomics. *Sci Rep* 10 (2020) 21645
- [53] Patti GJ, Yanes O, Siuzdak G. Innovation: Metabolomics: the apogee of the omics trilogy. *Nat Rev Mol Cell Biol* 13 (2012) 263-269
- [54] Armstrong M, Jonscher K, Reisdorph NA. Analysis of 25 underivatized amino acids in human plasma using ion-pairing reversed-phase liquid chromatography/time-of-flight mass spectrometry. *Rapid Commun Mass Spectrom* 21 (2007) 2717-2726
- [55] Michopoulos F, Whalley N, Theodoridis G, Wilson ID, Dunkley TP, Critchlow SE. Targeted profiling of polar intracellular metabolites using ion-pair-high performance liquid chromatography and -ultra high performance liquid chromatography coupled to tandem mass spectrometry: applications to serum, urine and tissue extracts. *J Chromatogr A* 1349 (2014) 60-68
- [56] Lesellier EW, C.; Lemasson, E.; Hennig, P.; Bertin, S. Mixed-mode chromatography—a review. *LCGC Supplements* 30 (2017) 22–33
- [57] Wang LW, W.; Xia, Z.; Jie, X.; Xia, Z.Z. Recent advances in materials for stationary phases of mixed-mode high-performance liquid chromatography. *TrAC Trends in Analytical Chemistry* 80 (2016) 495-506
- [58] Mitchell CR, Bao Y, Benz NJ, Zhang S. Comparison of the sensitivity of evaporative universal detectors and LC/MS in the HILIC and the

- reversed-phase HPLC modes. *J Chromatogr B Analyt Technol Biomed Life Sci* 877 (2009) 4133-4139
- [59] Menzies C, Naz S, Patten D, Alquier T, Bennett BM, Lacoste B. Distinct Basal Metabolism in Three Mouse Models of Neurodevelopmental Disorders. *eNeuro* 8 (2021) ENEURO.0292-20.2021
- [60] Hsiao JJ, Potter OG, Chu TW, Yin H. Improved LC/MS Methods for the Analysis of Metal-Sensitive Analytes Using Medronic Acid as a Mobile Phase Additive. *Anal Chem* 90 (2018) 9457-9464
- [61] Czajka JJ, Kambhampati S, Tang YJ, Wang Y, Allen DK. Application of Stable Isotope Tracing to Elucidate Metabolic Dynamics During *Yarrowia lipolytica* alpha-Ionone Fermentation. *iScience* 23 (2020) 100854
- [62] McCalley DV. Influence of metals in the column or instrument on performance in hydrophilic interaction liquid chromatography. *J Chromatogr A* 1663 (2022) 462751
- [63] Cecchi T, Pucciarelli F, Passamonti P, Ferraro S. Influence of Metal Impurities Sorption onto a Silica Based C18 Stationary Phase on the Hplc of Metal Chelating Analytes. *Journal of Liquid Chromatography & Related Technologies* 22 (2007) 429-440
- [64] Cecchi T, Pucciarelli F, Passamonti P. Influence of Metal Ion Sorption onto a Styrene-Divinylbenzene C18 Stationary Phase on the Hplc of Metal Chelating Analytes. *Journal of Liquid Chromatography & Related Technologies* 22 (2012) 2467-2481
- [65] Guimaraes GJ, Bartlett MG. Managing nonspecific adsorption to liquid chromatography hardware: A review. *Anal Chim Acta* 1250 (2023) 340994
- [66] Girel S, Guillaume D, Fekete S, Rudaz S, Gonzalez-Ruiz V. Investigation of several chromatographic approaches for untargeted profiling of central carbon metabolism. *J Chromatogr A* 1697 (2023) 463994
- [67] Lai AC, Tsai CF, Hsu CC, Sun YN, Chen YJ. Complementary Fe(3+)- and Ti(4+)-immobilized metal ion affinity chromatography for purification of acidic and basic phosphopeptides. *Rapid Commun Mass Spectrom* 26 (2012) 2186-2194
- [68] Andersson L, Porath J. Isolation of phosphoproteins by immobilized metal (Fe³⁺) affinity chromatography. *Anal Biochem* 154 (1986) 250-254
- [69] Hamada YZ, Carlson BL, Shank JT. Potentiometric and UV-Vis spectroscopy studies of citrate with the hexaquo Fe³⁺ and Cr³⁺ metal ions. *Synthesis and Reactivity in Inorganic and Metal-Organic Chemistry* 33 (2003) 1425-1440

- [70] Minotti G, Aust SD. Superoxide-dependent redox cycling of citrate-Fe³⁺: evidence for a superoxide dismutaselike activity. *Arch Biochem Biophys* 253 (1987) 257-267
- [71] Pesek JJ, Matyska MT, Fischer SM. Improvement of peak shape in aqueous normal phase analysis of anionic metabolites. *J Sep Sci* 34 (2011) 3509-3516
- [72] Myint KT, Uehara T, Aoshima K, Oda Y. Polar anionic metabolome analysis by nano-LC/MS with a metal chelating agent. *Anal Chem* 81 (2009) 7766-7772
- [73] Lin YT, Chan SA, Chen YJ, Chung KP, Kuo CH. Using an In-Sample Addition of Medronic Acid for the Analysis of Purine- and Pyrimidine-Related Derivatives and Its Application in the Study of Lung Adenocarcinoma A549 Cell Lines by LC-MS/MS. *J Proteome Res* 22 (2023) 1434-1445
- [74] Maqdasy S, Lecoutre S, Renzi G, Frendo-Cumbo S, Rizo-Roca D, Moritz T, Juvany M, Hodek O, Gao H, Couchet M, Witting M, Kerr A, Bergo MO, Choudhury RP, Aouadi M, Zierath JR, Krook A, Mejhert N, Ryden M. Impaired phosphocreatine metabolism in white adipocytes promotes inflammation. *Nat Metab* 4 (2022) 190-202
- [75] Birdsall RE, Kellett J, Yu YQ, Chen W. Application of mobile phase additives to reduce metal-ion mediated adsorption of non-phosphorylated peptides in RPLC/MS-based assays. *J Chromatogr B Analyt Technol Biomed Life Sci* 1126-1127 (2019) 121773
- [76] Schneider S, Planitz P. Determination of low-metal release from the Agilent 1260 Infinity Bio-inert Quaternary LC system using ICP-MS. in, Agilent Technologies Technical Overview, Santa Clara, CA, (2017) 5991-8314EN
- [77] Arnold PK, Finley LWS. Regulation and function of the mammalian tricarboxylic acid cycle. *J Biol Chem* 299 (2023) 102838
- [78] Wong TL, Che N, Ma S. Reprogramming of central carbon metabolism in cancer stem cells. *Biochim Biophys Acta Mol Basis Dis* 1863 (2017) 1728-1738
- [79] Martinez-Reyes I, Chandel NS. Mitochondrial TCA cycle metabolites control physiology and disease. *Nat Commun* 11 (2020) 102
- [80] Siegel D, Permentier H, Reijngoud DJ, Bischoff R. Chemical and technical challenges in the analysis of central carbon metabolites by liquid-

- chromatography mass spectrometry. *J Chromatogr B Analyt Technol Biomed Life Sci* 966 (2014) 21-33
- [81] Klein S, Heinzle E. Isotope labeling experiments in metabolomics and fluxomics. *Wiley Interdiscip Rev Syst Biol Med* 4 (2012) 261-272
- [82] Kruger NJ, Masakapalli SK, Ratcliffe RG. Strategies for investigating the plant metabolic network with steady-state metabolic flux analysis: lessons from an Arabidopsis cell culture and other systems. *J Exp Bot* 63 (2012) 2309-2323
- [83] Kao CC, Hsu JW, Bandi V, Hanania NA, Kheradmand F, Jahoor F. Resting energy expenditure and protein turnover are increased in patients with severe chronic obstructive pulmonary disease. *Metabolism* 60 (2011) 1449-1455
- [84] Azizi G, Khannazer N, Mirshafiey A. The Potential Role of Chemokines in Alzheimer's Disease Pathogenesis. *Am J Alzheimers Dis Other Demen* 29 (2014) 415-425
- [85] Ott BR, Jones RN, Daiello LA, De La Monte SM, Stopa EG, Johanson CE, Denby C, Grammas P. Blood-Cerebrospinal Fluid Barrier Gradients in Mild Cognitive Impairment and Alzheimer's Disease: Relationship to Inflammatory Cytokines and Chemokines. *Front Aging Neurosci* 10 (2018) 245
- [86] Russell DG, Huang L, Vanderven BC. Immunometabolism at the interface between macrophages and pathogens. *Nat Rev Immunol* 19 (2019) 291-304
- [87] Wolfe H, Mela V, Minogue AM, Miller AM, Mcguigan C, Williams L, Lohan D, Lawlor BA, Lynch MA. Monocytes exposed to plasma from patients with Alzheimer's disease undergo metabolic reprogramming. *Neurosci Res* 148 (2019) 54-60
- [88] Palmer CS, Cherry CL, Sada-Ovalle I, Singh A, Crowe SM. Glucose Metabolism in T Cells and Monocytes: New Perspectives in HIV Pathogenesis. *EBioMedicine* 6 (2016) 31-41
- [89] Torretta S, Scagliola A, Ricci L, Mainini F, Di Marco S, Cuccovillo I, Kajaste-Rudnitski A, Sumpton D, Ryan KM, Cardaci S. D-mannose suppresses macrophage IL-1beta production. *Nat Commun* 11 (2020) 6343
- [90] Cheng SC, Quintin J, Cramer RA, Shepardson KM, Saeed S, Kumar V, Giamarellos-Bourboulis EJ, Martens JH, Rao NA, Aghajani-refah A, Manjeri GR, Li Y, Ifrim DC, Arts RJ, Van Der Veer BM, Deen PM, Logie C, O'Neill LA, Willems P, Van De Veerdonk FL, Van Der Meer JW, Ng A,

- Joosten LA, Wijmenga C, Stunnenberg HG, Xavier RJ, Netea MG. mTOR- and HIF-1 α -mediated aerobic glycolysis as metabolic basis for trained immunity. *Science* 345 (2014) 1250684
- [91] Prinz M, Priller J. Microglia and brain macrophages in the molecular age: from origin to neuropsychiatric disease. *Nat Rev Neurosci* 15 (2014) 300-312
- [92] Mikita J, Dubourdieu-Cassagno N, Deloire MS, Vekris A, Biran M, Raffard G, Brochet B, Canron MH, Franconi JM, Boiziau C, Petry KG. Altered M1/M2 activation patterns of monocytes in severe relapsing experimental rat model of multiple sclerosis. Amelioration of clinical status by M2 activated monocyte administration. *Mult Scler* 17 (2011) 2-15
- [93] Prinz M, Jung S, Priller J. Microglia Biology: One Century of Evolving Concepts. *Cell* 179 (2019) 292-311
- [94] Graeber MB. Neuroinflammation: no rose by any other name. *Brain Pathol* 24 (2014) 620-622
- [95] Woodburn SC, Bollinger JL, Wohleb ES. The semantics of microglia activation: neuroinflammation, homeostasis, and stress. *J Neuroinflammation* 18 (2021) 258
- [96] Zrzavy T, Hametner S, Wimmer I, Butovsky O, Weiner HL, Lassmann H. Loss of 'homeostatic' microglia and patterns of their activation in active multiple sclerosis. *Brain* 140 (2017) 1900-1913
- [97] Patel HC, Boutin H, Allan SM. Interleukin-1 in the brain: mechanisms of action in acute neurodegeneration. *Ann N Y Acad Sci* 992 (2003) 39-47
- [98] Griffin WS, Stanley LC, Ling C, White L, Macleod V, Perrot LJ, White CL, 3rd, Araoz C. Brain interleukin 1 and S-100 immunoreactivity are elevated in Down syndrome and Alzheimer disease. *Proc Natl Acad Sci U S A* 86 (1989) 7611-7615
- [99] Zhao M, Cribbs DH, Anderson AJ, Cummings BJ, Su JH, Wasserman AJ, Cotman CW. The induction of the TNF α death domain signaling pathway in Alzheimer's disease brain. *Neurochem Res* 28 (2003) 307-318
- [100] Kouwenhoven M, Teleshova N, Ozenci V, Press R, Link H. Monocytes in multiple sclerosis: phenotype and cytokine profile. *J Neuroimmunol* 112 (2001) 197-205
- [101] Diskin C, Palsson-Mcdermott EM. Metabolic Modulation in Macrophage Effector Function. *Front Immunol* 9 (2018) 270

- [102] Izquierdo E, Cuevas VD, Fernandez-Arroyo S, Riera-Borrull M, Orta-Zavalza E, Joven J, Rial E, Corbi AL, Escribese MM. Reshaping of Human Macrophage Polarization through Modulation of Glucose Catabolic Pathways. *J Immunol* 195 (2015) 2442-2451
- [103] Raulien N, Friedrich K, Strobel S, Rubner S, Baumann S, Von Bergen M, Korner A, Krueger M, Rossol M, Wagner U. Fatty Acid Oxidation Compensates for Lipopolysaccharide-Induced Warburg Effect in Glucose-Deprived Monocytes. *Front Immunol* 8 (2017) 609
- [104] Lee MKS, Al-Sharea A, Shihata WA, Bertuzzo Veiga C, Cooney OD, Fleetwood AJ, Flynn MC, Claeson E, Palmer CS, Lancaster GI, Henstridge DC, Hamilton JA, Murphy AJ. Glycolysis Is Required for LPS-Induced Activation and Adhesion of Human CD14(+)CD16(-) Monocytes. *Front Immunol* 10 (2019) 2054
- [105] Dominguez-Andres J, Arts RJW, Ter Horst R, Gresnigt MS, Smeekens SP, Ratter JM, Lachmandas E, Boutens L, Van De Veerdonk FL, Joosten LaB, Notebaart RA, Ardavin C, Netea MG. Rewiring monocyte glucose metabolism via C-type lectin signaling protects against disseminated candidiasis. *PLoS Pathog* 13 (2017) e1006632
- [106] Ren W, Xia Y, Chen S, Wu G, Bazer FW, Zhou B, Tan B, Zhu G, Deng J, Yin Y. Glutamine Metabolism in Macrophages: A Novel Target for Obesity/Type 2 Diabetes. *Adv Nutr* 10 (2019) 321-330
- [107] Spiljar M, Kuchroo VK. Metabolic regulation and function of T helper cells in neuroinflammation. *Semin Immunopathol* 44 (2022) 581-598
- [108] Stienstra R, Netea-Maier RT, Riksen NP, Joosten LaB, Netea MG. Specific and Complex Reprogramming of Cellular Metabolism in Myeloid Cells during Innate Immune Responses. *Cell Metab* 26 (2017) 142-156
- [109] Nishizawa T, Kanter JE, Kramer F, Barnhart S, Shen X, Vivekanandan-Giri A, Wall VZ, Kowitz J, Devaraj S, O'brien KD, Pennathur S, Tang J, Miyaoka RS, Raines EW, Bornfeldt KE. Testing the role of myeloid cell glucose flux in inflammation and atherosclerosis. *Cell Rep* 7 (2014) 356-365

9 List of Publications

9.1 Publications in scientific peer-reviewed journals

Giacomello G, Otto C, Priller J, Ruprecht K, Böttcher C, Parr MK. 1,2-¹³C₂-Glucose Tracing Approach to Assess Metabolic Alterations of Human Monocytes under Neuroinflammatory Conditions. *Current Issues in Molecular Biology* 45 (2023) 765-781.

<https://doi.org/10.3390/cimb45010051>

Fernández Zapata C, Giacomello G, Spruth EJ, Middeldorp J, Gallaccio G, Dehlinger A, Dames C, Leman JKH, van Dijk RE, Meisel A, Schlickeiser S, Kunkel D, Hol EM, Paul F, Parr MK, Priller J, Böttcher C. Differential compartmentalisation of myeloid cell phenotypes and responses towards the CNS in Alzheimer's disease. *Nature Communications* 13 (2022) 7210.

<https://doi.org/10.1038/s41467-022-34719-2>

Giacomello G, Böttcher C, Parr MK. Isotopic tracing of glucose metabolites in human monocytes to assess changes in inflammatory conditions. *STAR Protocols* 3 (2022) 101715.

<https://doi.org/10.1016/j.xpro.2022.101715>

Giacomello G, Scholten A, Parr MK. Current methods for stress marker detection in saliva. *Journal of Pharmaceutical and Biomedical Analysis* 191 (2020) 113604.

<https://doi.org/10.1016/j.jpba.2020.113604>

9.2 Oral presentations

Giacomello G, Böttcher C, Parr MK. Phenotypic alterations of glucose-metabolism in stimulated monocytes. *NeuroMac* School-Winter School 2022 (18 September 2022), Copenhagen, Denmark.

Giacomello G, Parr MK. Targeted metabolomics - an HPLC-MS/MS method for the analysis of small, polar compounds. COOPERA-Workshop: Cooperation in Education and Research for Analysis with Mass Spectrometry (6-7 December 2021), Berlin/Cairo online conference.

Giacomello G, Böttcher C, Parr MK. Metabolic flux analysis for pathway elucidation in neurodegenerative diseases. *NeuroMac* School-Winter School 2021 (2-3 December 2021), Berlin, Germany.

9.3 Poster presentations

Giacomello G, Böttcher C, Parr MK. Assessment of metabolic alterations by isotopic tracing. International Symposium on Brain Myeloid Cells (16-17 September 2022), Copenhagen, Denmark.

Giacomello G, Böttcher C, Parr MK. Development and validation of a method to trace ^{13}C through glucose metabolism. DPhg Berlin-Brandenburg 12th Scientific Symposium (8 July 2022), Berlin, Germany.

10 Independence Declaration

I hereby affirm that I have completed the presented cumulative dissertation independently and without unauthorised assistance. No aids other than those listed in the text were used in the writing of the dissertation.

A doctoral procedure has never been completed at any other university or applied to another department.

Ginevra Giacomello

11 Appendix

11.1 List of Figures

- Figure 1: Barrier between CSF and blood in the choroid plexus in healthy individuals (upper pane) and patients with AD or MScl (lower pane). In the case of diseased people, the tight junctions of the epithelium lose their integrity, allowing the passage of myeloid cells into the CSF [26-29] (figure created with BioRender.com). 4
- Figure 2: Major metabolic pathways of a cell. A: glycolysis; B: pentose phosphate pathway (PPP); C: glutamate/glutamine metabolism; D: tricarboxylic acid (TCA) cycle; E: lactate metabolism; F: serine/glycine metabolism (figure created with BioRender.com)..... 7
- Figure 3: Metabolism (glycolysis and pentose phosphate pathway (PPP)) of [1,2-¹³C₂]glucose. The isotopic distribution of labelled carbons makes it possible to distinguish between the formation pathways of fructose-6-phosphate (green squared frames) and lactate (orange squared frames). G6P: glucose-6-phosphate; F6P: fructose-6-phosphate; FBP: fructose-1,6-biphosphate; G3P: glyceraldehyde-3-phosphate; DHAP: dihydroxyacetone phosphate; LAC: lactate; 6PGL: glucono-1,5-lactone-6-phosphate; 6PG: gluconate-6-phosphate; Ru5P: ribulose-5-phosphate; R5P: ribose-5-phosphate; X5P: xylulose-5-phosphate; S7P: sedoheptulose-7-phosphate; E4P: erythrose-4-phosphate (figure created with BioRender.com). 10
- Figure 4: Chromatographic peaks of ribose-5-phosphate (R5P). A: chromatogram of R5B with no additives in the mobile phases. The peak is broad due to the coordinating interactions of the phosphate group of the analyte with the metallic parts of the instrumentation (iron cations). B: chromatogram of R5B with medronic acid as additive in both the mobile phases (method detailed in Manuscript I). The peak shape is optimised, allowing the identification and quantification of the analyte. Column: Agilent InfinityLab Poroshell 120 HILIC-Z, 2.1 x 100 mm, 2.7 µm; extracted ion chromatograms in negative mode (EIC-) of ribose-5-phosphate ([M-H]⁻ m/z 229.0). 15

11.2 List of Tables

Table 1: Metabolites (displayed as unlabelled form) of the major metabolic pathways targeted in this study (structures created with ChemDraw Professional 15.1)	12
---	----